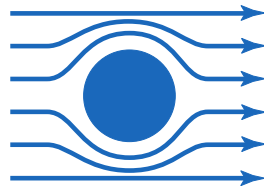




Technische  
Universität  
München



Walther-Meißner  
Institut



Bayrische  
Akademie  
der Wissenschaften

---

# Superconducting Microwave Resonator Designs for Electron Spin Resonance Applications

---

Master's thesis  
Petio Natzkin

Supervisor: Priv.-Doz. Dr. Hans-Gregor Huebl

Garching – December 4, 2017



# Contents

<b>1</b>	<b>Introduction</b>	<b>1</b>
<b>2</b>	<b>Theory</b>	<b>5</b>
2.1	Microwave Resonators . . . . .	5
2.1.1	Equation of motion . . . . .	5
2.1.2	Steady-state solution . . . . .	7
2.1.3	Excitation Dynamics . . . . .	8
2.1.4	Frequency Domain . . . . .	14
2.1.5	Integrated Resonator Field . . . . .	16
2.1.6	Asymmetric Lineshape . . . . .	18
2.2	Phosphorus doped Silicon . . . . .	20
<b>3</b>	<b>Methods</b>	<b>23</b>
3.1	Fabrication of Niobium Resonators with Aluminum-coating . . . . .	23
3.2	Sample Preparation . . . . .	24
3.3	Measurement Setups . . . . .	25
3.3.1	Continuous Wave Setup . . . . .	25
3.3.2	Time Domain Setup . . . . .	26
3.4	Heterodyne Signal Detection . . . . .	28
<b>4</b>	<b>Resonator Designs and Pre-characterization</b>	<b>31</b>
4.1	Lumped Element Resonators . . . . .	32
4.1.1	Capacitively Shunted Meander Resonator . . . . .	32
4.1.2	Meander Resonator . . . . .	36
4.1.3	Spiral Resonator . . . . .	38
4.1.4	Coupling to Transmission Line . . . . .	39
4.1.5	Dynamic Magnetic Field . . . . .	42
4.2	Continuous Wave Pre-characterization . . . . .	47
4.2.1	Resonance Transmission Fit . . . . .	47
4.2.2	Sample Pre-characterization . . . . .	49
4.2.3	Temperature . . . . .	53
4.2.4	Static Magnetic Field . . . . .	57
4.2.5	Microwave Power . . . . .	58

---

4.3	Time Domain Pre-characterization . . . . .	60
4.3.1	Time Domain Transmission Measurements . . . . .	60
4.3.2	Steady-state Transmission . . . . .	62
4.3.3	Resonator Dynamics . . . . .	63
4.4	Summary . . . . .	65
<b>5</b>	<b>Continuous Wave Electron Spin Resonance</b>	<b>67</b>
5.1	Collective Coupling of a Spin Ensemble to a Lumped Element Resonator . . . . .	67
5.1.1	Field Calibration . . . . .	67
5.1.2	Spectroscopic Characterization . . . . .	68
5.1.3	Characterization of the Spin Ensemble . . . . .	71
5.1.4	Modeling of the Filling Factor . . . . .	74
5.2	Power Dependence of $g_{\text{eff}}$ . . . . .	75
5.3	Temperature Dependence of $g_{\text{eff}}$ . . . . .	77
5.4	Summary . . . . .	79
<b>6</b>	<b>Pulsed Electron Spin Resonance</b>	<b>81</b>
6.1	Multiple Pulse Calibration . . . . .	81
6.1.1	Hahn Echo Pulse Sequence . . . . .	82
6.1.2	Pulse Length Calibration . . . . .	83
6.2	Pulsed ESR Experiments . . . . .	85
6.2.1	Hahn Echo Spectroscopy . . . . .	85
6.2.2	Echo-detected Frequency Sweep . . . . .	88
6.2.3	Echo-detected Field Sweep . . . . .	89
6.2.4	Inversion Recovery . . . . .	90
6.2.5	Driven Rabi Oscillations . . . . .	92
6.3	Summary . . . . .	93
<b>7</b>	<b>Summary &amp; Outlook</b>	<b>95</b>
<b>A</b>	<b>Appendix</b>	<b>99</b>
A.1	Power Dependence of the Dynamic Resonator Field . . . . .	99
A.2	Estimation of Microstrip Inductance and Capacitance . . . . .	100
A.3	Finite Element Method Simulations with CST Microwave Studios . . . . .	100
A.4	Kinetic Inductance . . . . .	101
A.4.1	Kinetic Inductance for Inhomogeneous Current Density . . . . .	101
A.4.2	Influence on Resonance Frequency . . . . .	103

# Chapter 1

## Introduction

Since the discovery of the first electron spin resonance spectrum by Evgenii K. Zavoisky in the middle of the past century [1,2], electron paramagnetic resonance has evolved to a versatile spectroscopy technique. It is advanced by an ever-growing research community covering a multitude of research areas and application fields, ranging from material science, molecular biology, chemistry, pharmacy and food industry to the field of quantum information processing. For instance, *in vivo* ESR imaging is used in radiological cancer therapy and for examining mechanisms related to oxidative diseases [3,4]. Also, studying the structure and properties of spin-labelled proteins and other complex molecules down to the nanoscale was enabled by ESR spectroscopy [5,6]. Already since the early phase, this technique was widely applied to investigate paramagnetic impurities and defects in semiconductors [7–13].

To this day, ESR spectroscopy has a limited sensitivity of  $\approx 10^{10}$  spins detectable within a single measurement at room temperature using inductive detection [14]. A major improvement was achieved with the development of Electrically Detected Magnetic Resonance (EDMR), which is based on the spin-dependent conductivity in semiconductors [15,16] and allows for an enhanced sensitivity down to the single spin level at low temperatures [17–19]. Single spin sensitivity has also been reported for Optically Detected Magnetic Resonance (ODMR) [20,21], which can be applied in the presence of suitable optical transitions. However, these indirect measurement techniques are not quantitative with respect to the determination of the spin density and additionally, they are restricted to a limited set of materials and substances.

The sensitivity of inductively-detected ESR experiments can be improved by performing the measurements at kelvin or millikelvin temperatures, utilizing the increased polarization of paramagnetic spin ensembles and the suppression of thermal noise [22]. Furthermore, low temperatures allow the usage of superconducting microwave resonators, which imply low losses and high quality factors [23]. Generally, the concept of planar microresonators enables smaller sample volumes and higher filling factors, compared to conventional three-dimensional cavities [24–26].

Recently, major achievements in sensitivity have been reported for spin systems weakly coupled to superconducting microwave resonators, by using squeezed microwaves [22] and amplification with supplemented noise at the quantum limit as well as optimized resonator structures [27,28]. Moreover, strong coupling between a spin ensemble and a microwave resonator has been demonstrated for numerous spin ensembles [26,29–32]. In the strong coupling regime, the collective

coupling rate of paramagnetic spins to the superconducting resonator exceeds both components' individual loss rates, enabling a coherent exchange of information between the resonator and the spin system at high fidelity [33]. Furthermore, it is possible to store multiple coherent microwave states within one spin system [34, 35]. Finally, the coherence times of such systems are shown to exceed seconds [36]. Taken together, solid-state based paramagnetic spin systems are promising candidates for future quantum memory applications in the large framework of cavity quantum electrodynamics [29, 33, 37–39].

The geometric design of a superconducting resonator is of key importance for ESR experiments [23, 27], as it particularly defines the dynamic excitation field, which mediates the coupling to the spin system. Additionally, different ESR experiments impose different requirements on the resonator. For instance strong coupling is more easily achieved with narrow linewidth resonators, while pulsed ESR measurements are more conveniently performed with broadband resonators.

The goal of this thesis is to study the influence of the geometric design of superconducting lumped element microwave resonators on the performance in various ESR applications. To this end, we develop and study three different resonator geometries, including the novel design approach of a spiral resonator, which enables an improved homogeneity of the excitation magnetic field increasing the sensitivity in pulsed ESR experiments. Furthermore, the spiral resonator vastly outperforms the other designs in specific ESR experiments, for instance, when conducting measurements at elevated temperatures or aiming for a maximal coupling between spin ensemble and resonator under realistic sample mounting conditions. Moreover, we tailor the resonator properties using Finite Element Method (FEM) simulations and compare them to characterization measurements. Finally, we demonstrate the qualification of all three resonator designs for continuous wave and pulsed ESR experiments using phosphorus doped silicon as a benchmark system. The properties of this spin ensemble are characterized with various standard ESR experiments.

We present a quantum mechanical framework for describing the coupled system of microwave resonator and transmission line in Chapter 2. In particular, we discuss the steady-state and dynamic excitation of resonators, which is useful for understanding the results of continuous wave and pulsed ESR experiments, respectively.

In Chapter 3, we describe the microfabrication process used for producing superconducting Lumped Element Resonators (LER) composed of aluminum-coated niobium. Additionally, we explain the measurement technique of the frequency and the time domain setup.

Chapter 4 is divided into three parts. First, we present different concepts of LERs including an approach towards improved homogeneity of the magnetic excitation field. Using FEM simulations, we investigate the tunability of resonator parameters, particularly focusing on the resonance frequency and the external coupling strength. Additionally, the simulations give insight into the three-dimensional distribution of the dynamic magnetic field, which is one key parameter of microwave resonators for ESR applications. In Section 4.2, we employ continuous wave measurements to pre-characterize a chip hosting 14 LERs of three different designs with and without a mounted sample. Furthermore, we investigate the influence of temperature, magnetic field and incident microwave power on the resonator parameters, identifying operational limits of the res-

onators for ESR applications and comparing the performance of resonator designs against each other. Section 4.3 presents time-resolved transmission measurements of microwave resonators after applying an excitation pulses. We compare experimental results with theoretical expectations based on the framework introduced in Section 2.1.

In Chapter 5, we analyze the spectrum of phosphorus doped silicon using continuous wave ESR measurements at liquid helium temperatures. We extract the collective coupling rate of the spin ensemble coupled to a LER and compare the result with expectations from theory. Furthermore, we investigate and model the saturation of the spin system for moderate and high microwave powers, which is a consequence of high relaxation times. Additionally, we study the temperature dependence of the collective coupling strength and the saturation behaviour.

We present pulsed ESR measurement in Chapter 6, starting with a discussion of the optimal pulse length in a Hahn echo experiment, aiming for maximization of the echo signal. Next, we present various pulsed ESR experiments, allowing to determine the relaxation times and loss rate of the spin system. Additionally, we consider the performance of lumped element resonators in driven Rabi oscillations.

The thesis is concluded with a summary and outlook in Chapter 7.



# Chapter 2

## Theory

We discuss the theory of microwave resonators in Section 2.1 and consider the spectroscopic features of phosphorus doped silicon in Section 2.2.

### 2.1 Microwave Resonators

In this section we study the fundamentals and characteristics of a microwave resonator. Based on a quantum mechanical description and input-output theory, we present a framework for describing the excitation of resonators coupled to a microwave transmission line, resulting in the equation of motion for the coupled system. We solve this equation for the steady-state (Section 2.1.2) and the dynamic case (Section 2.1.3), and examine the influence of intrinsic resonator parameters on the latter. Furthermore, we consider the interplay of time domain and frequency domain microwave pulse shapes, regarding pulsed excitations of resonators (Sections 2.1.4 and 2.1.5). In Section 2.1.6, we discuss asymmetric lineshapes and their modeling.

#### 2.1.1 Equation of motion

Based on a quantum mechanical description of the microwave fields including input-output theory [40], we consider the system of a resonator coupled to a microwave transmission line. In the classical picture, the microwave electric ( $E_1$ ) and magnetic field ( $B_1$ ) is a physical quantity and therefore real valued. However, it is useful to express for instance the dynamic magnetic field as  $B_1 = \tilde{B}_1 + \tilde{B}_1^*$ , where  $\tilde{B}_1$  is complex. In the quantum mechanical framework, the equivalent of  $\tilde{B}_1$  is, apart from prefactors, given by the annihilation operator  $a_r$ , which is related to the microwave field via  $B_1 \propto (a_r + a_r^\dagger)$  [41]. The operator  $a_r$  is the quantum mechanical system operator of the microwave resonator and represents the microwave field in the resonator.

For an absorption type resonator, schematically illustrated in Figure 2.1, the interplay between a vector valued microwave drive field  $\mathbf{b}_{\text{in}}$  and the vector valued system operator  $\mathbf{a}$  is described via the linear Heisenberg equation of motion [40, 42]

$$\dot{\mathbf{a}}(t) = A\mathbf{a}(t) - \kappa\mathbf{a}(t) + \sqrt{\kappa_{\text{ext}}} \mathbf{b}_{\text{in}}(t), \quad (2.1)$$

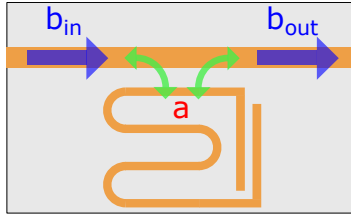


**Figure 2.1:** Schematic of absorption resonator coupled to transmission line with illustrations of microwave input and output signals (blue arrows) and excitation transfer paths between resonator and transmission line (green arrows).

with

$$A = \begin{pmatrix} -i\omega_r & 0 \\ 0 & i\omega_r \end{pmatrix}, \quad \mathbf{a}(t) = \begin{pmatrix} a_r(t) \\ a_r^\dagger(t) \end{pmatrix}, \quad \mathbf{b}_{\text{in}}(t) = \begin{pmatrix} b_{\text{in}}(t) \\ b_{\text{in}}^\dagger(t) \end{pmatrix}. \quad (2.2)$$

This gives two separate equations for  $a_r(t)$  and  $a_r^\dagger(t)$ , which however represent equivalent descriptions of the system. We decide to continue with the equation of motion for the creation operator  $a_r^\dagger$ , as this equation is associated with a counterclockwise ( $e^{i\omega t}$ ) rotation of operators in the complex plane, which is the mathematical rotation direction and will prove suitable for describing the measurement results. Henceforth, the creation operator is denoted as  $a$  and referred to as the resonator field. Its equation of motion reads

$$\dot{a}(t) = i\omega_r a(t) - \kappa a(t) + \sqrt{\kappa_{\text{ext}}} b_{\text{in}}(t). \quad (2.3)$$

The last term represents the drive of the resonator via an external microwave field  $b_{\text{in}}(t)$ . The term  $-\kappa a(t) = -(\kappa_{\text{ext}} + \kappa_{\text{int}})a(t)$  corresponds to losses of resonator photons coupling into the transmission line ( $\kappa_{\text{ext}}$ ) and internal losses ( $\kappa_{\text{int}}$ ). The half-widths  $\kappa$ ,  $\kappa_{\text{ext}}$  and  $\kappa_{\text{int}}$  have angular frequency units and are linked to the Q-factors via

$$Q = \frac{\omega_r}{2\kappa}, \quad Q_{\text{ext}} = \frac{\omega_r}{2\kappa_{\text{ext}}}, \quad Q_{\text{int}} = \frac{\omega_r}{2\kappa_{\text{int}}}, \quad (2.4)$$

and therefore

$$\frac{1}{Q} = \frac{1}{Q_{\text{ext}}} + \frac{1}{Q_{\text{int}}}. \quad (2.5)$$

Eq. (2.3) takes into account that photons transferred from transmission line to resonator and vice versa are free to propagate along the signal line in two directions, which reduces the effective rate of external coupling to the input field  $b_{\text{in}}$ :

$$\kappa_{\text{ext,eff}} = \frac{\kappa_{\text{ext}}}{2}. \quad (2.6)$$

Finally, the output field of an absorption resonator is given by [42]

$$b_{\text{out}}(t) = b_{\text{in}}(t) - \sqrt{\kappa_{\text{ext}}} a(t). \quad (2.7)$$

This relation, combined with the equation of motion, enables the calculation of steady-state transmission for continuous wave drives and dynamic transmission for arbitrary input fields  $b_{\text{in}}(t)$ .

### 2.1.2 Steady-state solution

We consider a continuous drive tone with frequency  $\omega/2\pi$  expressed by  $b_{\text{in}}(t) = \tilde{b}_{\text{in}} e^{i\omega t}$ ,  $\tilde{b}_{\text{in}} \in \mathbb{R}$ , and make the ansatz  $a(t) = \tilde{a} e^{i\omega t}$ ,  $\tilde{a} \in \mathbb{C}$ , for the resulting resonator field. Substitution into the equation of motion (Eq. (2.3)) yields

$$\dot{a} = \dot{\tilde{a}} e^{i\omega t} + (i\omega_r - \kappa) \tilde{a} e^{i\omega t} = (i\omega_r - \kappa) \tilde{a} e^{i\omega t} + \sqrt{\kappa_{\text{ext}}} \tilde{b}_{\text{in}} e^{i\omega t} \quad (2.8)$$

and therefore

$$\dot{\tilde{a}} = -(i\Delta + \kappa) \tilde{a} + \sqrt{\kappa_{\text{ext}}} \tilde{b}_{\text{in}}, \quad (2.9)$$

where  $\Delta = \omega - \omega_r$  denotes the detuning from the resonance frequency. Further, we focus on the steady-state case, where the resonator loss rates ( $\kappa_{\text{ext}}$  and  $\kappa_{\text{int}}$ ) are in equilibrium with the rate of photons coupling from the transmission line into the resonator, which means  $\dot{\tilde{a}} = 0$ . Now, solving Eq. (2.9) for  $\tilde{a}$  gives the steady-state result

$$\tilde{a} = \frac{\sqrt{\kappa_{\text{ext}}}}{\kappa + i\Delta} \tilde{b}_{\text{in}}. \quad (2.10)$$

We find that  $\tilde{a}$  is real-valued only at zero detuning  $\Delta = 0$ . Hence, there is a phase shift  $\varphi_a(\omega)$  between the resonator and input field for  $\Delta \neq 0$ :

$$\varphi_a(\omega) := \arctan\left(\frac{\text{Im}(\tilde{a}(\omega))}{\text{Re}(\tilde{a}(\omega))}\right) \stackrel{\text{(eq. 2.10)}}{=} -\arctan\left(\frac{\Delta}{\kappa}\right). \quad (2.11)$$

Next, we establish a link to the transmission parameter  $S_{21} := b_{\text{out}}(\omega)/b_{\text{in}}(\omega)$ , which, in contrast to the resonator field  $a$ , is directly measurable. Using equations 2.7 and 2.10 we find

$$S_{21}(\omega) = \frac{b_{\text{out}}(\omega)}{b_{\text{in}}(\omega)} = \frac{b_{\text{in}}(\omega) - \sqrt{\kappa_{\text{ext}}} a(\omega)}{b_{\text{in}}(\omega)} = 1 - \frac{\sqrt{\kappa_{\text{ext}}} \tilde{a}(\omega)}{\tilde{b}_{\text{in}}(\omega)} = 1 - \frac{\kappa_{\text{ext}}}{\kappa + i\Delta}. \quad (2.12)$$

In analogy to  $\varphi_a$ , we define the phase shift between output and input field via

$$\varphi_t(\omega) := \arctan\left(\frac{\text{Im}(S_{21}(\omega))}{\text{Re}(S_{21}(\omega))}\right). \quad (2.13)$$

The phase shift  $\varphi_t$  originates from interference between the drive tone  $b_{\text{in}}$  and the resonator field  $a$  coupling back into the transmission line.

Figure 2.2(a) shows the power transmission  $|S_{21}|^2$  and the squared resonator field magnitude  $|a|^2$  as a function of the detuning  $\Delta$  for an absorption resonator coupled to a transmission line. We exemplarily consider an overcoupled resonator with coupling coefficient  $\eta_c = 0.9$ , where

$$\eta_c := \frac{\kappa_{\text{ext}}}{\kappa}. \quad (2.14)$$

At zero detuning, the transmission is minimal whereas the resonator field magnitude is maximal. The phase relations of  $S_{21}$  and  $a$  with respect to the microwave drive are depicted in Figure 2.2(b). At  $\Delta = 0$ , we observe perfect destructive interference between resonator photons coupling back

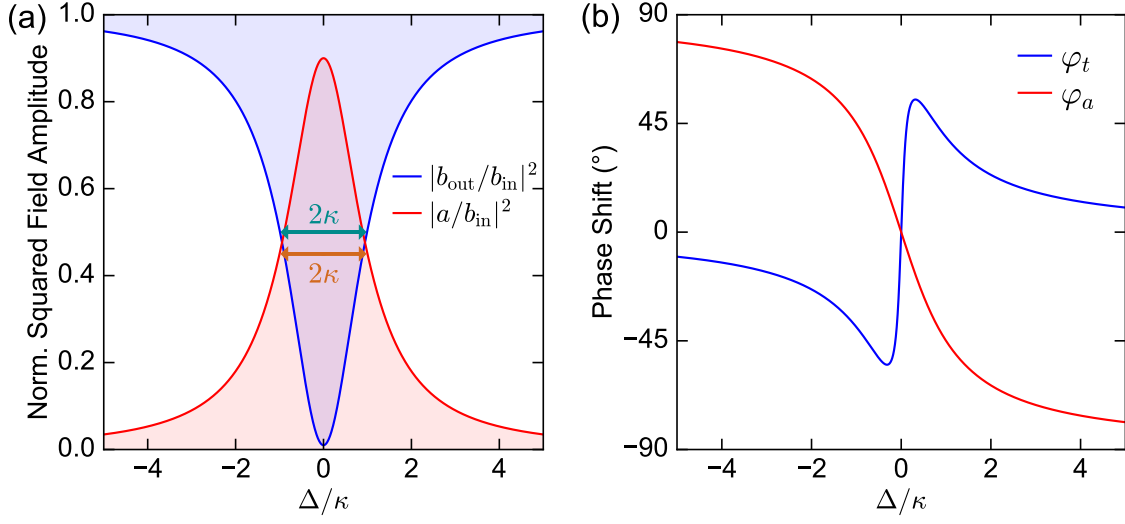


**Figure 2.2:** Calculated steady-state excitation of overcoupled absorption resonator with  $\eta_c = 0.9$ . **(a)** Power transmission  $|S_{21}|^2$  and normalized squared resonator field  $|a/b_{\text{in}}|^2$  as a function of detuning  $\Delta$ . **(b)** Phase shift of resonator field  $a$  and output field  $b_{\text{out}}$  with respect to input field  $b_{\text{in}}$  as a function of detuning  $\Delta$ .

into the transmission line and the input field  $b_{\text{in}}$ . The phase shift  $\varphi_t$  exhibits maximal deviation from zero close to  $\Delta = 0$ . The phase shift  $\varphi_a(\Delta)$  approaches the value  $90^\circ$  ( $-90^\circ$ ) for drive frequencies  $\omega/2\pi$  well-below (well-above) the resonance frequency  $\omega_r/2\pi$ . This behaviour is expected for a driven LC-circuit inductively coupled to a driving force.

In this section, we consider the relevant quantities, particularly the input field  $b_{\text{in}}$  as a dimensionless quantity for simplicity. However, in principle, it can be linked to the microwave power  $P_{\text{MW}}$  via

$$|b_{\text{in}}|^2 = \frac{P_{\text{MW}}}{\hbar\omega}, \quad (2.15)$$

as  $b_{\text{in}}$  is identified as the rate of photons propagating through the microwave transmission line. This yields in combination with Eq. (2.10) for the steady-state number of photons  $n$  in the resonator [43]

$$n = |a|^2 = \frac{\kappa_{\text{ext}}}{\kappa^2 + \Delta^2} |b_{\text{in}}|^2 = \frac{P_{\text{MW}}}{\hbar\omega} \frac{\kappa_{\text{ext}}}{\kappa^2 + \Delta^2}. \quad (2.16)$$

### 2.1.3 Excitation Dynamics

While continuous wave experiments yield information about the steady-state microwave transmission  $S_{21}$ , solving the equation of motion gives access to the resonator field  $a$ . The latter is proportional to the dynamic magnetic field  $B_1$  generated inside the resonator's mode volume, which in turn is the key parameter for ESR applications.

### 2.1.3.1 Resonator ring up and ring down

In this subsection, we focus on the excitation and relaxation dynamics of a microwave resonator by considering the rising and falling edge of a rectangular input microwave pulse, respectively. This is of interest, as the magnitude of the resonator field transient  $|a(t)|$  is proportional to the dynamic magnetic field magnitude  $B_1$  during an excitation pulse sequence in pulsed ESR experiments.

In General, we can calculate the resonator dynamics for an arbitrary input field  $b_{\text{in}}(t)$  by numerically solving the equation of motion (Eq. (2.3)) for  $b_{\text{in}}(t)$  with the boundary condition  $a(0) = 0$ . This was performed for a rectangular excitation pulse and zero detuning from the eigenfrequency ( $\Delta = 0$ ), resulting in the ring up and ring down behaviour illustrated in Figure 2.3. At the beginning of the rectangular pulse, we observe a ring up of the resonator field governed by  $|a| \propto (1 - e^{-\kappa t})$  with a characteristic time constant [44]

$$\tau_r = \frac{1}{\kappa}, \quad (2.17)$$

which is related to the quality factor of the system.

The output field magnitude  $|b_{\text{out}}|$  exhibits a behaviour opposite to  $a$  with an initial maximum at the very beginning of the excitation pulse followed by a decline towards steady state. This transient is also characterized by  $\tau_r$ . The contrary trend of  $b_{\text{out}}$  and  $a$  is attributed to destructive interference between the two contributions to  $b_{\text{out}}$  (described by Eq. (2.7)), which is the part of the input field  $b_{\text{in}}$  transmitted through the signal line and the resonator field coupling back into the signal line.

After the end of the excitation pulse, the input field vanishes ( $b_{\text{in}} = 0$ ) and the output field is sustained via the relaxing resonator field  $a$ , where part of the photons couple back into the transmission line contributing to  $b_{\text{out}}$ . This explains the similar trends of  $a$  and  $b_{\text{out}}$  after the end of

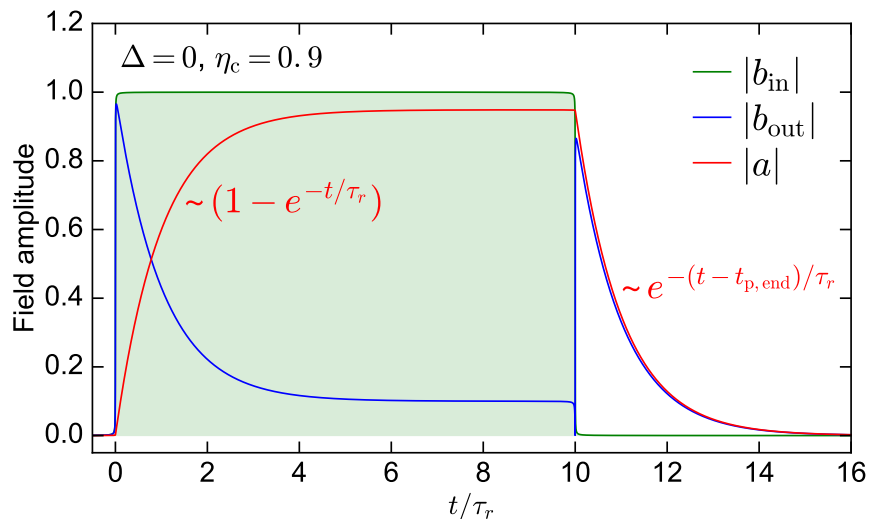


**Figure 2.3:** Simulated ring up and ring down of an overcoupled resonator ( $\eta_c = 0.9$ ) at zero detuning  $\Delta = 0$  as response to a rectangular excitation pulse from  $t = 0$  to  $t = t_{\text{p},\text{end}} = 10 \tau_r$ . The time axis is normalized to  $\tau_r$  (cf. Eq. (2.17)).

the rectangular pulse, shown in Figure 2.3. The exponential relaxation process of the resonator field is again governed by  $\tau_r$ .

We take a closer look at the phase relation of the output field defined via

$$\varphi_{\text{out}} := \arctan\left(\frac{\text{Im}(\tilde{b}_{\text{out}})}{\text{Re}(\tilde{b}_{\text{out}})}\right), \quad (2.18)$$

with  $b_{\text{out}}(t) = \tilde{b}_{\text{out}} e^{i\omega t}$ , and illustrated in Figure 2.4. We observe a sudden  $180^\circ$  phase shift in the output field phase relation  $\varphi_{\text{out}}$  at the end of the rectangular pulse: The input and output fields are in phase during the pulse ( $|b_{\text{in}}| = 1$ ) whereas, during the resonator ring down ( $|b_{\text{in}}| = 0$ ),  $b_{\text{out}}(t)$  is out of phase to  $a(t)$  (cf. Eq. (2.7)) and consequently out of phase to the input field.

Finally, we consider  $6\tau_r$  as a practical rule of thumb for the duration of transition to steady state. After this time, the deviation from steady state is less than 0.25 %.

### 2.1.3.2 Variation of Resonator Parameters

Next, we discuss the influence of linewidth  $\kappa$ , coupling coefficient  $\eta_c$  and detuning  $\Delta$  on the resonator dynamics, illustrated in Figure 2.5. For pulsed ESR, these design parameters are of key importance as they will decide upon the excitation bandwidth of the spin system as well as the readout contrast of the signals from the spin ensembles. In the following, we comment on the variation of each parameter.

The steady-state resonator field magnitude  $|a|$  increases with the coupling rate  $\kappa_{\text{ext}}$  between signal line and the resonator, which is explained by Eq. (2.10) for  $\Delta = 0$

$$|a| = \sqrt{\frac{\eta_c}{\kappa}} |b_{\text{in}}|. \quad (2.19)$$

However, the characteristic ring up and ring down time  $\tau_r$  is independent of  $\eta_c$ .

Considering a larger resonator linewidth  $\kappa$  for fixed  $\eta_c$ , we observe a steeper ring up and ring down, hence a decreased  $\tau_r$  (red curve), which is consistent with Eq. (2.17). Further, the steady-state transmission is decreased as well, which is again due to Eq. (2.19).

Finally, the resonator field transient for finite detuning  $\Delta > 0$  (green curve) also exhibits a decreased steady-state transmission accompanied by a ringing behaviour with a characteristic frequency given by  $\Delta$  and a decay of its envelope given by  $\tau_r$ . This is further investigated in the following subsections.

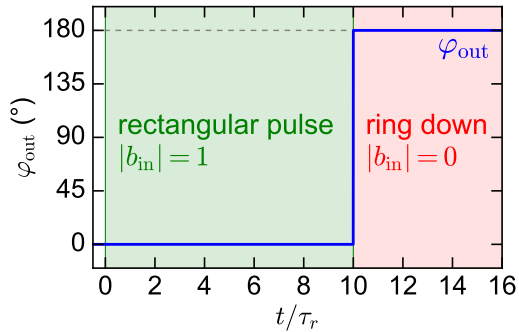
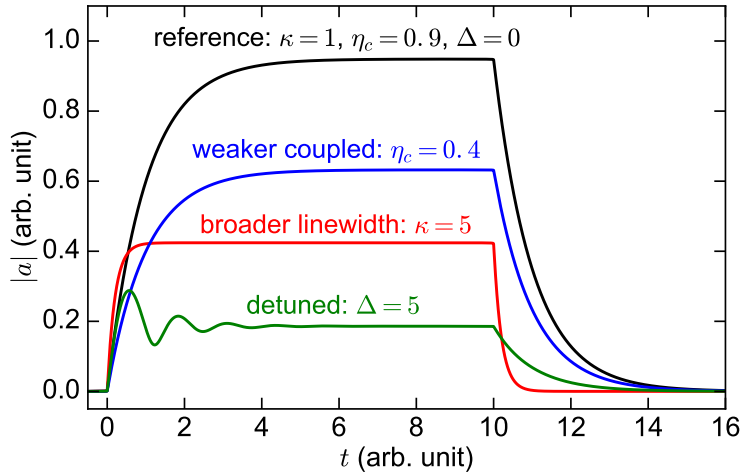


Figure 2.4: Phase relation  $\varphi_{\text{out}}$  of the output field  $b_{\text{out}}$  shown in Figure 2.3.



**Figure 2.5:** Unitless simulation of resonator field magnitude  $|a|$  as a function of time for different resonator parameter variations. The variation base is a reference resonator with  $\kappa = 1$ ,  $\eta_c = 0.9$  and  $\Delta = 0$ . The input field  $|b_{\text{in}}|$  corresponds to a rectangular pulse from  $t = 0$  to  $t = 10$ .

### 2.1.3.3 Offresonant Ring down

We describe the offresonant ring down of a microwave resonator. Assuming a non-zero resonator field  $a(t_0) = a_0$  at frequency  $\omega/2\pi$  and zero drive  $b_{\text{in}} = 0$  at time  $t_0$ , we consider for convenience the equation of motion in the laboratory frame, which reads

$$\dot{a} = (i\omega_r - \kappa)a \iff \frac{d}{dt} \ln(a) = (i\omega_r - \kappa), \quad (2.20)$$

and find the solution

$$a(t) = a_0 e^{(i\omega_r - \kappa)(t-t_0)}. \quad (2.21)$$

Consequently we have shown, that resonator ring down occurs at resonance frequency  $\omega_r/2\pi$ , independently of the previous drive tone frequency  $\omega/2\pi$ . This effect is observed after the end of a pulsed excitation, where the time-resolved transmission essentially changes oscillation frequency from the pulsed excitation frequency  $\omega/2\pi$  to the resonance frequency of the resonator  $\omega_r$ .

### 2.1.3.4 Offresonant Ring up

The offresonant excitation of an absorption resonator exhibits a damped ringing in the resonator field magnitude  $|a|$  as illustrated in Figure 2.6. We find the oscillation frequency of the ringing  $\omega_{\text{ring}}/2\pi$  to coincide with the detuning  $\Delta$ :

$$\omega_{\text{ring}} = \Delta. \quad (2.22)$$

In the following, we provide a explanation for this behaviour. The rising edge of the input field has a finite linewidth in frequency domain, resulting in resonator excitation at resonance frequency  $\omega_r/2\pi$  in the beginning of the pulse ( $t = 0$ ) even for large detuning  $\Delta \gg \kappa$  (cf. Section 2.1.4). This effect in combination with the resonator excitation at drive tone frequency  $\omega/2\pi$  explains

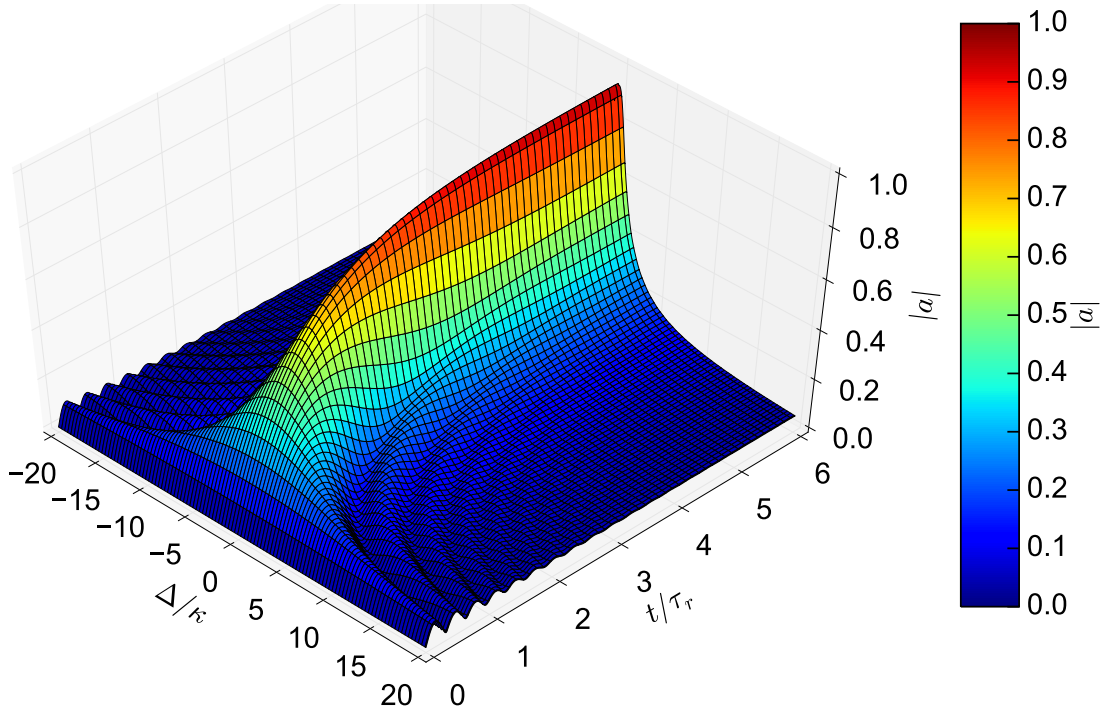


**Figure 2.6:** Simulated ring up of resonator field magnitude  $|a|$  as a function of time and detuning for an input field  $|b_{\text{in}}| = 0$  for  $t < 0$  and  $|b_{\text{in}}| = 1$  for  $t > 0$ . Values of  $|a|$  are visualized via color-code.

the ringing behaviour.

We develop a phenomenological ringing model for the dynamics of  $a(t)$ , in order to provide an understand of the dynamics, which is generally not given by numerical calculations. To this end, we assume instantaneous excitations  $a_{\text{res}}$  at  $\omega_r/2\pi$  and  $a_{\text{offres}}$  at  $\omega/2\pi$  via the rising edge of the input field ( $t = 0$ ). The resonator excitation at resonance frequency decays exponentially with increasing time while  $a_{\text{offres}}$  is continuously sustained by the microwave drive. Consequently, in this model, we express the resonator field transient by

$$a(t) = a_{\text{offres}} e^{i\omega t} + a_{\text{res}} e^{-\kappa t} e^{i(\omega-\Delta)t}. \quad (2.23)$$

We find for the field magnitude

$$|a(t)| = |a(t) e^{-i\omega t}| = \sqrt{a_{\text{offres}}^2 + a_{\text{res}}^2 e^{-2\kappa t} + 2 a_{\text{offres}} a_{\text{res}} e^{-\kappa t} \cos \Delta t}, \quad (2.24)$$

meaning that  $|a|^2$  performs a damped oscillation around a time-dependent offset, which converges to the steady-state value  $a_{\text{offres}}^2$  for large  $t$ .

As illustrated in Figure 2.7, the resonator field calculated with the ringing model is in perfect agreement with the simulation of  $|a|$  based on the equation of motion. Moreover, the best fit values for  $a_{\text{res}}$  and  $a_{\text{offres}}$  differ by less than 2 %. In the following, we discuss the ringing model (Eq. (2.24)).

According to Eq. (2.3), the excitation transfer from signal line to resonator is independent of the detuning  $\Delta$ . In addition, the steady-state resonator field magnitude is small for  $\Delta \gg \kappa$ . Hence, the resonator excitation reaches the steady-state level much faster than the characteristic time constant  $\tau_r$ , which justifies the assumption of instantaneous excitations in the ringing model. Due to the broad spectral density function of the input field (see 2.1.4), the resonator is excited in a wide frequency range at  $t = 0$ . However, this broad excitation starts to decay exponentially for  $t > 0$ , which occurs at resonance frequency as already shown by Eq. (2.21). Therefore, we have motivated the use of two distinct superposing frequencies for the resonator field in our ringing model (Eq. (2.23)).

### 2.1.3.5 Power Dependence

In this section, we discuss the power dependence of the resonator field magnitude  $|a|$ , assuming a microwave power below the critical power threshold of the resonator, at which non-linear excitation effects arise.

For the steady-state case, Eq. (2.10) shows that the resonator field magnitude  $|a|$  scales linearly with the magnitude of the input field  $|b_{\text{in}}|$ , which in turn is proportional to  $\sqrt{P_{\text{MW}}}$  (cf. Eq. (2.16)). A similar relation is derived for case of dynamic excitation in Appendix A.1.

There, we solve the equation of motion for an arbitrary pulse sequence at frequency  $\omega/2\pi$  and maximal microwave power  $P_{\text{MW}}$ , which implies for the input field

$$b_{\text{in}}(t, \omega, P_{\text{MW}}) = \sqrt{\frac{P_{\text{MW}}}{\hbar\omega}} \hat{b}_{\text{in}}(t), \quad t_0 < t < t_1 \quad (2.25)$$

with the fixed and normalized pulse sequence  $0 < \hat{b}_{\text{in}}(t) < 1$ . For convenience, the relevant quantities are considered dimensionless. As shown in Appendix A.1, the resulting resonator field magnitude is proportional to the magnitude of the pulse sequence, hence

$$|a(t)| \propto \sqrt{P_{\text{MW}}}, \quad (2.26)$$

which is illustrated by Figure 2.8. This implies for the dynamic magnetic field magnitude [45]

$$|B_1| \propto \sqrt{P_{\text{MW}}}. \quad (2.27)$$

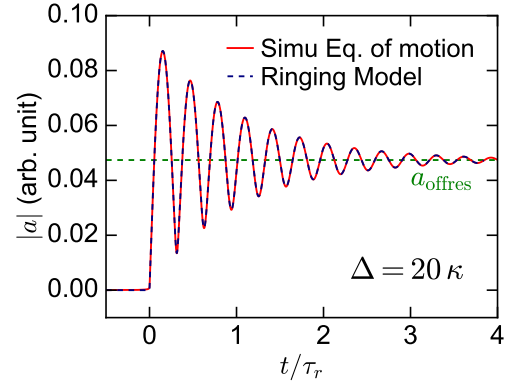


**Figure 2.7:** Offresonant ring up of resonator field  $|a|$  simulated with equation of motion (red curve) and calculated with ringing model (dashed blue curve) defined by Eq. (2.24) where  $a_{\text{offres}} = 0.0474$  and  $a_{\text{res}} = 0.0464$ .

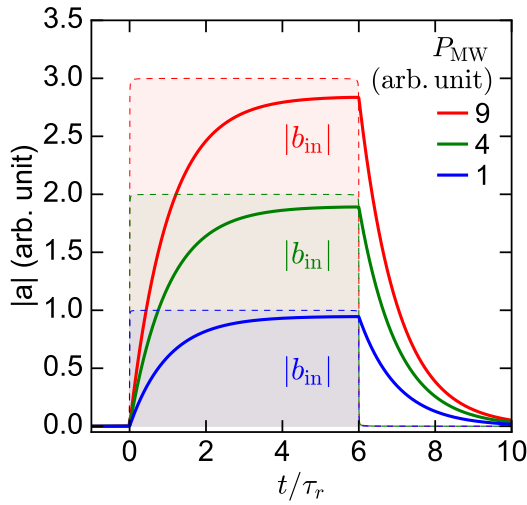


**Figure 2.8:** Simulated resonator field magnitude (bold curves) for different input microwave powers  $P_{\text{MW}}$  (arbitrary units) of a rectangular excitation pulse (thin dashed curves).

#### 2.1.4 Frequency Domain

The offresonant resonator ring up discussed in Section 2.1.3.4 indicates a finite bandwidth of the drive frequency  $\omega/2\pi$  for rectangular microwave pulses. In this section, we discuss rectangular and Gaussian pulse shapes in the time domain and frequency domain.

We define the input field of a rectangular pulse with length  $t_p$  via

$$b_{\text{in,Rect}} = \begin{cases} \sqrt{\frac{P_{\text{MW}}}{\hbar\omega}} e^{i\omega t} & \text{if } -\frac{1}{2} \leq \frac{t-t_0}{t_p} \leq \frac{1}{2} \\ 0 & \text{else} \end{cases}, \quad (2.28)$$

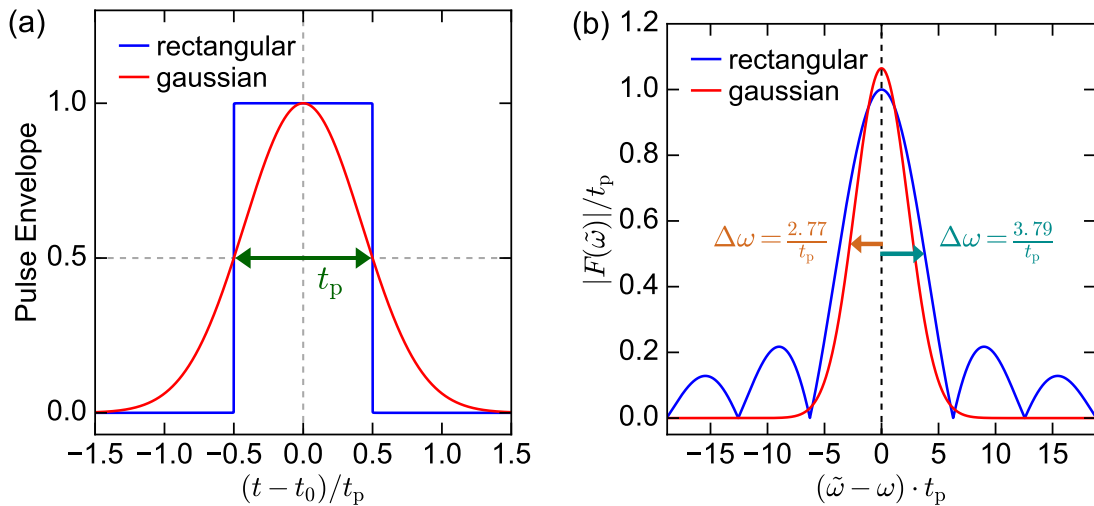


**Figure 2.9:** (a) Pulse envelope of rectangular and Gaussian pulse shapes as a function of time  $t$  (normalized to the pulse length  $t_p$ ). (b) Spectral distribution  $|F(\tilde{\omega})|$  as a function of detuning  $(\tilde{\omega} - \omega)$  from modulation frequency  $\omega$ . The x- and y-axis is normalized to  $t_p^{-1}$  and  $t_p$ , respectively.

and for Gaussian pulse shape<sup>1</sup>

$$b_{\text{in,Gauss}} = \sqrt{\frac{P_{\text{MW}}}{\hbar\omega}} \exp\left(-\frac{4\ln 2 \cdot (t - t_0)^2}{t_p^2}\right) e^{i\omega t}, \quad (2.29)$$

where  $t_0$  is the center of the pulse. Both pulse shapes are illustrated in Figure 2.9(a).

Figure 2.9(b) shows the corresponding Fourier transforms<sup>2</sup> of the two pulse types in the frequency domain given by<sup>3</sup>

$$F_{\text{Rect}}(\tilde{\omega}) = \sqrt{\frac{P_{\text{MW}}}{\hbar\omega}} t_p \text{sinc}\left(\frac{(\tilde{\omega} - \omega)t_p}{2\pi}\right), \quad (2.30)$$

$$F_{\text{Gauss}}(\omega) = \sqrt{\frac{P_{\text{MW}}}{\hbar\omega}} t_p \sqrt{\frac{\pi}{4 \cdot \ln 2}} \exp\left(-\frac{(\tilde{\omega} - \omega)^2 t_p^2}{16 \cdot \ln 2}\right). \quad (2.31)$$

Note that the Fourier transform is normalized in the frequency axis and amplitude to account for the time duration of the pulse  $t_p$ . We further analytically determine the half width at half maximum of the Fourier transform  $\Delta\omega$ . For the rectangular pulse, we find for  $\text{sinc}(\hat{x}) = 1/2$ ,  $\hat{x} \approx 0.603$ . Using Eq. (2.30), we obtain

$$\Delta\omega_{\text{Rect}} = \frac{2\pi\hat{x}}{t_p} \approx \frac{3.789}{t_p}. \quad (2.32)$$

For the Gaussian pulse, we solve

$$\exp\left(-\frac{\Delta\omega_{\text{Gauss}}^2 t_p^2}{16 \ln(2)}\right) = \frac{1}{2}, \quad (2.33)$$

which yields

$$\Delta\omega_{\text{Gauss}} = \frac{4\ln(2)}{t_p} \approx \frac{2.773}{t_p}. \quad (2.34)$$

Hence, for our definition of rectangular and Gaussian pulse shapes, the former exhibits a slightly broader linewidth in frequency domain.

Moreover, the spectral density of rectangular pulses is non-zero even for high deviations from  $\omega_0$  (see Figure 2.9(b)), which renders pulsed ESR experiments, which involve detuning from the resonator eigenfrequency, difficult.

Additionally, the ringing behaviour of the resonator field  $a$ , discussed in Section 2.1.3.4, is suppressed by Gaussian pulses (compare Figures 2.10 and 2.7).

---

<sup>1</sup> The factor  $4\ln 2$  ensures, that the full width at half maximum of the Gaussian pulse equals  $t_p$ . <sup>2</sup> We use the unitary Fourier transformation in ordinary frequency units. <sup>3</sup> Here we define the sinc function as  $\text{sinc}(x) = \sin(\pi x)/\pi x$ .

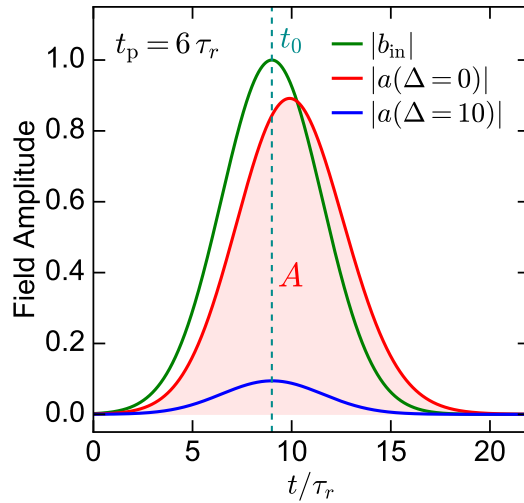


**Figure 2.10:** Resonator dynamics for Gaussian input field at different detuning  $\Delta$ . Red area illustrates the integrated resonator field  $A$  (see Eq. (2.35)).

### 2.1.5 Integrated Resonator Field

The manipulation of a spin system coupled to a resonator depends on the resonator field evolution throughout the excitation pulse. More precisely, for a drive pulse  $b_{in}$  at fixed frequency  $\omega/2\pi$  the quantity of interest is the integrated resonator field defined by

$$A := \int_{t_1}^{t_2} |a(t)| dt, \quad (2.35)$$

with appropriate integration limits  $t_1$  and  $t_2$  where  $a(t_1) = a(t_2) = 0$ .  $A$  is illustrated by the red area in Figure 2.10.

We explore the dependence of  $A$  on the pulse length  $t_p$  for the cases of resonant and offresonant excitation.

#### 2.1.5.1 Resonant Excitation

We assume a drive pulse  $b_{in}(t) = \tilde{b}_{in}(t) e^{i\omega t}$  with arbitrary pulse shape  $\tilde{b}_{in}(t) \in \mathbb{R}_{\geq 0}$  and nominal pulse length  $t_p$  and define its integral as

$$B_{in}(t_p) = \int_{t_1}^{t_2} \tilde{b}_{in}(t) dt, \quad (2.36)$$

This integral naturally scales linearly with the length of the excitation pulse  $t_p$ , i.e.

$$B_{in}(t_p) \propto t_p. \quad (2.37)$$

We find the resonator field  $a$  by solving the equation of motion for the given drive pulse and  $\Delta = 0$ . Due to excitation at resonance frequency, the phase shift between  $a$  and drive is zero.

Hence, we write  $a(t) = \tilde{a}(t)e^{i\omega t}$  with  $\tilde{a}(t) \in \mathbb{R}_{\geq 0}$  and find for the integrated resonator field

$$A = \int_{t_1}^{t_2} \tilde{a}(t) dt. \quad (2.38)$$

Next, we rewrite the equation of motion (see Eq. (2.3)) for  $\tilde{a}$

$$\dot{\tilde{a}}(t) = -\kappa \tilde{a}(t) + \sqrt{\kappa_{\text{ext}}} b_{\text{in}}(t), \quad (2.39)$$

and find with the fundamental theorem of calculus using equations 2.36 and 2.38

$$0 = \tilde{a}(t_2) - \tilde{a}(t_1) = \int_{t_1}^{t_2} \dot{\tilde{a}}(t) dt = \int_{t_1}^{t_2} [-\kappa \tilde{a}(t) + \sqrt{\kappa_{\text{ext}}} b_{\text{in}}(t)] dt = -\kappa A + \sqrt{\kappa_{\text{ext}}} B_{\text{in}}(t_p). \quad (2.40)$$

Solving this equation for  $A$  yields

$$A = \frac{\sqrt{\kappa_{\text{ext}}}}{\kappa} B_{\text{in}}(t_p). \quad (2.41)$$

In combination with Eq. (2.15) and Eq. (2.37) we obtain

$$A \propto \sqrt{P_{\text{MW}}} \frac{\sqrt{\kappa_{\text{ext}}}}{\kappa} t_p. \quad (2.42)$$

Finally, we establish a link to the spin manipulation in pulsed ESR experiments. In the simplified picture of a homogeneous  $B_1$ -field distribution, the rotation angle  $\theta$  in the Bloch sphere due to an excitation pulse is given by [44]

$$\theta = \int \gamma |B_1(t)| dt, \quad (2.43)$$

where  $\gamma$  is the gyromagnetic ratio and  $|B_1(t)|$  is proportional to the resonator field magnitude  $|a(t)|$ . Using Eq. (2.42) we find the relation

$$\theta = \int \gamma |B_1(t)| dt \propto A \propto \sqrt{P_{\text{MW}}} \frac{\sqrt{\kappa_{\text{ext}}}}{\kappa} t_p, \quad (2.44)$$

which shows the dependence of the magnetization rotation in the Bloch sphere on the resonator parameters ( $\kappa, \kappa_{\text{ext}}$ ), the microwave power  $P_{\text{MW}}$  and the pulse length  $t_p$ . This result was deduced for the case  $\Delta = 0$ .

### 2.1.5.2 Offresonant Excitation

For offresonant excitation  $\Delta \neq 0$ , relation 2.41 is generally not true as demonstrated in the following.

Figures 2.11(a) and (b) show the integrated resonator field  $A$  as a function of detuning for rectangular and Gaussian drive pulses with different lengths  $t_p$ , respectively.

In case of long  $t_p \ll \tau_r$ ,  $A(\Delta)$  is dominated by the steady-state resonator field (cf. Figure 2.2(a))

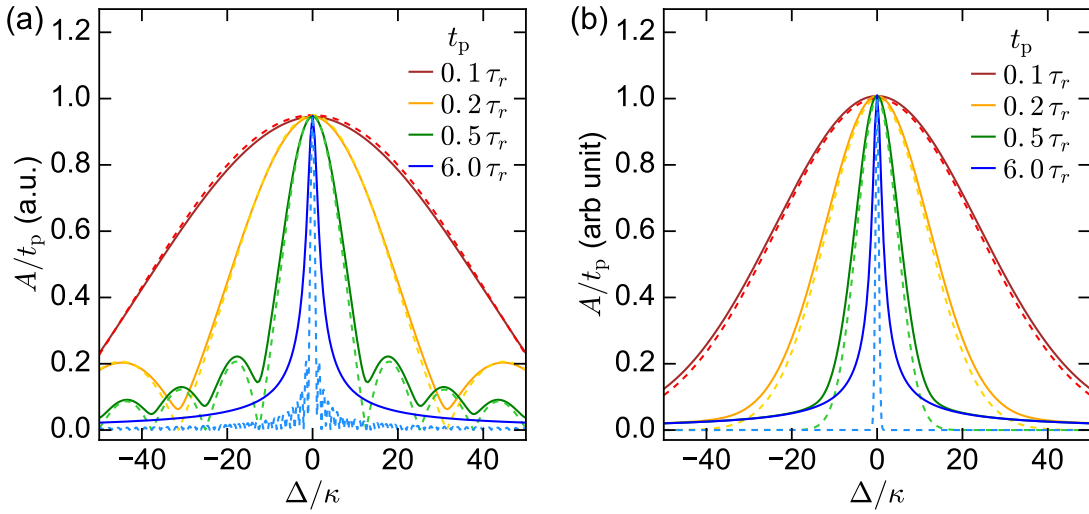


**Figure 2.11:** Integrated resonator field  $A$  (solid lines) as a function of detuning for different pulse lengths  $t_p$  simulated with rectangular (a) and Gaussian (b) shaped drive pulses.  $A$  is normalized to  $t_p$ . The spectral density functions (normalized to  $A(\Delta = 0)$ ) of the corresponding pulse shapes and lengths are depicted with dashed lines.

for both pulse shapes

$$A \propto |a(\Delta)| \cdot t_p. \quad (2.45)$$

For short  $t_p \ll \tau_r$ , the linewidth of  $A$  broadens. In this case, the shape of the integrated resonator field  $A(\Delta)$  is well-approximated by the spectral density function  $|F(\Delta)|$  of the respective pulse shape (dashed curves in Figure 2.11)

$$A \propto |F(\Delta)|. \quad (2.46)$$

Figure 2.11 reveals deviations from the relations 2.45 and 2.46, since in general, the integrated resonator field is obtained as convolution of the resonator transfer function and the spectral density function of the applied drive pulse.

### 2.1.6 Asymmetric Lineshape

In Sections 2.1.1 to 2.1.3 we developed a framework for describing the steady state excitation and dynamics of a resonator coupled to a transmission line. However, this framework does not cover asymmetric lineshapes observed in the experimental data. We model these non-symmetric resonance dips with the diameter correction method (DCM), which is based on the assumption of an impedance mismatch between the input and output impedance [46]. This method assumes a complex valued external coupling rate  $\kappa_{\text{ext}} \in \mathbb{C}$ , accounting for the impedance mismatch. We define the angle  $\varphi_r$  via

$$\kappa_{\text{ext}} = |\kappa_{\text{ext}}| e^{i\varphi_r}, \quad (2.47)$$

which is a measure for the asymmetry of a lineshape and typically assumes values between  $-20^\circ$  and  $20^\circ$ .

Consequently, we extend the framework described in Sections 2.1.1 to 2.1.3 by the complex val-

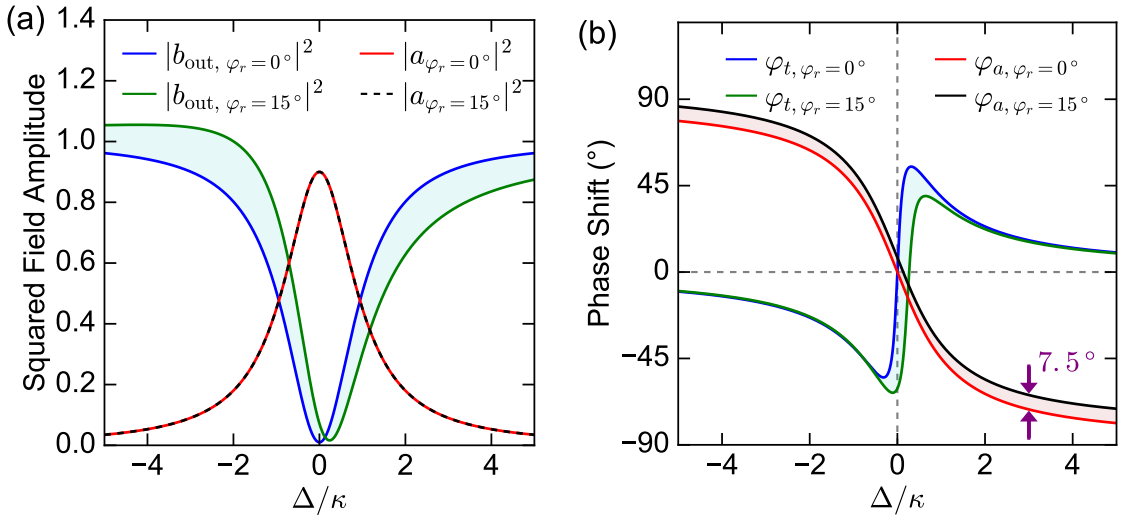


**Figure 2.12:** Simulated steady state of continuously driven ( $|b_{\text{in}}| = 1$ ) resonator with fixed parameters  $\kappa$ ,  $\kappa_{\text{ext}}$  and  $\omega_r$  for symmetric ( $\varphi_r = 0^\circ$ ) and asymmetric ( $\varphi_r = 15^\circ$ ) line-shapes. **(a)** Squared output and resonator field magnitude as a function of detuning  $\Delta$ . **(b)** Steady-state phase relation of output field  $b_{\text{out}}$  and resonator field  $a$  with respect to input field  $b_{\text{in}}$  as a function of detuning  $\Delta$ .

ued  $\kappa_{\text{ext}}$ . In particular, we find

$$Q_{\text{ext}}^{-1} = |Q_{\text{ext}}^{-1}| e^{i\varphi_r}, \quad (2.48)$$

and the relation of the Q-factors modifies to

$$\frac{1}{Q} = \text{Re} \left( \frac{1}{Q_{\text{ext}}} \right) + \frac{1}{Q_{\text{int}}} = \frac{\cos \varphi_r}{|Q_{\text{ext}}|} + \frac{1}{Q_{\text{int}}}. \quad (2.49)$$

Next, we compare symmetric and asymmetric lineshapes for a continuously driven resonator with fixed parameters  $\kappa$ ,  $\kappa_{\text{ext}}$  and  $\omega_r$  depicted in Figure 2.12. We observe a pronounced asymmetry in the power transmission for  $\varphi_r = 15^\circ$ , shifting the transmission minimum away from the nominal resonance frequency  $\omega_r/2\pi$ . We conclude, that the asymmetry parameter  $\varphi_r$ , in addition to  $\kappa$ ,  $\kappa_{\text{ext}}$  and  $\omega_r$ , is crucial for the correct description of resonance lineshapes.

We further observe, that the resonator field magnitude  $|a(\Delta)|$  is independent of  $\varphi_r$ . We explain this by considering the equation of motion (Eq. (2.3)):  $\varphi_r$  effectively shifts the phase of the drive tone experienced by the resonator by  $\varphi_r/2$ :

$$\dot{a} = (i\omega_r - \kappa) a + \sqrt{\kappa_{\text{ext}}} b_{\text{in}} = (i\omega_r - \kappa) a + \sqrt{|\kappa_{\text{ext}}|} e^{\frac{i\varphi_r}{2}} b_{\text{in}}. \quad (2.50)$$

However,  $|a(t)|$  is independent of the input field phase and does consequently not change upon variation of  $\varphi_r$ , as shown in Figure 2.12(a). Additionally, we observe the effective phase shift  $\varphi_r/2$  of the drive tone in  $\varphi_a(\Delta)$  (depicted in Figure 2.12), where the latter is increased by  $\varphi_r/2$  for all detuning values  $\Delta$ .

Finally, we consider the effect of asymmetric line shapes on the resonator dynamics. As illustrated by Figure 2.13, we find the resonator field magnitude  $|a(t)|$  to be independent of the asymmetry

parameter  $\varphi_r$ , as already shown in the steady-state case. This again is explained by the effective phase shift of the resonator demonstrated by Eq. (2.50), which has no influence on the excitation dynamics. However, in contrast to  $|a(t)|$ , the output field transient  $|b_{\text{out}}(t)|$  is dependent on  $\varphi_r$  (not shown here).

As motivated in this section, we employ the DCM model for description of all measured and simulated resonance lineshapes and excitation dynamics in the remainder of this thesis.

## 2.2 Phosphorus doped Silicon

In this section, we consider the spectroscopic features of isolated phosphorus donors in a silicon crystal. Atoms in crystalline silicon are arranged in the diamond structure and have four covalently bonded next neighbours. Incorporating a phosphorus  $^{31}\text{P}$  atom into the silicon crystal by substitution of a silicon atom leaves one of the five valence electrons of  $^{31}\text{P}$  unbound, providing an unpaired spin  $S = 1/2$ . This spin is subjected to the Fermi contact hyperfine interaction with the nuclear spin  $I = 1/2$  of the phosphorus atom, in addition to the Zeeman interaction to the static magnetic field  $B_0$ . Assuming  $B_0$  in the direction of the z-axis, the Hamiltonian of this system is given by

$$H = \frac{g_{\text{ep}}\mu_{\text{B}}}{\hbar}B_0S_z + \frac{g_{\text{n}}\mu_{\text{N}}}{\hbar}B_0I_z + \frac{A}{\hbar^2}\mathbf{S}\mathbf{I}, \quad (2.51)$$

with the electron ( $g_{\text{ep}} = 1.9985$ ) and nuclear g-factor ( $g_{\text{n}} = 2.2632$ ) [47, 48], the Bohr (nuclear) magneton  $\mu_{\text{B}}$  ( $\mu_{\text{N}}$ ), the electron ( $\mathbf{S}$ ) and nuclear spin ( $\mathbf{I}$ ), and the hyperfine interaction constant  $A = h \cdot 117.53 \text{ MHz}$  [9]. The first (second) term of Eq. (2.51) describes the Zeeman interaction of the electron (nuclear) spin with the static magnetic field  $B_0$ , and the last term describes the hyperfine interaction between electron and nuclear spin. Solving the Hamiltonian yields four eigenstates with the energies  $E_1$ ,  $E_2$ ,  $E_3$  and  $E_4$  given by

$$E_1 = \frac{A}{4} + \frac{B_0}{2}(g_{\text{ep}}\mu_{\text{B}} + g_{\text{n}}\mu_{\text{N}}), \quad (2.52)$$

$$E_2 = -\frac{A}{4} + \frac{1}{2}\sqrt{A^2 + B_0^2(g_{\text{ep}}\mu_{\text{B}} - g_{\text{n}}\mu_{\text{N}})^2}, \quad (2.53)$$

$$E_3 = \frac{A}{4} - \frac{B_0}{2}(g_{\text{ep}}\mu_{\text{B}} + g_{\text{n}}\mu_{\text{N}}), \quad (2.54)$$

$$E_4 = -\frac{A}{4} - \frac{1}{2}\sqrt{A^2 + B_0^2(g_{\text{ep}}\mu_{\text{B}} - g_{\text{n}}\mu_{\text{N}})^2}. \quad (2.55)$$

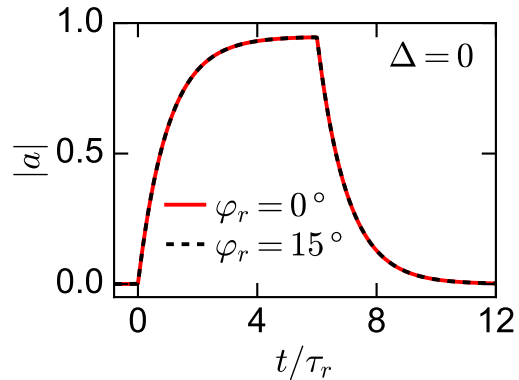


**Figure 2.13:** Excitation dynamics simulated with symmetric and asymmetric lineshape for rectangular pulse and fixed  $\kappa$ ,  $\kappa_{\text{ext}}$  and  $\omega_r$ .

The eigenenergies are illustrated in a Breit-Rabi diagram in Figure 2.14.

Due to the spin angular momentum  $\pm\hbar$  of the photon, an excitation between two different spin states is possible. This gives rise to nuclear magnetic resonance (NMR) and electron spin resonance (ESR) corresponding to nuclear and electron spin-flips, respectively. One typically uses MHz frequencies for NMR experiments, while ESR transitions are typically associated with the GHz regime. In this thesis we are interested in ESR transitions probed using microwave resonators with GHz resonant frequencies. The green arrows in Figure 2.14 illustrate the two possible ESR transitions with equal resonance frequency  $\omega/2\pi$ . These transitions are separated by a static magnetic field difference of 4.2 mT (red arrow), which is characteristic for an isolated phosphorus donor in a silicon host crystal.

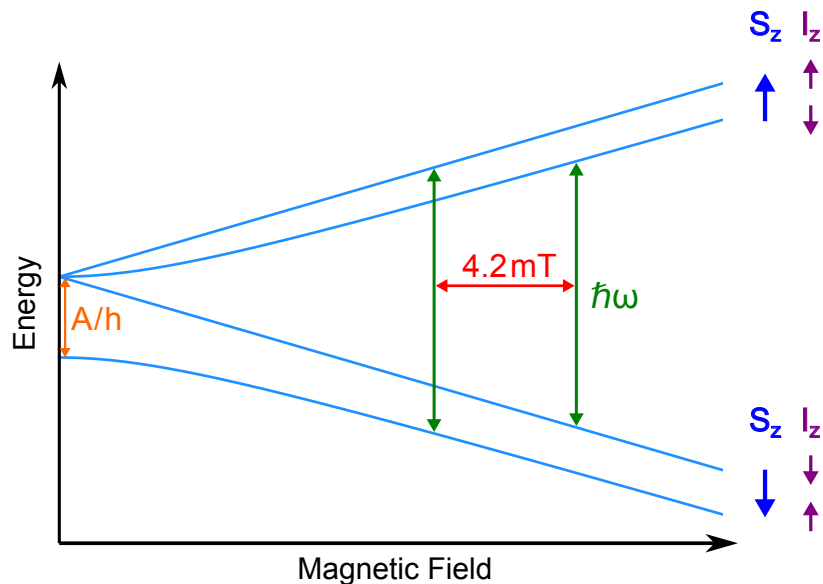


**Figure 2.14:** Schematic Breit-Rabi diagram of isolated phosphorus in silicon. The eigenenergies of the Hamiltonian are plotted against the static magnetic field (light blue lines). The green arrows show the possible ESR transitions with same resonance frequency  $\omega/2\pi$ . The two hyperfine split transitions are separated by 4.2 mT. The orange arrow marks the hyperfine splitting at zero field between the degenerate triplet and the singlet state.



# Chapter 3

## Methods

In this section, we describe the fabrication process for superconducting microwave resonators, the sample mounting and the experimental setup for continuous wave and time domain measurements.

### 3.1 Fabrication of Niobium Resonators with Aluminum-coating

We present a fabrication process for aluminum-coated niobium microstructures deposited and patterned on a silicon substrate, which enables superconducting microwave resonators with high internal quality factors in the order of  $2 \cdot 10^5$ . The quality factor is essentially dependent on the cleanliness of material surfaces prior to each process step. We use an *in situ* sputtered aluminum layer of 10 nm thickness to protect the niobium from oxidation, and thus preventing a degradation of the resonator quality over long periods of time.

The material layers involved in the fabrication are shown in Figure 3.1(a). The successive steps of the process are illustrated in Figure 3.1(b).

We use a highly resistive silicon substrate ( $>10\text{ k}\Omega/\text{cm}$ ) with a thickness of  $525\text{ }\mu\text{m}$  and in-plane dimensions of  $6 \times 10\text{ mm}^2$ . Using *in situ* sputtering without prior surface treatment of the substrate, we deposit 150 nm of niobium covered with a 10 nm layer of aluminum. Next, the chip surface is coated with an adhesion promoter and a bilayer of the positive electron-beam resist AR-P 6200.04 (short CSAR) with a spin coater. The double layer of resist is needed to withstand the three following etching steps. The chip layout is patterned into the resist with Electron-Beam Lithography (EBL) and developed with the moderate developer AR 600-549. Then, resist residuals are removed from the aluminum surface using argon ion milling (see Figure 3.1(b)). The aluminum in the patterned areas is etched in a wet-chemical step using the optical developer AZ-726 MIF with a concentration of 2.38 % Tetra-Methyl-Ammonium-Hydroxide (TMAH). We further use reactive ion etching (RIE) in a 15 mTorr  $\text{SF}_6/\text{Ar}$  atmosphere with a radio frequency (RF) power of 100 W for etching the niobium. Finally, we remove the undeveloped resist with the remover AR 600-71 in ultrasonic bath.

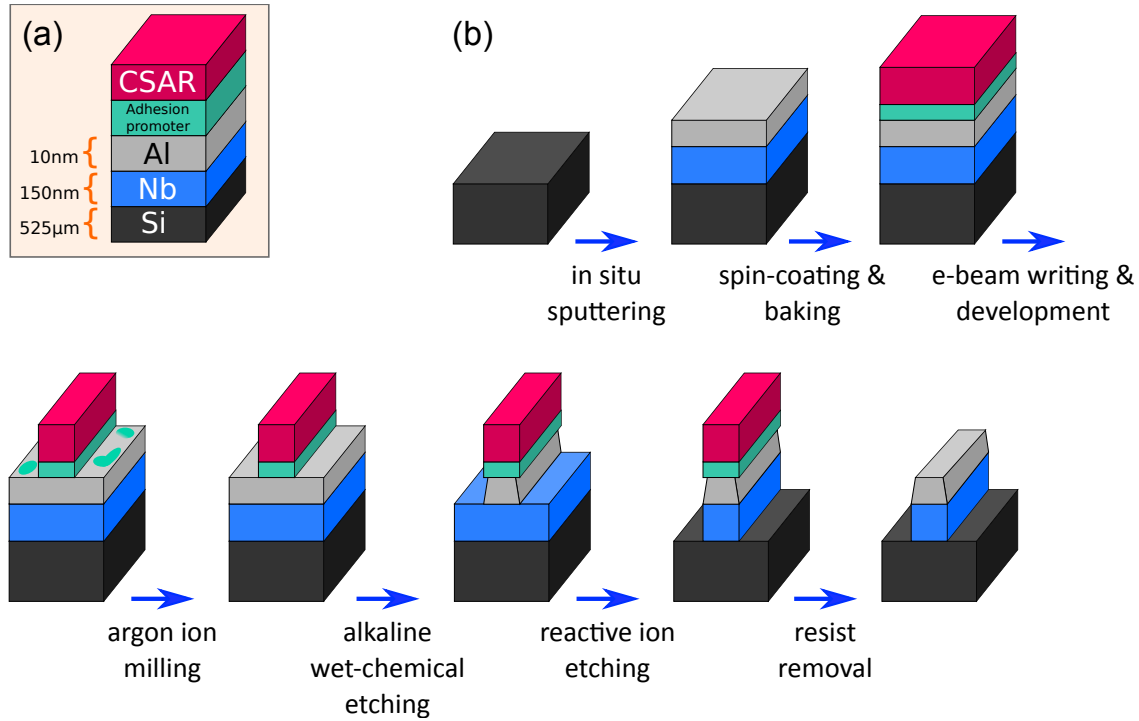


**Figure 3.1:** (a) Illustration of material layers involved in the fabrication process. (b) Illustration of the successive steps of the fabrication process.

Argon ion milling represents the key step of this fabrication process, cleaning the aluminum surface from the resist residuals before the wet-chemical etching is conducted. Applying the wet-chemical step without prior cleaning of the surface leads to a collapsed process window, as a long wet-chemical etching time leads to underetching of the aluminum beneath undeveloped areas of the resist, whereas a short etching time leaves aluminum residuals on the silicon surface, which are resilient against reactive-ion etching. This results in rough silicon surfaces, which decrease the quality factor of the resonator.

### 3.2 Sample Preparation

In this section, we describe the assembling of the resonator chip, the spin marker and the sample containing the spin system into a copper sample box.

After passing through the fabrication process, the chip surface is cleaned with acetone in ultrasonic bath and dried with compressed nitrogen. A clean surface is essential for achieving a good coupling between the resonator and the spin system. Using silver glue, the  $6 \times 10 \text{ mm}^2$  chip is attached to the floor of a copper box as illustrated in Figure 3.2(a).

The two ground planes of the chip located on both sides of the transmission line center conductor are shorted to the box by depositing silver glue at the borders of the chip surface. Additionally, two SMA microwave connectors are inserted from either side of the box, such that the metal pad with sub millimeter width exhibits a small gap to either of the ends of the transmission line center conductor. The metal pads are electrically connected to the center conductor of the transmission line by partly filling the gap with silver glue, making use of the capillary action, without

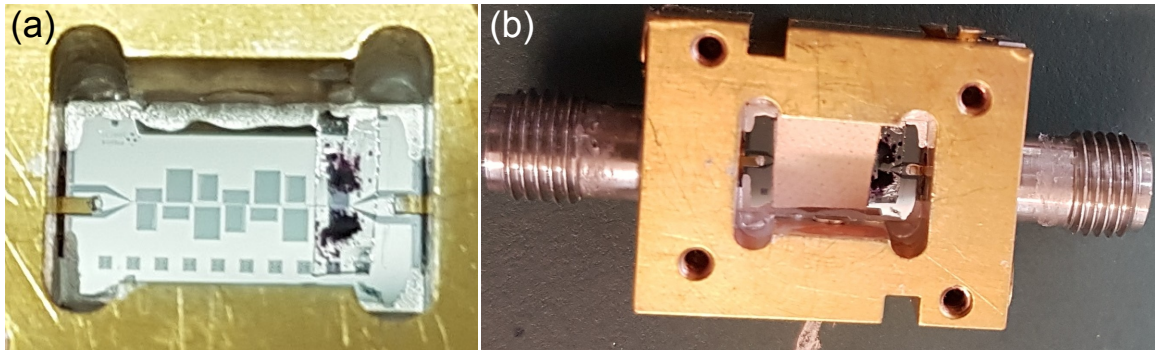


**Figure 3.2:** (a) Resonator chip attached to the bottom of the copper box with contacted metal pads of the microwave contacts and mounted DPPH on two of the resonators using adhesive tape. (b) Copper box after placing the phosphorus doped silicon sample in flip-chip geometry on the chip surface.

shorting the center conductor to the ground plane. It is highly recommended to tightly screw the microwave contacts onto the box, before contacting them to the transmission line, otherwise the connection might be damaged, when attaching the chip to the microwave circuitry.

We cover two resonators of the chip with the spin marker DiPhenyl-Picryl-Hydrazyl (DPPH) [49], which is used for calibration of the static magnetic field. It is important to avoid the coverage of other resonators and the signal line due to the strong ESR signal expected for this spin marker as a consequence of a high density of spins [49]. We used DPPH in the form of pressed powder, which was attached to the chip surface with adhesive tape. Liquid adhesive is not suited for this purpose, since DPPH diffuses within liquid substances, and thus spreads over the chip surface.

The phosphorus doped silicon crystal is mounted onto the surface of the chip, next to the resonators covered with DPPH (see Figure 3.2(b)). To this end, an adhesive tape is attached to the backside of the sample, before placing it in flip-chip geometry onto the chip surface. Next, the cover of the box is fixed with four screws. Moreover, the box cover has a threaded hole in its center, which is now used for tightly fixing the sample onto the surface of the chip using a copper screw. The adhesive tape between the screw and the sample acts as a buffer for thermal expansion of the components. It is crucial, to use the same material for the box and the screw fixing the sample, in order to minimize the relative thermal compression between both components. With this mounting technique, we were able to realize close-to-perfect filling factors for a bulk sample (cf. Section 5.1.3).

### 3.3 Measurement Setups

#### 3.3.1 Continuous Wave Setup

A Vector Network Analyzer (VNA) is the heart of the continuous wave measurement setup. It functions as both a generator and detector for microwave signals at the same time, and allows to measure the scattering parameters of a circuit, i.e. the reflection on one microwave port or the

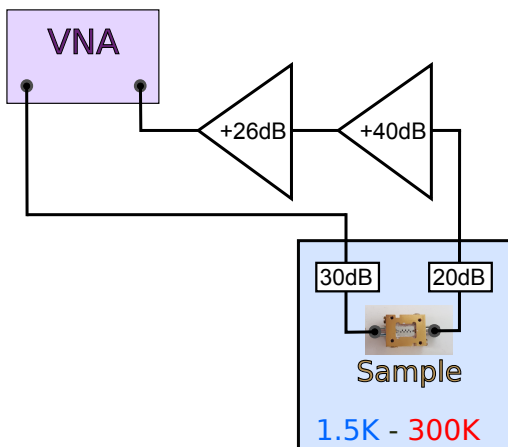


**Figure 3.3:** Schematic of the microwave circuit of the continuous wave measurement setup.

transmission between two ports. In the following, we introduce the concept of the continuous wave measurement setup, illustrated by Figure 3.3.

The setup is designed for measuring the microwave transmission through a superconducting transmission line coupled to a lumped element microwave resonator, which in turn is coupled to a paramagnetic spin ensemble. However, the spin system under investigation typically exhibits saturation effects for microwave powers<sup>4</sup> at sample in the order of  $-100$  dBm or higher at  $1.5$  K (see Section 5.2). Furthermore, the thermal noise at room temperature corresponds to a noise power of  $\approx -106$  dBm for a resonator linewidth of  $3$  MHz [50]. In order to prevent saturation, we add cold attenuators into the cryostat at both the input ( $30$  dB) and the output signal path ( $20$  dB), which are cooled to sample temperature. This effectively suppresses room temperature microwave noise photons to saturate the sample. To compensate this attenuation and raise the signal level to the dynamic range of the VNA, we use low noise preamplifiers (*MITEQ ASF5* and *Kuhne KU LNA BB 202 A*) at room temperature, prior to detecting the signal with the VNA. For reaching low sample powers down to  $-125$  dBm, we employ for most measurements an Agilent PNA-X N5242A with a built-in step attenuator, which is able to provide output powers between  $-95$  dBm and  $19$  dBm in the relevant frequency range.

### 3.3.2 Time Domain Setup

The concept of the time domain setup is based on an Arbitrary Waveform Generator (AWG), which enables to apply arbitrary pulse shapes and sequences to the spin system via the microwave resonator. However, the pulses are typically generated at MHz frequencies and require a conversion to the GHz range. On the other hand, signal detection is limited to MHz signals, which requires a downconversion of the transmitted microwave transients. This functionality is managed by the microwave circuit depicted in Figure 3.4. Additionally, a VNA can be used to perform continuous wave measurements (cf. Section 3.3.1) for convenient adjustment of the drive frequency and the applied static magnetic field. In the following, we describe the signal path from generation to detection based on Figure 3.4.

<sup>4</sup> In this thesis, microwave powers are typically given in decibel-milliwatts. A power value in milliwatts  $P[\text{mW}]$  is converted to decibel-milliwatts via  $P[\text{dBm}] = 10 \log_{10}(P[\text{mW}])$ .

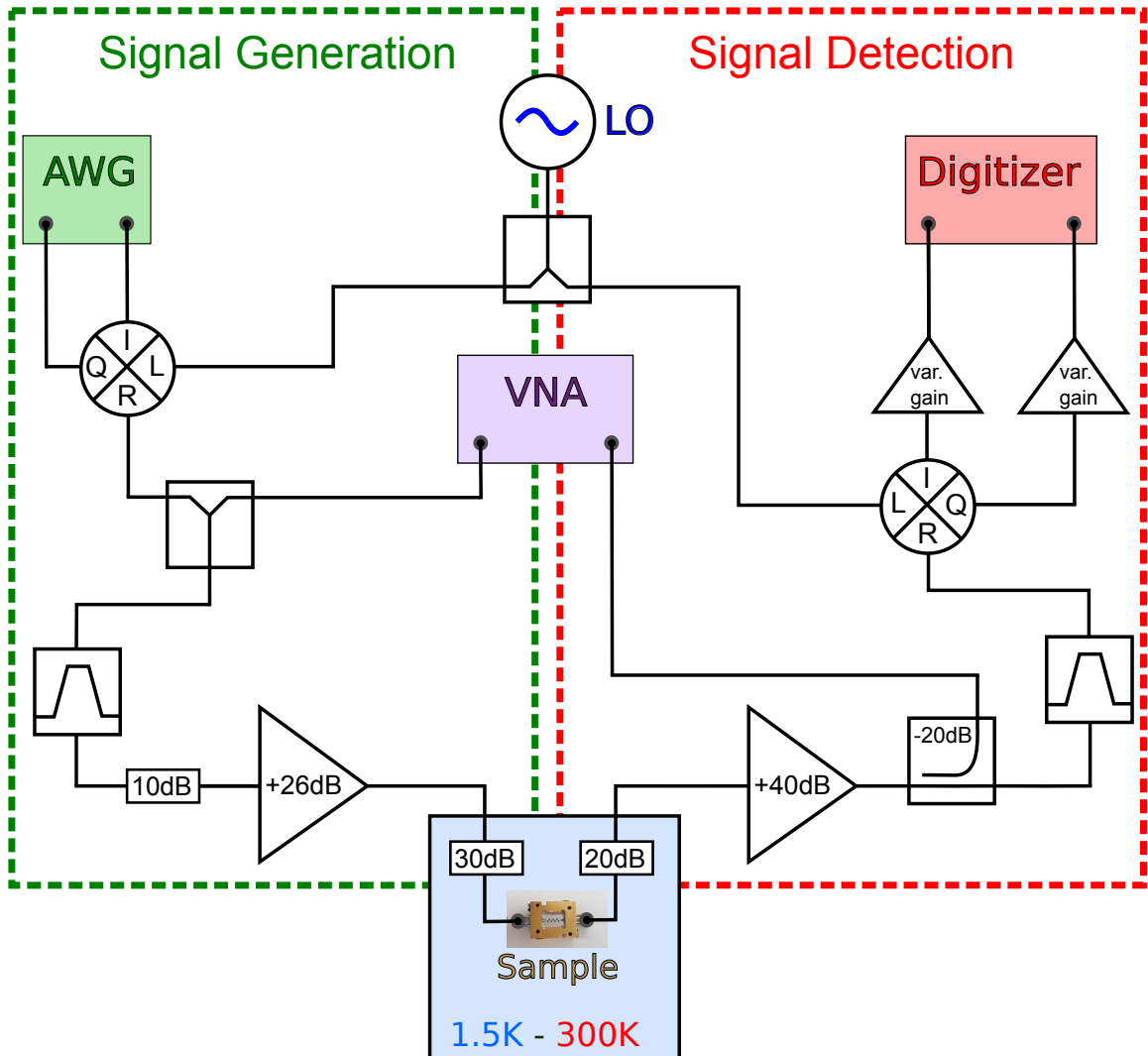


**Figure 3.4:** Schematic of the microwave circuit of the time domain measurement setup with integrated continuous wave measurement capability. With the time domain signal generation, a maximal power of around

The AWG (Agilent M8190A) generates the in-phase ( $I$ ) and quadrature component ( $Q$ ) of a waveform at an intermediate frequency  $f_{IF} = 42.5\text{ MHz}$ . The IQ mixer (Marki MLIQ 0218L) is used as a single sideband (SSB) mixer, which mixes the quadratures  $I$  and  $Q$  with the local oscillator signal at frequency  $f_{LO}$  (supplied by an AGILENT E8267D frequency source), resulting in a radio frequency signal at  $f_{IF} + f_{LO}$ . Due to the  $90^\circ$  phase shift between  $I$  and  $Q$ , the contributions from both quadratures superpose constructively at the frequency  $f_{IF} + f_{LO}$  after upconversion, while they cancel at the lower sideband  $f_{IF} - f_{LO}$ . Next, a power divider (PD-0220) combines the signal paths of the time domain signal and the VNA output port, allowing the alternate use of either measurement technique without modifications to the circuitry.

The signal is filtered outside the frequency range of 3.5 GHz to 4.5 GHz by a band-pass filter *Mini-Circuits VBFZ-4000+* and attenuated by 10 dB, in order to prevent saturation of the subsequent amplifier (*Kuhne KU LNA BB 202 A*). In analogy to the continuous wave setup, the microwave signal is transmitted through the cold attenuators and the sample within the cryostat.

On the signal detection side, we amplify the signal using a low-noise amplifier (*MITEQ ASF5*). Thereafter the signal is splitted into two paths by a 20 dB coupler. The attenuated signal path is connected to the input port of the VNA, while the transmitted part of the signal is filtered by a band-pass filter. In a next step, the signal is downconverted to intermediate frequency by an IQ mixer (*Marki MLIQ 0218L*) yielding the quadratures  $I$  and  $Q$ . These signals are amplified by an IF amplifier (*FEMTO DHPVA-200*) with variable gain between 10 dB and 60 dB and finally digitized using a fast 1 GS/s digitizer (Gage Eon CompuScope CS121G2).

The signal of the local oscillator is split by a power divider and thus provided to both IQ mixers, ensuring a phase coherent LO signal. Additionally, the AWG and digitizer are synchronized to the temperature-stabilized 10 MHz reference oscillator of the local oscillator.

Single shot pulsed ESR measurements at liquid helium temperatures are not feasible due to the low signal-to-noise ratio, which can be improved by averaging several shots into a single transient. This is realized such that the digitizer card triggers each shot of the AWG.

Finally, the power at sample is adjusted via the AWG power  $P_{\text{AWG}}$ , which allows output powers between  $-10 \text{ dBm}$  to  $10 \text{ dBm}$  output, while the output power of the local oscillator is fixed at  $15.4 \text{ dBm}$ . However, due to attenuation and amplification along the signal path to the sample, there is a constant offset between the AWG and the sample power  $P_s$  power. A power calibration performed with a power meter yields

$$P_s = P_{\text{AWG}} - 22 \text{ dB}. \quad (3.1)$$

The maximal sample power is  $-12 \text{ dBm}$ , which corresponds to an input power of  $P_{\text{input}}^{\text{Kuhne}} = -12 \text{ dBm} + 30 \text{ dBm} - 26 \text{ dBm} = -8 \text{ dBm}$  at the *Kuhne KU LNA BB 202 A*. This is well below the specified maximal input power of  $\approx 0 \text{ dBm}$  for this amplifier.

The detected quadratures with intermediate frequency  $f_{\text{IF}}$  are demodulated in software, as described below.

### 3.4 Heterodyne Signal Detection

In this section, we present the software postprocessing of the quadratures  $I$  and  $Q$  acquired with the time domain setup. Neglecting contributions of noise, we assume  $I$  and  $Q$  to take the form

$$I(t) = A(t) \sin(2\pi f_{\text{IF}} t + \varphi), \quad Q(t) = A(t) \cos(2\pi f_{\text{IF}} t + \varphi), \quad (3.2)$$

where  $A(T)$  is the envelope of the modulation,  $f_{\text{IF}} = 42.5 \text{ MHz}$  is the modulation frequency and  $\varphi$  accounts for the phase shift due to the run time of microwave signals as well as for the phase relation of the transmitted signals ( $I$ ,  $Q$ ) with respect to the drive signal. In general,  $\varphi$  can be time-dependent, for instance when considering the resonator transmission during an excitation pulse, as shown in Figure 2.4. In this case, we are interested in the envelope  $|A(t)|$  of  $I$  and  $Q$ , which is given by

$$\sqrt{I^2(t) + Q^2(t)} = |A(t)| \sqrt{\sin^2(2\pi f_{\text{IF}} t + \varphi(t)) + \cos^2(2\pi f_{\text{IF}} t + \varphi(t))} = |A(t)|. \quad (3.3)$$

When considering the record of a typical spin echo,  $\varphi$  is a constant and we can apply a phase-sensitive demodulation. To this end, we neglect the quadrature  $Q$ , since both quadratures carry redundant information as shown by Eq. (3.2). First, we apply a band-pass filter with a total bandwidth of 10 MHz, which exceeds the resonator and the spin system linewidth, to reduce the noise in  $I$ . Next, we demodulate  $I$  via

$$I_{\text{demod}} = A(t) \cdot \sin(2\pi f_{\text{IF}} t + \varphi). \quad (3.4)$$

According to the trigonometric addition theorems,  $I_{\text{demod}}$  is a superposition of a dc signal and a signal at a frequency of  $2f_{\text{IF}}$ . The latter is suppressed by applying a 10 MHz low-pass filter. Thus, we obtain the demodulated dc signal  $S(t)$ .

However, in the first place,  $\varphi$  is a free parameter in Eq. (3.4), as the phase relation of the quadrature is unknown. We find the optimal phase  $\varphi_{\text{opt}}$  by maximizing the integrated demodulated signal, which corresponds to the echo area

$$A_{\text{echo}} = \int S(t) dt. \quad (3.5)$$

Additionally, when recording a series of echo signals, it is sufficient to find  $\varphi_{\text{opt}}$  once, and fix it for further demodulations. Finally, the phase-sensitive demodulation can reproduce negative echo areas. Here, one needs to identify a reference echo with a positive echo area, in order to obtain a value for  $\varphi_{\text{opt}}$ , which can then be applied to the other recorded transients. A typical example is the inversion recovery experiment (cf. Section 6.2.4), where short wait times  $T$  between the inversion pulse and the Hahn echo sequence are expected to result in negative echo areas. Here,  $\varphi_{\text{opt}}$  can be determined based on an inversion recovery sequence with very long values of  $T$ , which is expected to lead to an echo signal in phase with the drive pulse sequence, i.e. a positive echo area  $A_{\text{echo}}$ .



## Chapter 4

# Resonator Designs and Pre-characterization

In magnetic resonance experiments with microwave resonators, the tailoring of resonator geometry and parameters is essential for the outcome of the performed measurements. In general, different experimental techniques impose individual requirements on a resonator. One prominent resonator concept is the coplanar waveguide resonator (CPWR), which was widely investigated in the past decades [51, 52]. In principle, the CPWR is composed of a waveguide, whose resonance condition is tuned by geometrical features, like for instance, strip ends that are isolated from or shorted to the ground, which give rise to standing electromagnetic waves along the waveguide [53].

In this thesis we specifically investigate the design of lumped element resonators (LER) for electron spin resonance (ESR). A typical LER is described as a microscopic series LC-circuit with clearly separated geometric structures hosting the resonator's inductance and capacitance. In contrast, the operating principle of a CPWR can only be understood in the framework of a waveguide. Compared to the CPWR, the LER enables smaller in-plane dimensions, which correspond to a natural protection against static magnetic field inhomogeneities, which is favorable for ESR measurements. Additionally, the LER allows for a large freedom in its geometric design.

We present three different LER design concepts in Section 4.1. We investigate the general working principles and the tunability of resonator parameters, particularly focusing on the external coupling as well as the dynamic magnetic field distribution.

We experimentally realize the three resonator designs on one sample chip. In particular, the chip contains a total of 14 microwave resonators coupled to one transmission line. In a next step, we characterize the resonator properties depending on the applied operation conditions, namely temperature, static magnetic field and drive power.

In Section 4.3, we introduce and verify the time domain measurement setup. Finally, we show the prediction power of resonator dynamics simulations, which are based on the exact knowledge of resonator parameters in combination with the equation of motion, describing the coupled system of resonator and transmission line (cf. Section 2.1.1).

## 4.1 Lumped Element Resonators

We explore the capacitively shunted meander resonator (CR) design as a starting point for the understanding of a LER's working principle as well as for developing further design concepts. Various ESR experiments have been reported with this resonator type, including strong coupling to a paramagnetic spin ensemble at millikelvin temperatures [32, 54, 55].

Based on our understanding of the CR resonator, we introduce the meander resonator, which has no deliberately designed capacitive element. Finally, we present the novel concept of a spiral resonator, aiming for improved homogeneity of the dynamic magnetic field. For each design, we focus on the tunability of the resonance frequency, supported by systematic finite element method (FEM) simulations, and give an estimation of the electromagnetic properties, i.e. the resonators inductance and capacitance, based on simple geometric models. Additionally, we discuss how the resonator couples to the microwave signal line and present how and to which extend this coupling can be controlled. Finally, we investigate the dynamic magnetic field based on FEM simulations and discuss the advantages of designs for different ESR experiments.

### 4.1.1 Capacitively Shunted Meander Resonator

The capacitively shunted meander resonator is a typical LER with sub millimeter in-plane dimensions. As illustrated in Figure 4.1, the resonator structure is patterned into a ground plane, close to the center conductor of an end-to-end coplanar waveguide (CPW).

The CPW impedance is tuned to  $50\Omega$  by choosing the width of the center conductor  $w = 20\mu\text{m}$  and its gap to the ground plane  $s = 12\mu\text{m}$  [56]. This CPW acts as a transmission line coupled to the LER. The LER is an absorption type resonator, i.e., when a microwave signal propagating in the CPW matches the resonance condition of the resonator, the signal transmitted through the CPW is reduced.

The CR features a meandering structure and an interdigital capacitor containing the resonators inductance  $L$  and capacitance  $C$ , respectively. The meander section is defined by the strip width  $w_s = 5\mu\text{m}$  and the pitch  $p = 30\mu\text{m}$  given by the center-to-center separation of neighbouring strip sections, whereas the capacitor is parametrized by the width of fingers  $w_{\text{cap}} = 10\mu\text{m}$ , their spacing  $s_{\text{cap}} = 15\mu\text{m}$  and by the length  $l_{\text{cap}}$  of one of the fingers, which will act as a tuning parameter for the resonance frequency.

In a simplified picture, the LER is described by an RLC-circuit with very low resistance  $R$ , accounting for the resonator's internal losses and the above mentioned quantities  $L$  and  $C$ . Therefore, the resonant frequency is well approximated by [57]

$$f_r = \frac{1}{2\pi\sqrt{LC}}. \quad (4.1)$$

A propagating drive tone in the CPW induces a current in the resonator strip due to their mutual inductance. As is well-known for the LC-circuit, both, the current  $I(t)$  in the meander structure and the capacitor voltage  $V(t)$  typically oscillate with the drive frequency. The total excitation energy of the resonator  $E = \frac{1}{2}LI_{\text{max}}^2$  is transferred from magnetic to electric energy and vice versa

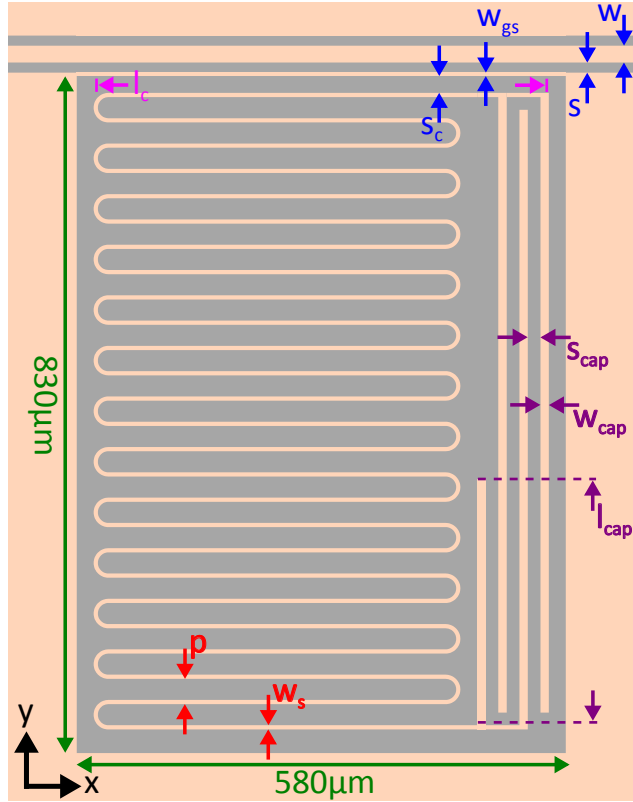


**Figure 4.1:** Layout of the capacitively shunted meander resonator patterned into one of the ground planes of a coplanar waveguide. The conductor and the substrate material are illustrated with light orange and grey color, respectively. The characteristic parameters are shown in Table 4.1. The total strip length is around 13 mm.

Parameter	Dimension ( $\mu\text{m}$ )
$w$	20
$s$	12
$w_{gs}$	5
$s_c$	20
$l_c$	540
$w_s$	5
$p$	30
$w_{cap}$	10
$s_{cap}$	15
$l_{cap}$	300

**Table 4.1:** Geometric parameters of the CR as shown in Figure 4.1. The parameters  $l_{cap}$  and  $w_{gs}$  are varied for tuning the resonance frequency and the external coupling rate, respectively.

within one oscillation period.

Inherent to the meandering structure is the alternating current direction in neighboring strip sections, which leads to the dynamic magnetic field  $\mathbf{H}_1$  illustrated in Figure 4.2, in particularly superposing in between strip sections. The dynamic excitation field is essential for the interaction of the resonator with paramagnetic spins in ESR experiments (further discussed in Section 4.1.5). However, the alternating current also gives rise to an inductive coupling between neighboring strip sections, which alters the total inductance of the LER compared to the unperturbed line inductance as discussed below.

We estimate the inductance and capacitance of the CR based on its geometric structure.

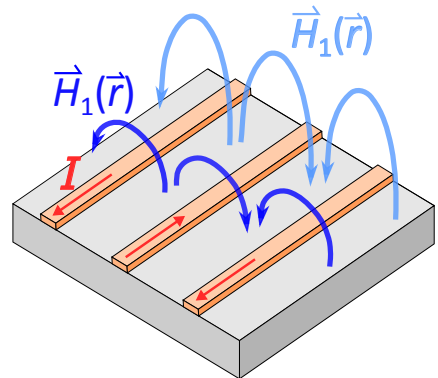


**Figure 4.2:** Schematic of the dynamic magnetic field (light and dark blue arrows) generated by neighbouring strip sections with alternating current directions (red arrows).

In general, there are two contributions to the inductance of a microstrip. The first one is the self-inductance  $L_{\text{self}}$ , which scales predominantly with the total strip length. The CR is designed to a total length of  $l_{\text{tot}}^{(\text{CR})} = 13.0 \text{ mm}$ , which here includes twice the length of a capacitor finger. Using the strip width  $w = 5 \mu\text{m}$  and thickness  $d = 150 \text{ nm}$ , Eq. (A.8) yields  $L_{\text{self}}^{(\text{CR})} = 23.5 \text{ nH}$ . The second contribution is the mutual inductance  $M$ , which in general is based on electromagnetic inductance between neighbouring strip sections. For the CR,  $M$  is obtained by multiplying the number of neighbouring sections with the mutual inductance between two sections. The latter is estimated with the geometric mean distance (GMD) method [58], which results in a total mutual inductance of  $M^{(\text{CR})} = 4.9 \text{ nH}$ . Furthermore, the total inductance takes the form

$$L = L_{\text{self}} \pm 2M , \quad (4.2)$$

where the sign of  $M$  depends on the relative current direction of neighbouring strips. In the case of the CR with opposing directions, the mutual inductance reduces the total inductance, therefore we find  $L^{(\text{CR})} = 13.7 \text{ nH}$ .

For estimating the capacitance  $C$ , we consider the dielectric environment of the interdigital capacitor, which is a silicon ( $\epsilon_r = 11.7$ ) and a vacuum ( $\epsilon_r = 1$ ) half space, resulting in an effective permittivity of  $\epsilon_{\text{eff}} = 6.35$ . Assuming a plate capacitor is an unsuitable model due to the low thickness  $d = 150 \text{ nm}$  of the plates compared to their large distance of  $15 \mu\text{m}$ . Instead, we assume two thin wires and find with Eq. (A.9) the capacitance  $C^{(\text{CR})} = 61 \text{ fF}$  for  $l_{\text{cap}} = 300 \mu\text{m}$ . Combining the estimated values of  $L$  and  $C$  with Eq. (4.1), we estimate the resonance frequency of the CR to  $f_r^{(\text{est.})} = 5.5 \text{ GHz}$  for  $l_{\text{cap}} = 300 \mu\text{m}$ . This is in very good agreement with the measured value  $f_r^{(\text{meas.})} = 5.15 \text{ GHz}$  (see Figure 4.3(a)), taking into account the simplicity of the employed models for  $L$  and  $C$ . Additionally, the electromagnetic properties of simple microstructures are crucially altered, when assembling them to more complex structures like a LER [57].

Next, we present finite element method (FEM) simulations of the resonator layout and compare them to our measurements. In general, we perform FEM simulations in order to access the microwave transmission through the CPW coupled to LERs as well as extract three dimensional dynamic electric and magnetic fields generated by the microstructure. Here, we focus on the simulation of the resonance frequency of the CR as a function of the length  $l_{\text{cap}}$  of one capacitor finger (cf. Figure 4.1). For details on the simulations of coplanar microwave resonators see Appendix A.3.

For verification of the simulations, we designed a chip with eight CR's coupling to a transmission line. Each resonator has a different value of  $l_{\text{cap}}$ , varying from zero to  $l_{\text{cap,max}} = 736 \mu\text{m}$ . Two chips with this design have been fabricated and characterized at liquid helium temperatures down to  $T = 1.5 \text{ K}$ . The results were evaluated as shown in Section 4.2.1.

Figure 4.3(a) shows the simulated and the measured resonance frequency  $f_r$  plotted against  $l_{\text{cap}}$ . We observe that  $f_r$  tunes well with  $l_{\text{cap}}$ . Apart from a systematic offset of  $\approx 50 \text{ MHz}$ , the simulated resonance frequencies are in good agreement with the measured values. The overestimation in the simulation might be attributed to the fact, that the simulation does not include properties of superconductors. The relevant effects are the specific current distribution in the strip cross section

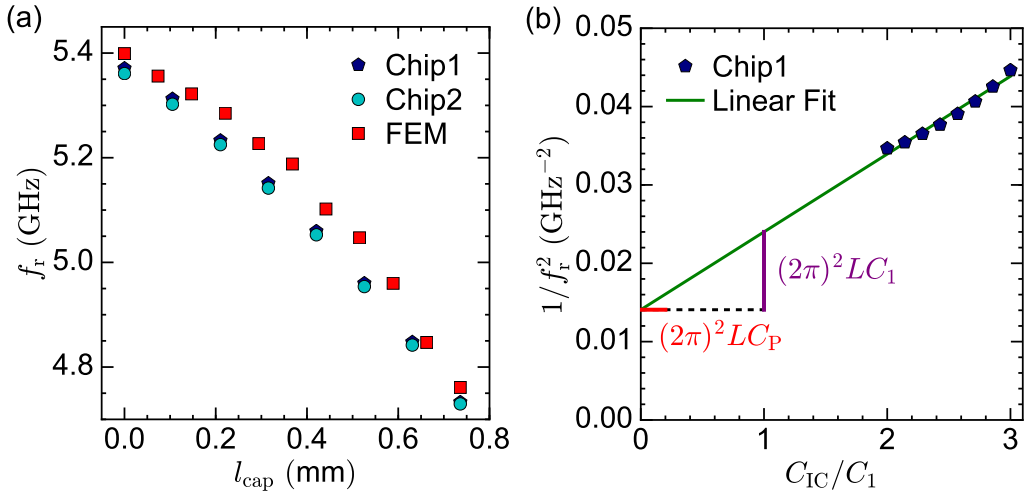


**Figure 4.3:** (a) Measured and simulated resonance frequency  $f_r$  plotted against the length  $l_{cap}$  of one capacitor finger, which here acts as a geometric tuning parameter. (b) Squared inverse resonance frequency as a function of the designed capacitance  $C_{IC}$  of the interdigital capacitor. The x-axis is normalized to the capacitance  $C_1$  between two fingers. The dependence of  $f_r^{-2}$  is linearly fitted. Due to Eq. (4.4), the offset of the fit line is related to the parasitic capacitance  $C_P$ , while its slope is related to  $C_1$ .

as well as the kinetic inductance (cf. Section 4.2.3.2), which both alter the total inductance, and thus can account for the offset in  $f_r$  between simulation and measurement.

Additionally, we use the measured dependence  $f_r(l_{cap})$  to extract information about the parasitic capacitance  $C_P$  of LER, which is distributed over the whole resonator [57]. Since the capacitance between two fingers is proportional to the finger length (see Eq. (A.9)), we can write the total capacitance of the interdigital capacitor as

$$C_{IC} = \left( 2 + \frac{l_{cap}}{l_{cap,max}} \right) C_1, \quad (4.3)$$

where  $l_{cap,max} = 736 \mu\text{m}$  is the maximal finger length and  $C_1$  is the capacitance between two capacitor fingers of length  $l_{cap,max}$ . Further, we have  $C = C_{IC} + C_P$  and rewrite Eq. (4.1) to

$$\frac{1}{f_r^2} = (2\pi)^2 L \left[ C_1 \left( 2 + \frac{l_{cap}}{l_{cap,max}} \right) + C_P \right]. \quad (4.4)$$

This function is fitted to the measured data set of  $f_r(l_{cap})$  as shown in Figure 4.3(b) and results in a large ratio of  $C_P/C_1 = 1.4$ . With the estimated capacitance  $C_{IC} = 61 \text{ fF}$  from above, we can estimate the parasitic capacitance to be

$$C_P^{(\text{CR})} = 1.4 C_1 = 1.4 \frac{C_{IC}}{2 + \frac{300 \mu\text{m}}{736 \mu\text{m}}} = 36 \text{ fF}. \quad (4.5)$$

We demonstrated that the parasitic capacitance represents a large part of the total capacitance. This motivates the investigation of a resonator design without an interdigital capacitor, which is presented in the next section.

#### 4.1.2 Meander Resonator

We present the meander resonator (MR) design, which is obtained from the CR by omitting the interdigital capacitor. The idea is to increase the inductance of the resonator while decreasing the capacitance at the same time in order to keep the resonance frequency around 5 GHz. For the realization of this resonator, we need to enlarge the total strip length of the resonator, which increases the inductance  $L$  (cf. Eq. (A.8)) as well as the resonator's in-plane dimensions, as illustrated in Figure 4.4. Except for the length of the meandering strip section, the characteristic geometric parameters are inherited from the capacitively shunted meander resonator (cf. Table 4.1).

We estimate the inductance of the meander resonator in analogy to the approach demonstrated for the CR. Considering the total length of the  $l^{(MR)} = 22.8$  mm and the 32 meandering strip sections with an effective length of  $680\text{ }\mu\text{m}$  each, we calculate  $L_{\text{self}}^{(MR)} = 43.9\text{ nH}$  and  $M^{(MR)} = 12.1\text{ nH}$ . Due to the meandering structure, the MR exhibits opposing current directions in neighbouring strip sections, which leads to a negative contribution of the mutual to the total inductance  $L^{(MR)} = L_{\text{self}}^{(MR)} - 2M^{(MR)} = 19.7\text{ nH}$ . We find a value that is enhanced by 45 % compared to the CR inductance.

It is difficult to estimate the capacitance of the meander resonator ab initio due to the various contributions, which are capacitance between neighboring strip sections, mutual capacitance with the CPW and the ground plane as well as contributions from stray capacitance  $C_{\text{stray}}$ . However, for a rough estimation we can use the result found for the parasitic capacitance  $C_{\text{p}}^{(\text{CR})} = 36\text{ fF}$  of the CR in the previous section (cf. Eq. (4.5)) and assume that  $C_{\text{p}}$  scales linearly with the total strip

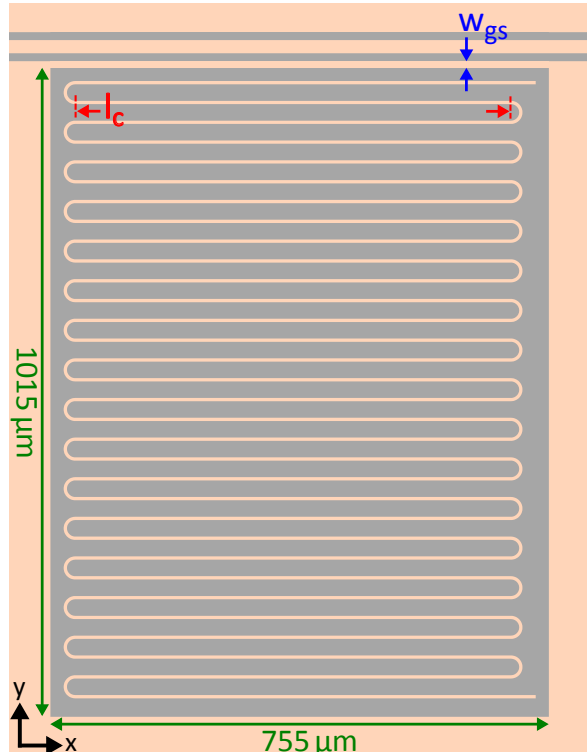


**Figure 4.4:** Layout of the meander resonator with a total strip length of 22.8 mm coupled to a CPW transmission line.

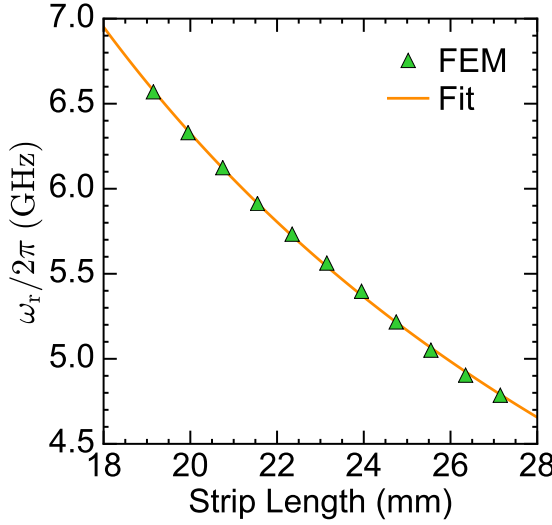


**Figure 4.5:** Simulated resonance frequency of the meander resonator as a function of the total strip length fitted using Eq. (4.7) with the two free parameters ( $L_l C_l$ ) and ( $L_l C_{\text{stray}}$ ). For a comparison between simulation and measurement see Section 4.2.2.1.

length. In this way, we find  $C^{(MR)} = 63 \text{ fF}$  and therefore  $f_r^{(MR)} = 4.5 \text{ GHz}$ , which is relatively close to  $f_r = 5.5 \text{ GHz}$ , resulting from FEM simulations of the meander resonator.

The absence of the interdigital capacitor requires to find a new geometric parameter for tuning the resonance frequency of meander resonators. We chose to stretch the resonator's dimension in the x-direction (cf. Figure 4.4) and thereby control its total strip length  $l^{(MR)}$ .

In Figure 4.5 we illustrate the dependence of the resonance frequency on  $l$  (short for  $l^{(MR)}$ ) simulated with the FEM.

We observe good tunability of  $f_r$  by varying the resonator strip length. However, the data set exhibits deviations from the expected relation

$$f_r = \frac{1}{2\pi\sqrt{L_l l \cdot C_l l}} \propto \frac{1}{l}, \quad (4.6)$$

where  $L_l$  and  $C_l$  are the inductance and capacitance per unit length, respectively. This is attributed to a contribution to the resonator capacitance, which is independent of the strip length, here denoted as the stray capacitance  $C_{\text{stray}}$ . With this assumption, we have  $C = C_l l + C_{\text{stray}}$  and therefore

$$f_r = \frac{1}{2\pi\sqrt{L_l C_l l^2 + L_l C_{\text{stray}} l}}. \quad (4.7)$$

Fitting this relation to the data in Figure 4.5 yields  $L_l C_l = 1.26 \cdot 10^{-18} \frac{\text{HF}}{\text{m}^2}$  and  $L_l C_{\text{stray}} = 6.4 \cdot 10^{-21} \frac{\text{HF}}{\text{m}}$ . This result gives access to the ratio of the stray to the total capacitance, which is determined to

$$\frac{C_{\text{stray}}}{C} = \frac{C_{\text{stray}}}{C_l l + C_{\text{stray}}} = \frac{1}{\frac{L_l C_l l}{L_l C_{\text{stray}}} + 1} = 18\%. \quad (4.8)$$

### 4.1.3 Spiral Resonator

In this section we present the spiral resonator (SR), which is a novel LER design based on the concept of a planar coil. In principle, this design is a further development of the MR, where we rearrange the two-dimensional topology of the resonator strip, such that neighbouring strip sections exhibit parallel current directions. We will show that this implies an improved homogeneity of the generated dynamic magnetic field  $B_1$  of the SR compared to resonators with meandering structures (see Section 4.1.5).

The layout of a SR coupled to a transmission line is depicted in Figure 4.6. Both strip ends of the resonator are topologically separated from each other, which permits the implementation of an interdigital capacitor. However, the latter is not essential for realizing resonance frequencies around 5 GHz, as shown for the meander resonator (cf. Section 4.1.2).

In order to maximize the generated  $B_1$ -field perpendicular to the  $x$ -axis, the layout is designed with two geometric features. First, the resonator's  $x$ -dimension is stretched, such that it represents a planar coil with in-plane asymmetry (see Figure 4.6). Second, the pitch between neighbouring strip sections is decreased for sections parallel to the  $x$ -axis ( $p_v = 25 \mu\text{m}$ ) compared to sections parallel to the  $y$ -axis ( $p_h = 30 \mu\text{m}$ ).

As performed for the previous designs, we estimate the inductance and capacitance of the SR. The resonator has a total strip length of  $l^{(\text{SR})} = 11.1 \text{ mm}$ , which yields a self-inductance of  $L_{\text{self}}^{(\text{SR})} = 19.7 \text{ nH}$  calculated with Eq. (A.8). Taking into account the pitches  $p_h$  and  $p_v$  as well as the effective length of neighbouring strip sections in  $x$ - and  $y$ -direction, we find  $M^{(\text{SR})} = 4.3 \text{ nH}$ . In contrast to resonators with meandering structures, the spiral resonator admits a parallel current direction in neighbouring strip sections. This implies that the mutual inductance of the SR contributes

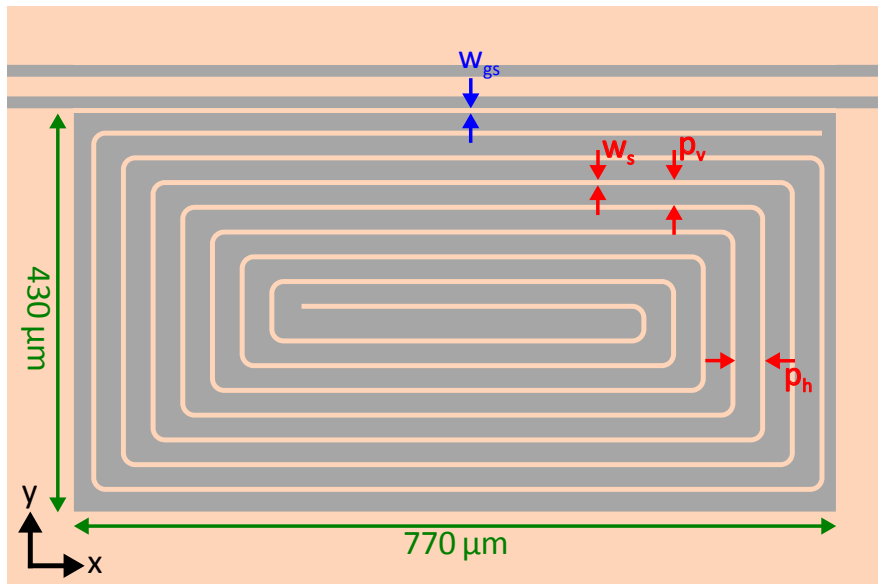


**Figure 4.6:** Layout of a spiral resonator with different pitches  $p_v = 25 \mu\text{m}$  and  $p_h = 30 \mu\text{m}$  between neighbouring strip sections depending on their in-plane orientation. The resonator microstrip has a width of  $w_s = 5 \mu\text{m}$  and total length of 11.1 mm.

positively to the total inductance, resulting in

$$L^{(\text{SR})} = L_{\text{self}}^{(\text{SR})} + 2M^{(\text{SR})} = 28.3 \text{ nH}. \quad (4.9)$$

Although the strip geometry and spacings are different, we assume the same parasitic capacitance per unit length as found for the CR, which yields  $C^{(\text{SR})} = 31 \text{ fF}$  and therefore  $f_{(\text{r})}^{(\text{SR})} = 5.4 \text{ GHz}$ . This agrees well with the measured value of 4.9 GHz.

In analogy to the meander resonator design, the resonance frequency of the SR is tuned by controlling the total strip length, which is varied via the resonator's x-dimension. For a comparison between the simulation and measurement results of the SR, see Figure 4.14 and corresponding discussion.

#### 4.1.4 Coupling to Transmission Line

In general, the coupling between a lumped element resonator and a transmission line can be inductive or capacitive, or a mixture of both. Capacitive coupling is realized by bringing one end of the resonator strip into the vicinity of the signal line, while inductive coupling is observed when the center of the strip is placed close to the signal line [59].

We discuss the coupling type of resonator designs CR, MR and SR based on the distribution of their surface current magnitude, simulated for resonant excitations and shown in Figure 4.7.

Theoretically, a capacitively shunted LER features a constant current magnitude along its inductive section [57]. Deviations from this idealization are due to parasitic capacitances between neighboring meander sections. This result is reproduced with FEM simulations for the CR layout (cf. Section 4.1.1) as shown in Figure 4.7, where we find a current magnitude decrease of roughly 30% from the center to the outer section of the meandering strip.

However, this outer section accounts for the coupling of the resonator to the signal line, which is mediated by a grounded strip (see Figure 4.1). Hence, we conclude a predominant inductive coupling of the CR to the transmission line.

The situation is different for meander and spiral resonators, where the coupling strip section represents at the same time one end of the resonator strip. Consequently, we expect a dominating capacitive coupling, since charge carriers cannot develop large current densities close to the resonator's loose ends, which agrees with the simulated surface current illustrated in Figure 4.7.

The external coupling rate  $\kappa_{\text{ext}}$  is a crucial tuning parameter for microwave resonators, since different ESR applications impose individual requirements on  $\kappa_{\text{ext}}$ .

In general, the coupling strength is governed by the coupling geometry, specifically by the capacitance  $C_c$  and the mutual inductance  $M_c$  between transmission line and resonator in case of capacitive and inductive coupling, respectively, following the relation  $Q_{\text{ext}} \propto C_c^{-2}, M_c^{-2}$  [52, 59]. However, the quantities  $C_c$  or  $M_c$  are difficult to determine for a given layout. Hence, we focus on FEM simulations of  $\kappa_{\text{ext}}$  and their agreement with measurement data. The influence of geometric

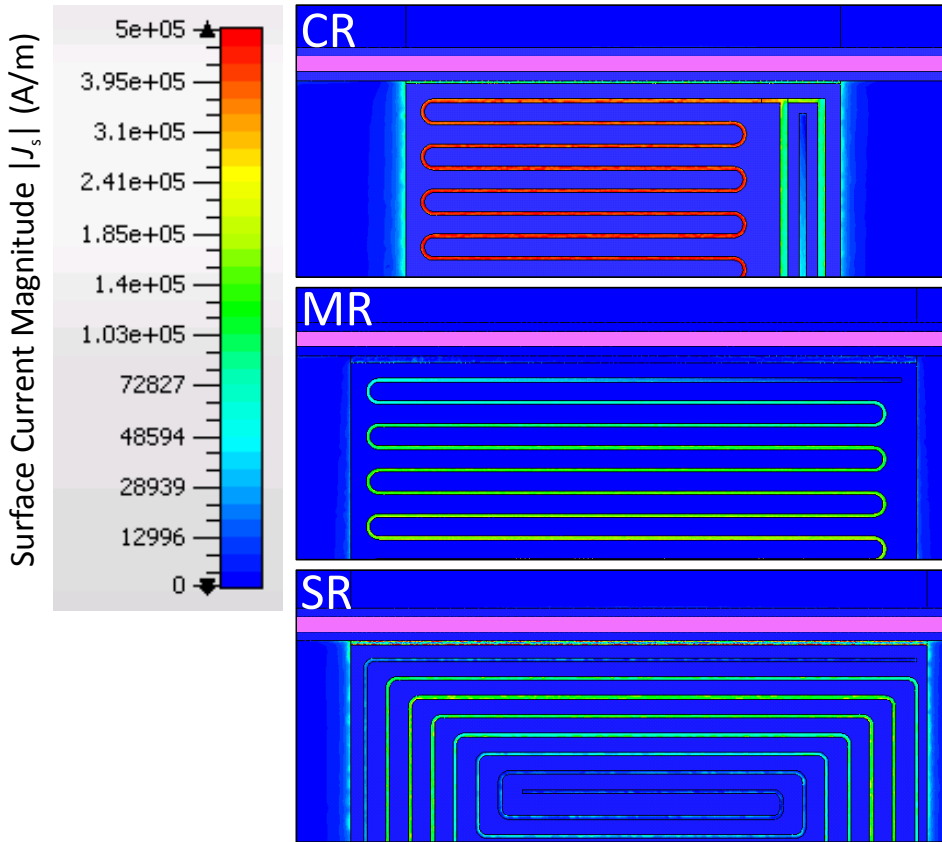


**Figure 4.7:** Simulated two-dimensional distribution of the surface current magnitude  $|J_s|$  of designs CR, MR and SR, resonantly driven via a transmission line (pink strip). The surface current magnitude is color coded on a logarithmic scale. Each resonator is excited with a similar photon number<sup>5</sup>.

parameters  $\kappa_{\text{ext}}$  is investigated.

We focus on the width of the grounded strip  $w_{\text{gs}}$  between the resonator and the CPW center conductor, the length of the coupling strip section  $l_c$  and the spacing  $s_c$  resonator and grounded strip (parameters illustrated in Figure 4.1). Remarkably, we find that the length of the coupling strip section  $l_c$  as well as its distance to the grounded strip  $s_c$  has little influence on the coupling rate  $\kappa_{\text{ext}}$ . However, our simulations show that varying  $w_{\text{gs}}$  allows to tune the coupling strength by several orders of magnitude.

In order to verify the FEM simulations, we designed a sample layout hosting eight capacitively shunted resonators coupled to one signal line. The resonators are tailored to distinct resonance frequencies and different values of  $w_{\text{gs}}$  ranging from  $5 \mu\text{m}$  to  $70 \mu\text{m}$ . We fabricated two superconducting chips with this layout and characterized their microwave transmission at liquid helium temperatures. From these transmission measurements, we extract the coupling rate  $\kappa_{\text{ext}}$  and plot it as a function of  $w_{\text{gs}}$  in Figure 4.8(a) along with the simulation results.

<sup>5</sup> The different surface current magnitudes between resonators are explained, considering their inductance. Due to a longer total strip length, the MR has an increased inductance. Additionally, the SR exhibits an enhanced inductance as a consequence of the positive contribution of the mutual inductance (cf. Section 4.1.3). Since all three resonators in Figure 4.7 host a similar excitation energy due to a similar photon number, the CR admits a higher current magnitude compensating for its lower inductance (cf. energy of LC circuit  $E_{\text{LC}} = \frac{1}{2}LI^2$ ).

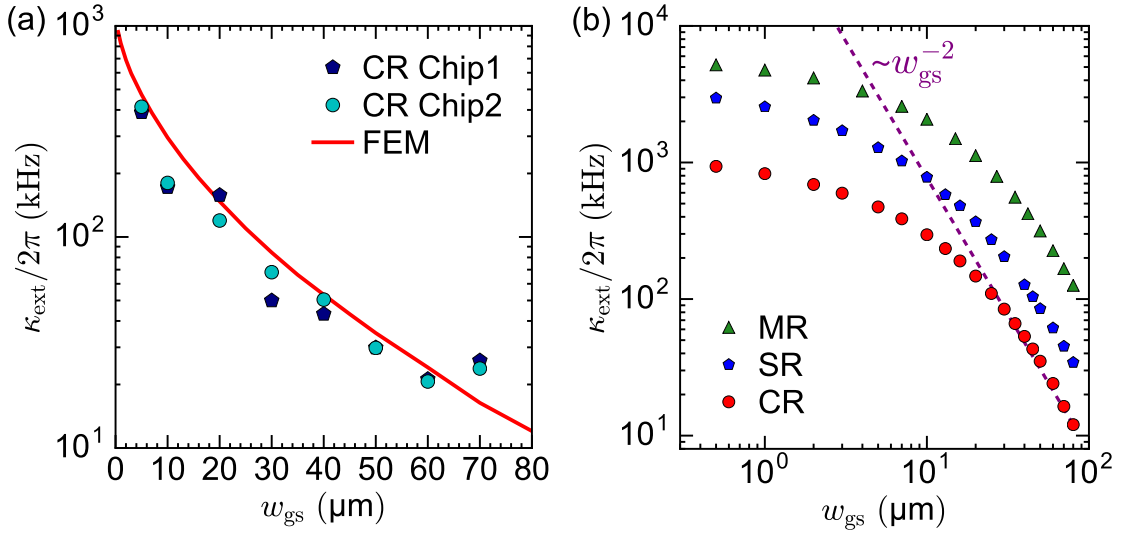


**Figure 4.8:** Tunability of external coupling strength measured and simulated for capacitively shunted meander resonators (a) and simulated for the three resonator designs (b). The coupling rate  $\kappa_{\text{ext}}/2\pi$  is plotted as a function of grounded strip width  $w_{\text{gs}}$ , which is the tuning parameter. Coupling rates were extracted from the transmission data using the DCM model (cf. Section 4.2.1).

We observe a very good agreement of measurement and simulation, taking into account that fabrication deviations typically have a significant influence on sample properties. Remarkably, for both chips the measured coupling strength of the resonator with  $w_{\text{gs}} = 70 \mu\text{m}$  is around twice the value expected from simulation. This is attributed to the vicinity of this resonator to a taper of the transmission line (located at either chip end), which leads to a significant enhancement of the coupling rate, compared to the small as-designed coupling rate.

Next, we demonstrate the tunability of  $\kappa_{\text{ext}}$  for the MR and SR designs, which are rather capacitively than inductively coupled. Again, the only effective tuning parameter is the grounded strip width  $w_{\text{gs}}$ . As illustrated in Figure 4.8(b), the variation of this parameter leads to tuning of the coupling rate in a similar fashion for all designs. We observe a lower coupling rate for capacitively shunted compared to spiral and meander resonators, for equal values of  $w_{\text{gs}}$ , which is attributed to the fundamentally different coupling type of the designs.

We also find a large enhancement of the MR coupling strength in comparison to spiral resonators, which might be due to capacitive coupling of the coupling strip section to neighbouring sections in combination with the different resonator topologies.

For all designs, we find that the coupling rate approximately scales as  $\kappa_{\text{ext}} \propto w_{\text{gs}}^{-2}$  (dashed purple line in Figure 4.8(b)) for large grounded strip widths  $w_{\text{gs}}$ .

Finally, tuning the coupling rate via the grounded strip width has an upper limit, given by the minimal width of superconducting strips due to the resolution in fabrication, which for the process used in this thesis is  $\lesssim 0.5 \mu\text{m}$ . One possibility to increase the coupling rate beyond that limit is to omit the grounded strip and thereby realize a direct coupling between the resonator and the signal line.

#### 4.1.5 Dynamic Magnetic Field

The dynamic magnetic field inhomogeneity of LERs with meandering structures is illustrated in Figure 4.9. We show the simulated dynamic field magnitude  $|H_1|$  of the CR in a resonant steady-state excitation, covering the meandering strips and the interdigital capacitor as well as two cutting planes, perpendicular to the x- and y-axis.

We observe high field magnitudes in the vicinity of the meandering strips. This is expected from Biot-Savart's law, which is here simplified to the magnetic field magnitude  $B_1(r)$  at distance  $d$  from an infinitely long straight wire in x-direction with current  $I$

$$\begin{aligned} B_1(d) &= \frac{\mu_0 I}{4\pi} \int_{-\infty}^{\infty} \frac{ds \times r}{r^3} = 2 \cdot \frac{\mu_0 I}{4\pi} \int_0^{\infty} \frac{|ds \times r|}{r^3} = \frac{\mu_0 I}{2\pi} \int_0^{\infty} dx \frac{d}{(x^2 + d^2)^{\frac{3}{2}}} \\ &= \frac{\mu_0 I}{2\pi} \left[ \frac{1}{d \sqrt{1 + \frac{d^2}{x^2}}} \right]_0^{\infty} = \frac{\mu_0 I}{2\pi d}. \end{aligned} \quad (4.10)$$

Additionally,  $|H_1|$  rapidly decays along the z-direction (note the logarithmic scale of  $|H_1|$ ) and vanishes on the length scale of the pitch  $p = 30 \mu\text{m}$ . The inset in Figure 4.9 illustrates  $H_1$  close to the chip surface, showing large inhomogeneities in the directions perpendicular to the resonator strip (y- and z-direction) for  $z < 10 \mu\text{m}$ .

The described magnetic field distribution is inherent to the arrangement of coplanar parallel strip sections with alternating current directions, resulting in a constructive and destructive magnetic field superposition in the near and far field, respectively.

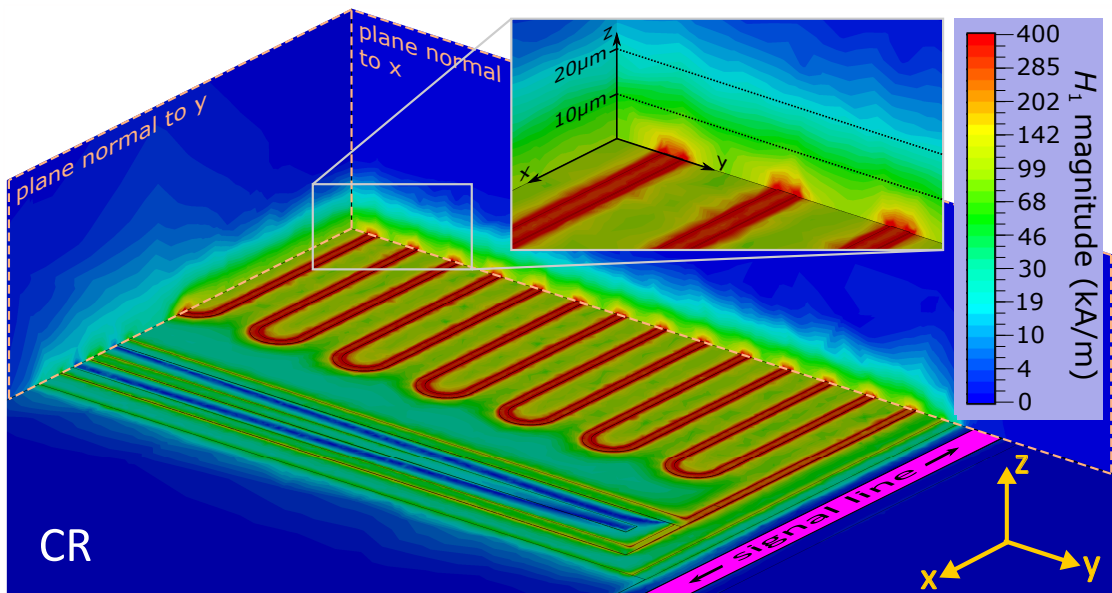


**Figure 4.9:** Image of the simulated magnetic field magnitude  $|H_1|$  of the capacitively shunted resonator excited at resonance frequency with a power of 0.5 W. The illustration of  $|H_1|$  is color coded with a logarithmic scale and covers part of the resonator layout as well as two cutting planes perpendicular to the x- and y-axis.

The exact opposite is observed for the magnetic field distribution of spiral resonators, illustrated in Figure 4.10. Due to the spiral topology, we find parallel current directions in neighboring strip sections, which leads to a constructive superposition of their contributions to  $|H_1|$  in the far field, whereas  $H_1$  partly vanishes in the near field (bluish areas in between neighboring strip sections). This gives rise to a flat descent of  $|H_1(z)|$ , resulting in a higher homogeneity of the dynamic magnetic field in the order and beyond the length scale of the pitch  $p_v = 25\mu\text{m}$  (cf. Figure 4.6). However, as a consequence of the coplanar coil concept, the mode volume of the SR exhibits domains, where the dynamic magnetic field is not perpendicular to the x-axis, which implies limitations to the filling factor for this resonator type (cf. Figure 5.3).

Next, we present a quantitative comparison of the  $B_1$ -field distributions of different resonator designs. For each resonator type, we extract from FEM simulations the dynamic magnetic field on a three-dimensional lattice with a voxel size of  $1\mu\text{m}^3$  within a cubic test volume in the half space  $z > 0$ . The footprint of the test volume is individual for each resonator design, coinciding with the resonator's footprint. To ensure comparability between designs, we rescale the extracted  $B_1$  distribution, taking into account the different number of photons during steady-state excitation of each resonator. To this end, we extract the simulated photon number  $n$  from each resonators' microwave transmission and rescale the magnitude of  $B_1$  to a constant photon number<sup>6</sup> of  $n = 2 \cdot 10^{13}$  for all designs via the relation  $B_1 \propto \sqrt{n}$ .

First, we use this framework to estimate the mode volumes  $V_m$  of resonator designs, here defined as the volume, which contains magnetic field magnitudes  $|B_1|$  greater than 5 % of the maximal

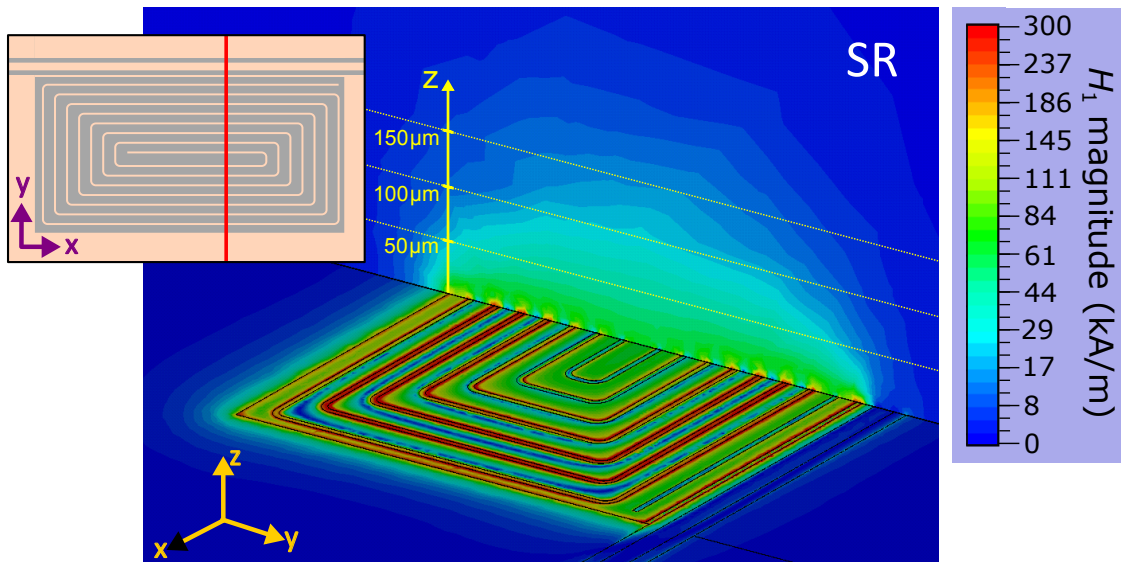


**Figure 4.10:** Image of the simulated magnetic field magnitude  $|H_1|$  of the spiral resonator, resonantly excited with a power of  $0.5\text{ W}$ . The illustration of  $|H_1|$  is color coded with a logarithmic scale and covers part of the resonator layout as well as a cutting plane perpendicular to the x-axis. The inset shows the layout of the SR indicating the in-plane position of the cutting plane (red line).

<sup>6</sup> This photon number roughly corresponds to the maximal critical microwave power of  $-6\text{ dBm}$  found for our LERs (cf. Section 4.2.5).

value  $|B_{1,\max}|$  of the distribution<sup>7</sup>. Based on this definition, we find  $V_m^{(\text{CR})} = 0.046 \text{ mm}^3$ ,  $V_m^{(\text{MR})} = 0.056 \text{ mm}^3$  and  $V_m^{(\text{SR})} = 0.220 \text{ mm}^3$ , which reflects the large spatial extent of the spiral resonator's  $B_1$ -field shown in Figure 4.10. Further, we consider for each resonator the ratio

$$R_{yz} = \sqrt{\frac{\sum_{\mathbf{r} \in V_m} (B_{1,y}^2(\mathbf{r}) + B_{1,z}^2(\mathbf{r}))}{\sum_{\mathbf{r} \in V_m} B_1^2(\mathbf{r})}}, \quad (4.11)$$

which is a measure for the orientation of  $B_1$  in the mode volume with respect to the  $yz$ -plane. Additionally,  $R_{yz}$  is proportional to the collective coupling rate  $g_{\text{eff}}$  of a paramagnetic spin system to the resonator (cf. Section 5.1.4). We find  $R_{yz}^{(\text{CR})} = 91.3\%$ ,  $R_{yz}^{(\text{MR})} = 99.0\%$  and  $R_{yz}^{(\text{SR})} = 72.8\%$ . For the CR,  $R_{yz}^{(\text{CR})}$  is reduced from 100% due to contributions of  $B_1$ -field vectors that are parallel to the  $x$ -axis, stemming from the interdigital capacitor. This is even more pronounced for the SR, which exhibits large domains with  $B_1(\mathbf{r}) \parallel \hat{x}$  as mentioned above.

In the following, we compare the statistical distribution of the  $yz$ -component  $B_{1,yz}$  of the dynamic magnetic field for different resonator designs. Figure 4.11(a) shows the spectral distribution of  $B_{1,yz}$  in arbitrary units plotted against  $B_{1,yz}$  for the three resonator designs considering a test volume defined by each resonator's footprint and  $0 \mu\text{m} < z < 35 \mu\text{m}$ . We observe a high spectral distribution of low fields for the CR and MR, which is attributed to the rapid decay of  $B_1(z)$ , when moving away from the resonator surface. In contrast, the spiral resonator shows a comparable

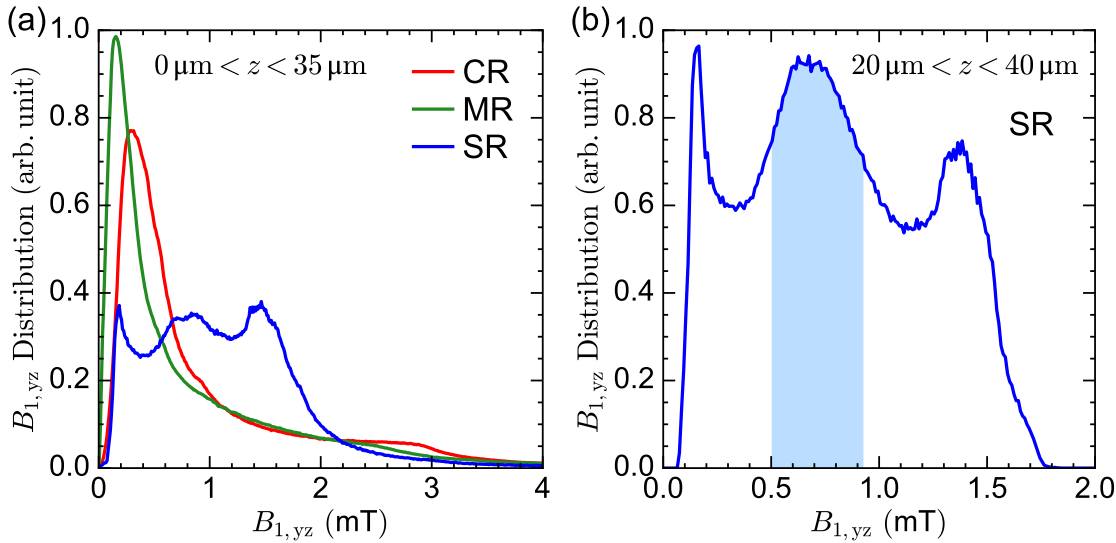


**Figure 4.11:** Comparison of simulated magnetic excitation field distribution for the CR, MR and SR. For both figures, we plot the spectral distribution of  $B_{1,yz}$  in arbitrary units as a function of  $B_{1,yz}$ . Each simulated  $B_1$  distribution is normalized to a typical critical photon number of  $n = 2 \cdot 10^{13}$  for comparability. The analysis is restricted to the  $yz$ -component of the dynamic magnetic field  $B_{1,yz} = \sqrt{B_{1,y}^2 + B_{1,z}^2}$ , which is relevant for the manipulation of spins in ESR experiments. The total test volumes are cuboids, which are individually defined by each resonator's footprint in combination with the condition  $0 \mu\text{m} < z < 35 \mu\text{m}$  (a) and  $20 \mu\text{m} < z < 40 \mu\text{m}$  (b).

<sup>7</sup> In practice, we interpret the 99th percentile as  $|B_{1,\max}|$  to circumvent numerical artifacts.

spectral density of  $B_{1,yz}$  values up to 1.6 mT.

To highlight the local  $B_1$  homogeneity of the SR, we consider its spectral  $B_1$  distribution in a test volume with  $20 \mu\text{m} < z < 40 \mu\text{m}$  in Figure 4.11(b). The high spectral diffusion for low values of  $B_{1,yz}$  stem from  $B_1$ -vectors parallel to the x-axis, which thus have a small  $yz$ -component. Dynamic field values exceeding 1.6 mT do not occur, since high values of the magnetic excitation field are typically observed close to the resonator surface (we excluded the volume given by  $z < 20 \mu\text{m}$  from this consideration). Finally, the improved  $B_1$  homogeneity is illustrated by the blue area, which marks values of  $B_{1,yz}$  in a 30 % interval centered around 0.72 mT. Comparing the SR with the CR and MR, we find that the  $B_1$  distribution of the SR is more favorable for pulsed ESR experiments, as a larger number of spins at different locations in the test volume ( $20 \mu\text{m} < z < 40 \mu\text{m}$ ) experience a similar  $B_1$ -field magnitude and thus perform a similar rotation on the Bloch sphere, which ultimately leads to an increased ESR signal.

Next, we perform a sanity check of the obtained  $B_1$  distribution. In general, the dynamic electric ( $E_1$ ) and magnetic ( $B_1$ ) fields of a resonator can be linked to the vacuum fluctuations corresponding to half a photon via [38]

$$\frac{\hbar\omega}{2} = \int_{V_m} \left( \frac{\epsilon_0 \epsilon_r}{2} E_1^2(\mathbf{r}) + \frac{1}{2\mu_0} B_1^2(\mathbf{r}) \right) d\mathbf{r} = 2 \int_{V_m} \frac{1}{2\mu_0} B_1^2(\mathbf{r}) d\mathbf{r} = \frac{V_m}{\mu_0} B_{1,RMS}^2, \quad (4.12)$$

with the root-mean-squared magnetic field  $B_{1,RMS}$ . By rescaling this result to the simulated photon number  $n = 2 \cdot 10^{13}$  we obtain

$$B_{1,RMS} = \sqrt{\frac{n\hbar\omega\mu_0}{2V_m}} = 0.94 \text{ mT}, \quad (4.13)$$

for the CR resonator, which is in the order of the root-mean-square  $B_{1,RMS}^{(\text{FEM})} = 1.8 \text{ mT}$ , extracted from the FEM simulation of the  $B_1$  distribution.

The criteria for the evaluation and comparison of different dynamic magnetic field distributions essentially depends on the experimental targets and circumstances of an ESR application. Therefore, we discuss in the following the performance of resonator designs in several scenarios of different ESR experiments, specifically considering the geometry and mounting of the ESR sample.

**Strong coupling to bulk sample** When aiming for a maximized coupling between the resonator and a bulk sample, one would choose a design with meandering structure. This choice is motivated by the orientation of the dynamic magnetic field of the CR and MR, which is mainly perpendicular to the static magnetic field direction, i.e., the magnetization direction of the spin ensemble. This property is quantified by  $R_{yz}$  (see Eq. (4.11)), which is directly proportional to the collective coupling rate  $g_{\text{eff}}$  and represents the only limitation to  $g_{\text{eff}}$  in this scenario.

**Strong coupling to thin sample** Next, we consider a thin ESR sample with a thickness in the range of tens of  $\mu\text{m}$ . In addition to the unfavorable orientation of the  $B_1$ -field of the SR, large parts of the resonator's mode volume are not coupled to the spin system due to the small sample size, which drastically reduces the collective coupling. In contrast, we observe a high concentration of the dynamic magnetic field of the CR and MR close to the resonator surface, or equivalently, the mode volume exhibits a small extent in z-direction (cf. Figure 4.9). Consequently, we expect no significant decrease of  $g_{\text{eff}}$  due to the sample thickness, assuming perfect mounting of the sample.

**Strong coupling with realistic sample mounting** As illustrated in Figure 4.16(a), a perfect mounting of the sample is difficult in reality, especially if the sample is very thin or has a rough surface. Mainly due to small dust particles on the chip surface, we assume a micrometer gap between the resonator and the mounted sample. In this realistic scenario, the spiral resonator outperforms other designs, due to its large mode volume, whereas resonators with meandering structures exhibit a strongly reduced collective coupling, as quantitatively shown in Figure 5.3.

**Maximize pulsed ESR sensitivity with a bulk sample** Increasing the sensitivity of pulsed ESR experiments, is a widely pursued target [22, 27]. We consider the ESR signal of a standard Hahn Echo pulse sequence with a bulk sample, assuming perfect mounting. In a simplified version, the detected echo signal is expressed by [45]

$$S = \int_{V_m} d\mathbf{r} A_0 |B_{1,yz}(\mathbf{r})| \underbrace{\sin(\theta_1) \sin^2\left(\frac{\theta_2}{2}\right)}_{=:\tilde{S}(\theta_1, \theta_2)}, \quad (4.14)$$

where  $1/A_0 = \int_{V_m} d\mathbf{r} |B_{1,yz}(\mathbf{r})|$  is a normalization factor and  $\theta_1$  and  $\theta_2$  denote the rotation angles in the Bloch sphere <sup>8</sup>.

In general, the rotation angle in the Bloch sphere  $\theta_1$  of a single spin at position  $\mathbf{r}$  depends on the pulse length  $t_1$  and  $|B_{1,yz}(\mathbf{r})|$ . In a simple picture, only spins from locations  $\mathbf{r}$ , where

$$\tilde{S} = \sin(\theta_1) \sin^2\left(\frac{\theta_2}{2}\right) \approx 1 \iff \theta_1(t_1, |B_{1,yz}(\mathbf{r})|) \approx \pi/2, \quad (4.15)$$

effectively contribute to the ESR signal  $S$ . This qualitatively defines a probe volume  $V_p$ , which exhibits small variations of  $|B_{1,yz}|$  (for instance 10 %), in order to fulfill Eq. (4.15). In this simple picture, we assume  $\tilde{S} = 1$  in the whole probe volume  $V_p$  and  $\tilde{S} = 0$  outside of  $V_p$ . With this, we can rewrite Eq. (4.14) to

$$S = \frac{\int_{V_p} d\mathbf{r} |B_{1,yz}(\mathbf{r})|}{\int_{V_m} d\mathbf{r} |B_{1,yz}(\mathbf{r})|}, \quad (4.16)$$

which represents a rough estimation of the ratio of the ESR signal to the total possible signal, given the case of a completely homogeneous magnetic excitation field  $B_1$ . On one hand, resonators with meandering structure exhibit a small probe volume  $V_p$  due to their  $B_1$  inhomogeneity, on the other hand they have a small mode volume. Hence, the integration volumes of both integrals

<sup>8</sup> This paragraph assumes knowledge of the basic principles of ESR, which can be acquired in [44, 60].

in Eq. (4.16) are small for the CR and the MR.

In contrast to that, the spiral resonator has a large volume  $V_p$ , where spins effectively contribute to the detected ESR signal, as a consequence of the flat  $B_1(z)$  descent for increasing distance  $z$  from the chip surface. However, at the same time this characteristic property of the spiral resonator leads to a large mode volume  $V_m$ . Considering Eq. (4.16), the simultaneous increase of  $V_p$  and  $V_m$  qualitatively cancels.

We conclude that increased homogeneity of the  $B_1$ -field does not automatically imply an enhanced ESR signal in pulsed experiments, as it is accompanied with a large volume of  $B_1$  field magnitudes, which do not effectively contribute to the signal.

**Weak coupling for coherent manipulation of spin system** The last ESR application we discuss is a weakly coupled spin system aiming for pulsed ESR experiments with coherent spin manipulation. Here, one would use a thin ESR sample coupled to a spiral resonator, ideally placed at a distance of around  $d_{\text{gap}} \approx 30 \mu\text{m}$  from the chip surface. In this region, the dynamic magnetic field is very homogeneous in the plane parallel to the chip surface and shows a weak dependence  $B_{1,yz}(z)$ , allowing for a coherent manipulation of the whole paramagnetic spin ensemble. In contrast, the highly inhomogeneous  $B_1$  distribution of the CR and MR lead to an increased dephasing of the magnetization during pulses in ESR experiments.

## 4.2 Continuous Wave Pre-characterization

Continuous wave (CW) experiments allow to characterize the microwave transmission of resonators coupled to a transmission line. Analyzing the transmission data with the framework introduced in Section 2.1.2, yields the resonance frequency as well as the internal and external Q-factors of a resonator, which are the key quantities for CW ESR spectroscopy covered in Chapter 5.

In Section 4.2.1, we perform an exemplary pre-characterization of a resonance lineshape acquired with the continuous wave measurement setup (cf. Section 3.3.1). We present a sample layout hosting multiple resonator designs (cf. Sections 4.1.1 to 4.1.3) on one chip. Further, we perform transmission measurements while varying temperature, static magnetic field and microwave drive power. Increasing these quantities, results in a situation less favorable for superconducting circuits and generally leads to a resonance frequency shift, which in most cases is accompanied by a linewidth broadening due to increased internal losses [61, 62]. Our results yield operation limits for the microwave resonators and show that the robustness against demanding measurement conditions is different for our various resonator designs. In particular, we identify the resonator's ratio of kinetic to total inductance as one key parameter for increasing the operating range of microwave resonators.

### 4.2.1 Resonance Transmission Fit

In the following we present an exemplary fit of transmission data with the DCM model (cf. Section 2.1.6).

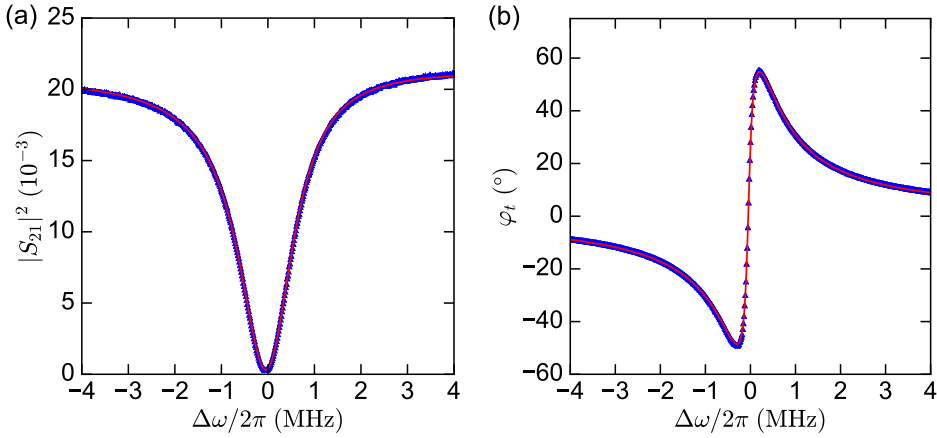


**Figure 4.12:** Exemplary fit (solid line) of transmission measurement data (blue triangles) using the DCM model (cf. Section 2.1.6). Power transmission  $|S_{21}|$  **(a)** and transmission phase  $\varphi_t$  **(b)** as a function of detuning  $\Delta\omega$ . Due to the frequency dependent electric length, the raw data of  $\varphi_t(\omega)$  have a baseline linear in  $\omega$ . We subtract an offset that is linear in frequency from the raw data, such that they coincide with simulated data at the two offresonant frequencies  $\omega_r/2\pi \pm 6 \text{ MHz}$ <sup>9</sup>.

Due to different attenuation and amplification of the microwave signal along its path between input and output port of the VNA, we observe a total setup power attenuation denoted as  $S_0^2$ . Hence, we modify Eq. (2.12) to

$$S_{21}(\Delta) = S_0 \left( 1 - \frac{\kappa_{\text{ext}}}{\kappa + i\Delta} \right), \quad (4.17)$$

where  $\Delta = \omega - \omega_r$  is the detuning from resonance frequency  $\omega_r/2\pi$ . Note that within the framework of DCM,  $\kappa_{\text{ext}} = |\kappa_{\text{ext}}| e^{i\varphi_r}$  accounts for an asymmetric lineshape arising from small induction changes of the coplanar waveguide transmission line near the resonator [59].

For fitting experimental or simulation data  $S_{21}(\omega)$ , it is sufficient to consider the real valued magnitude  $|S_{21}(\omega)|$  and ignore the phase information  $\varphi_t(\omega)$  (cf. Eq. (2.13)).

Figure 4.12(a) shows transmission data of the CR and the corresponding fit curve found with the above described framework. The measurement was performed with a sample power of  $-50 \text{ dBm}$  at zero static magnetic field  $B_0$  and  $T = 1.5 \text{ K}$ , which is well below the critical temperature of the bulk superconducting niobium ( $T_c = 9.2 \text{ K}$ ). Note that the critical temperature of our niobium thin films with  $d = 150 \text{ nm}$  thickness is expected to be less than  $0.1 \text{ K}$  reduced compared to the bulk value [63].

Our model provides a very good fit of the asymmetric lineshape. The fit parameters are shown

Parameter	$\omega_r/2\pi$ (GHz)	$2\kappa/2\pi$ (MHz)	$Q$	$Q_{\text{ext}}$	$Q_{\text{int}}$	$\varphi_r$ (°)	$S_0$ (dB)
Fit value	5.301	1.436	3692	4192	30978	-3.9	-38.6

**Table 4.2:** Summary of the DCM model parameters determined in the exemplary transmission fit in Figure 4.12.

<sup>9</sup> In principle, after subtracting the linear background from the phase  $\varphi_t$ , one finds a finite offset between the values of  $\varphi_t(\omega)$  for  $\omega \ll \omega_r$  and  $\omega \gg \omega_r$ , which is in analogy to the real part  $\epsilon'(\omega)$  of the complex dielectric function  $\epsilon = \epsilon' + i\epsilon''$  in the Lorentz model for dielectrics [64].

in Table 4.2. Using these parameters, we calculate the transmission phase shift  $\varphi_r(\omega)$  with Eq. (4.17) and find a very good agreement to the experimentally acquired  $\varphi_r(\omega)$  data in Figure 4.12(b).

### 4.2.2 Sample Pre-characterization

We present a sample layout with multiple microwave resonators and their designed parameters. Additionally, we pre-characterize the resonators before and after mounting an ESR sample on the chip and discuss the non-trivial assignment of resonance dips to resonator types.

#### 4.2.2.1 Sample Layout and Pre-characterization of Bare Chip

In order to overcome deviations in fabrication and ESR sample mounting between single chips, we assemble a chip layout, shown in Figure 4.13, containing multiple resonator designs (cf. Section 4.1) coupled to one transmission line. This allows the comparison of the general properties of resonator designs and their performance in various ESR applications.

All resonators are tailored to distinct resonance frequencies  $\omega_r/2\pi$  between 4.8 GHz and 5.8 GHz via slight tuning of their geometry. The external coupling rates are designed to span one order of magnitude for each resonator type, addressing the needs of different ESR applications (cf. Section 4.1.4). The sample hosts four resonators of each design.

Moreover, the layout contains two additional CR with a decreased (CR0, 3.7 GHz) and increased (CR5, 6.7 GHz) resonance frequency compared to the other resonators. These resonators are reserved for calibration of the static magnetic field  $B_0$  using the spin marker DPPH and will later on not be covered by the phosphorus doped silicon (Si:P) ESR sample (cf. Section 3.2).

Using the fabrication process described in Section 3.1, we microstructured this layout into an aluminum coated niobium layer deposited on a Silicon substrate. All measurements presented in the remainder of this thesis are performed on this sample.

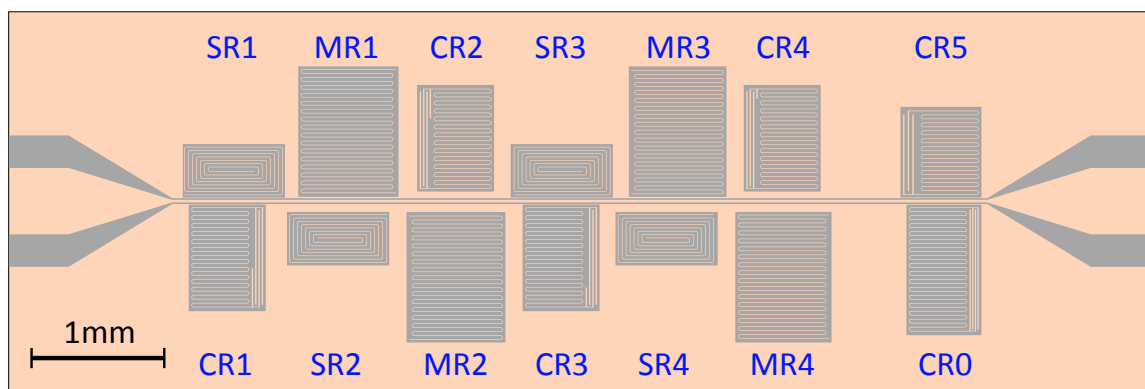


**Figure 4.13:** Region of interest of chip layout ( $6 \times 10 \text{ mm}^2$ ) covering 14 resonators coupled to a transmission line. The chip contains four versions of each resonator design (SR1-4, CR1-4, MR1-4) tailored at distinct resonance frequencies and various external coupling strengths and additional two CR for magnetic field calibration (CR0, CR5). Substrate and superconductor are illustrated in grey and light orange color, respectively.

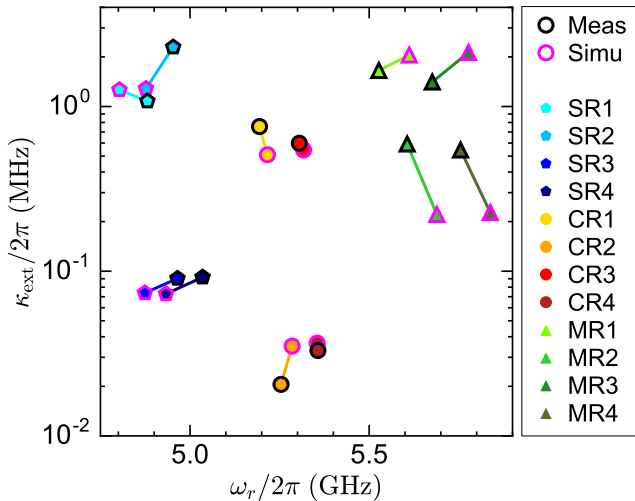


**Figure 4.14:** Measured and simulated resonator parameters of the multiple design sample.

The external coupling rate  $\kappa_{\text{ext}}/2\pi$  is plotted as a function of resonance frequency  $\omega_r/2\pi$ . Measured (black marker edge) and simulated data points (magenta marker edge) of same resonators are connected with a straight line for visualization.

In the following, we compare the tailored parameters of each resonator to the data acquired in CW measurements of the bare chip.

The microwave transmission of each resonator was simulated with an FEM solver and measured with the CW setup at  $T = 1.5\text{ K}$  and zero magnetic field. Both data sets were evaluated with the DCM model (cf. Section 4.2.1). The results are illustrated in Figure 4.14, where the external coupling rate  $\kappa_{\text{ext}}/2\pi$  is plotted as a function of resonance frequency  $\omega_r/2\pi$  for each resonator. We observe a good agreement of simulation and measurement. In the simulation, the resonance frequencies of spiral resonators (SR1-SR4) are systematically underestimated, whereas they are overestimated for meander resonators (MR1-MR4). Particularly, the resonance frequencies are well-separated from each other, which in principle allows the use of all resonators for ESR experiments. Except for the resonators MR2 and MR4, the coupling rates  $\kappa_{\text{ext}}$  exhibit a maximal deviation of factor 1.5 between measurement and simulation, which is small compared to their variation in the target design (one order of magnitude).

#### 4.2.2.2 Pre-characterization of Chip with Mounted ESR Sample

Next, we consider the microwave transmission of the sample, after mounting a phosphorus doped silicon single crystal as shown in Figure 3.2(b), which fully covers all resonators except CR0 and CR5.

Figure 4.15 shows the microwave transmission as a function of frequency of both, the sample with mounted Si:P crystal and the bare chip. Note that a different configuration of microwave attenuators and amplifiers was used for both measurements, explaining the different shapes of the offresonant transmissions (black lines).

After mounting the ESR sample, the set of resonance dips is shifted towards lower frequencies spanning 3.65 GHz to 4.75 GHz. The shift is individual for each resonator and assumes values up

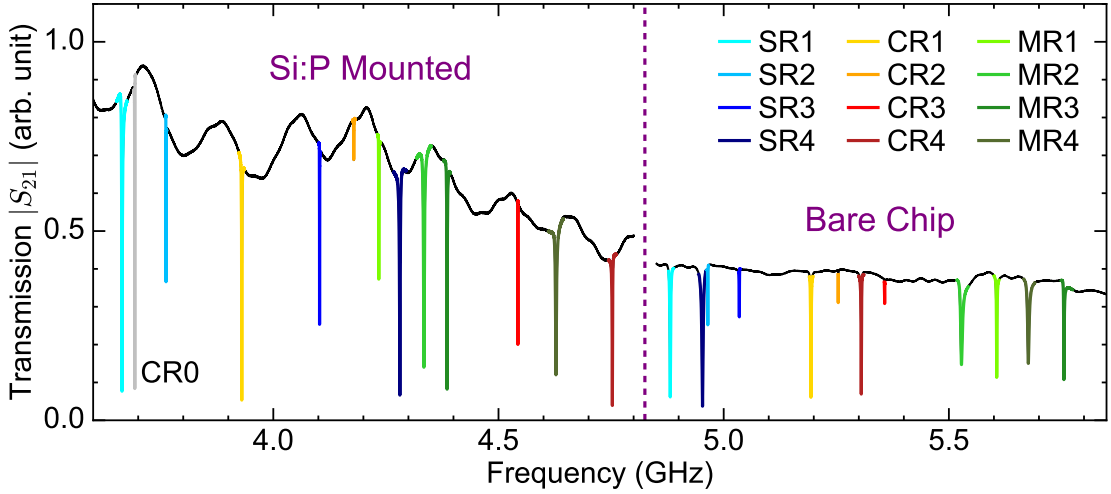


**Figure 4.15:** Transmission  $|S_{21}|$  of the sample with mounted Si:P crystal and the bare sample acquired with different CW setups at  $T = 1.5\text{ K}$ . Offresonant transmission of both measurements (black lines) is calibrated to match at  $\omega/2\pi = 4.8\text{ GHz}$ . The transmission is plotted in arbitrary units as a function of frequency. The resonance frequency of CR0 (silver line) remains unchanged upon mounting the Si:P crystal.

to 1.25 GHz. By mounting the Si:P crystal, the effective relative permittivity  $\epsilon_{\text{eff}}$  is increased, since vacuum ( $\epsilon_{\text{vac}} = 1$ ) is replaced by phosphorus doped silicon ( $\epsilon_{\text{Si:P}} \approx \epsilon_{\text{Si}} = 11.7$  [65]) as illustrated in Figure 4.16(a). Consequently, the resonators capacitance  $C \propto \epsilon_{\text{eff}}$  is increased, which in turn reduces the resonance frequency (cf. Eq. (4.1))

$$f_r \propto \frac{1}{\sqrt{\epsilon_{\text{eff}}}}. \quad (4.18)$$

In absence of the Si:P crystal, the effective permittivity is  $\epsilon_{\text{eff}}^{(\text{bare})} = (\epsilon_{\text{vac}} + \epsilon_{\text{Si}})/2 = 6.35$ , whereas it can be enhanced up to  $\epsilon_{\text{eff}}^{(\text{Si:P})} = (\epsilon_{\text{Si}} + \epsilon_{\text{Si:P}})/2 = 11.7$ , after mounting the Si:P crystal. Using Eq. (4.18) we find the maximal frequency shift

$$\frac{\Delta f_r^{(\text{Si:P})}}{f_r^{(\text{bare})}} = \frac{f_r^{(\text{Si:P})} - f_r^{(\text{bare})}}{f_r^{(\text{bare})}} = \sqrt{\frac{\epsilon_{\text{eff}}^{(\text{bare})}}{\epsilon_{\text{eff}}^{(\text{Si:P})}}} - 1 = -26.3\%, \quad (4.19)$$

which corresponds to  $|\Delta f_r^{(\text{Si:P})}| = 1.3\text{ GHz}$  for  $f_r^{(\text{bare})} = 4.9\text{ GHz}$ .

However, due to imperfect mounting of the Si:P crystal on the chip surface, we assume a micrometer gap between the chip surface and the ESR sample, which in principle can be individual for each resonator. Hence, the dielectric environment of resonators changes individually, explaining the different frequency shifts shown in Figure 4.15. We explore the dependence  $\Delta f_r^{(\text{Si:P})}(d_{\text{gap}})$  with FEM simulations by varying the gap  $d_{\text{gap}}$  between chip surface and ESR sample. The simulated resonance frequency  $\Delta f_r^{(\text{Si:P})}/f_r^{(\text{bare})}$  as a function of  $d_{\text{gap}}$  is plotted for the resonators SR1, CR1 and MR1 in Figure 4.16(b).

We observe a perfect agreement between theoretical prediction (cf. Eq. (4.19)) and simulation for the case of zero gap  $d_{\text{gap}} = 0$ . For  $d_{\text{gap}} > 0$ , the CR exhibit a smaller relative frequency change,

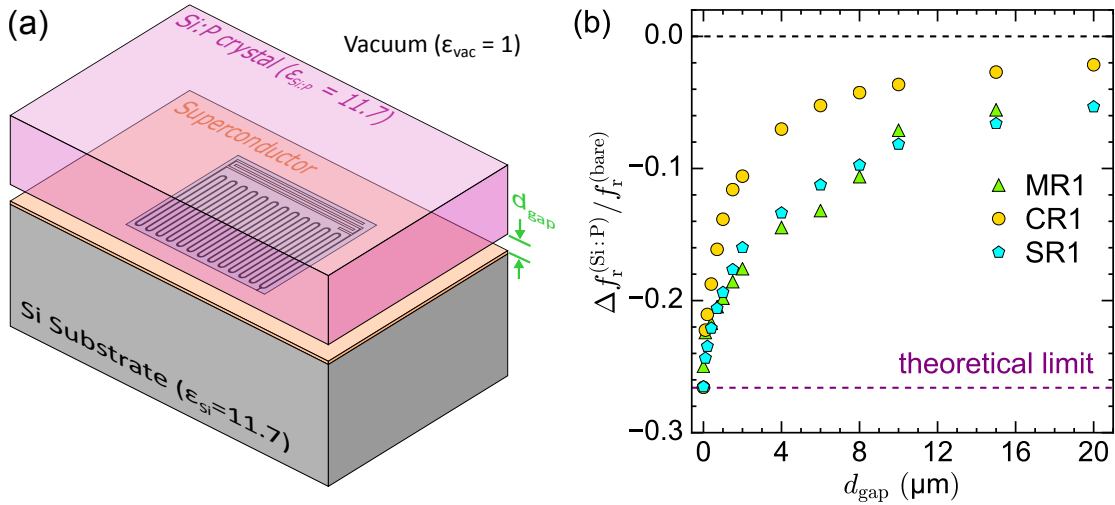


**Figure 4.16:** (a) Illustration of finite gap  $d_{\text{gap}}$  between chip surface and mounted Si:P crystal. (b) Simulated frequency shift as a function of the gap width  $d_{\text{gap}}$  for different resonator designs. The dashed purple line indicates the theoretical limit of the frequency shift given by Eq. (4.19).

i.e., the enhancement of the resonator capacitance is smaller than for other designs. We attribute this to the different geometric length scales of the resonators capacitive structures. While  $C^{(\text{CR})}$  is governed by the interdigital capacitor with a finger spacing of  $s_{\text{cap}} = 15 \mu\text{m}$ , the capacitance of meander and spiral resonators is formed between neighbouring strip sections, which are separated by a spacing of  $25 \mu\text{m}$ . Hence, the electric fields of the CR are more confined compared to other designs. Therefore, the resonance frequency of the CR is less sensitive to dielectric changes at a distance  $d_{\text{gap}} > 0$  from the chip surface.

#### 4.2.2.3 Resonator Assignment

We explain our procedure to assign the resonance dips, which are observed after mounting the Si:P crystal on the chip surface, to the different resonator designs. This allows for a comparison of designs in ESR applications. We use the following arguments in chronological order:

1. The resonance frequencies  $f_r$  of CR0 and CR5 remain unchanged.
2. The temperature dependence of  $f_r(T)$ , investigated in Section 4.2.3, clearly distinguishes spiral resonators from the other resonator designs.
3. We use the values of the external coupling rate  $\kappa_{\text{ext}}$  to assign resonators with either very high or very low coupling strength.
4. According to Eq. (4.19), the maximal frequency shift of a resonator is at most 26.3 % of its original resonance frequency.
5. We distinguish capacitively shunted and meander resonators by their slightly different dependence of resonance frequency on the static magnetic field, which is examined in Section 4.2.4.

The assignment of CR0 and CR5 is trivial, since they are not affected by the mounting of the Si:P crystal. We identify the spiral resonators (SR1-SR4) due to their weaker dependence of resonance frequency on temperature (see Figure 4.17). Next, we find CR2 and CR3 due to their very high external coupling rate  $\kappa_{\text{ext}}$  as well as MR2 and MR4 due to a very low  $\kappa_{\text{ext}}$ . We assign CR1 to the lowest remaining frequency as a consequence of the limit on relative frequency shift.

At this point, one CR and two MR are yet to be assigned. For this purpose, we consider the resonant frequency as a function of the static magnetic field, depicted in Figure 4.19(a). We observe a clustering of non-spiral resonators into two groups for high values of  $B_0$ . As suggested by the resonators assigned up to now, the two clusters separate capacitively shunted resonators from meander resonators, which can be attributed to their different geometry. With this result, we assign the remaining resonators (CR4, MR1, MR3).

#### 4.2.3 Temperature

In this section, we examine the temperature dependence of the resonance frequency and the internal loss rate. We develop a model for the observed data based on the kinetic inductance of the superconductor.

##### 4.2.3.1 Experimental Results

Figure 4.17(a) shows the relative frequency shift as a function of temperature.

For all resonators,  $f_r$  decreases with increased temperature. We observe two distinct clusters, one comprising capacitively shunted resonators (CR) and meander resonators (MR), the other one consisting of spiral resonators (SR). Both clusters are fitted (purple line in Figure 4.17(a)) with the model introduced in Section 4.2.3.2.

Additionally, we calculate the temperature derivative  $df_r(T)/dT$ , depicted in Figure 4.17(b).

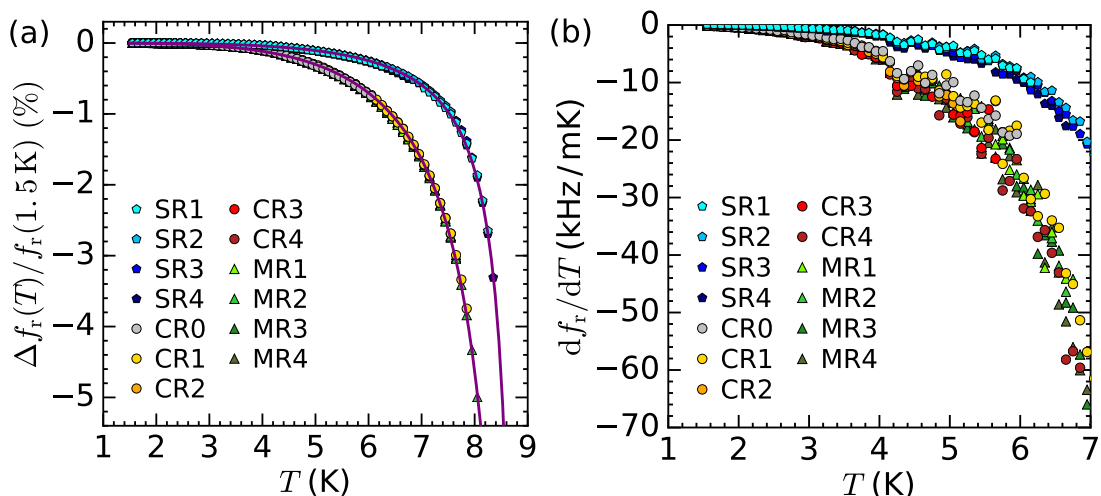


**Figure 4.17:** Relative resonance frequency shift ( $f_r(T) - f_r(1.5 \text{ K})/f_r(1.5 \text{ K})$ ) (a) and temperature derivative  $df_r/dT$  of the resonance frequency (b) as a function of temperature. The data was extracted from transmission measurements which were performed at zero field with a sample power of  $-30 \text{ dBm}$ . Purple lines are fits to the data with Eq. (4.27).

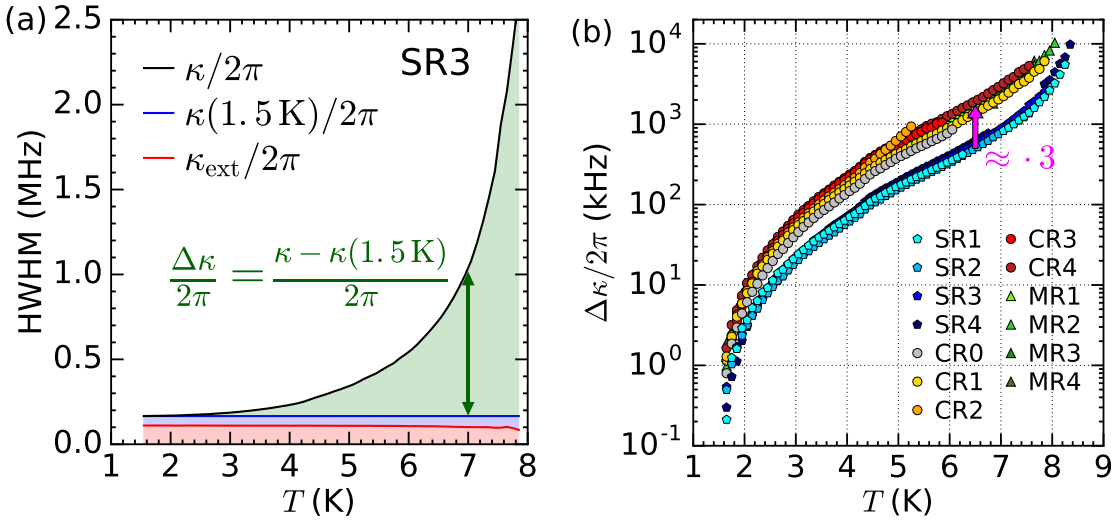


**Figure 4.18:** (a) Contributions to half linewidth (half width at half maximum in ordinary frequency units) of SR3 as a function of temperature. Red, blue and green areas illustrate  $\kappa_{\text{ext}}$ ,  $\kappa_{\text{int}}(1.5 \text{ K})$  and  $\Delta\kappa = \kappa - \kappa(1.5 \text{ K})$ , respectively. (b) Linewidth broadening  $\Delta\kappa$  for various resonators plotted logarithmically as a function of temperature. The two clusters are roughly separated by a factor of 3.

As expected, we again observe the two clusters of resonator designs. Spiral resonators exhibit a weaker temperature dependence  $|df_r(T)/dT|$  in comparison to the other designs, which is an advantage for ESR measurements at higher temperatures  $T \lesssim T_c$ , since setup temperature fluctuations translate into deviations of the resonance frequency.

Figure 4.18(a) illustrates the contributions to the resonator linewidth plotted against temperature. The external coupling rate  $\kappa_{\text{ext}}$  does not vary with temperature, since it only depends on geometry. We separate the total linewidth into the contributions

$$\kappa(T) = \kappa_{\text{ext}} + \kappa_{\text{int}}(1.5 \text{ K}) + \Delta\kappa(T), \quad (4.20)$$

where  $\Delta\kappa(T) = \kappa(T) - \kappa(1.5 \text{ K})$  is the pure temperature induced linewidth broadening. The latter is depicted in Figure 4.18(b) for all resonators. For temperatures between 3 K and 7 K, we find an exponential dependence of  $\Delta\kappa$  on temperature. Deviations from this behaviour below 3 K are attributed to the fact, that we subtracted  $\kappa(1.5 \text{ K})$  from  $\kappa$  instead of  $\kappa(0)$ , which results in a linear offset of data in Figure 4.18(b).

Additionally, resonators cluster in the same fashion as observed for the temperature dependence of the resonance frequency, which here means that spiral resonators exhibit a linewidth broadening  $\Delta\kappa$  reduced by a factor of 3 in comparison to the other designs.

#### 4.2.3.2 Effect of Kinetic Inductance

In order to explain the results presented in Figure 4.17(a), we develop an expression for the temperature dependence of the resonance frequency in the following.

The capacitance of a microwave resonator is assumed temperature independent, since it depends

only on the structure and the dielectric environment. However, the total inductance of a resonator consists of the temperature dependent kinetic inductance  $L_k(T)$  and the temperature independent geometric inductance  $L_{\text{geo}}$  [52]:

$$L(T) = L_{\text{geo}} + L_k(T). \quad (4.21)$$

It is useful to consider inductance per unit length, i.e.  $L_l(T) = L_{\text{geo},l} + L_{k,l}(T)$ , since both,  $L_{\text{geo}}$  and  $L_k$  scale linearly with the strip length  $l$ . While  $L_{\text{geo}}$  is related to the energy stored in the dynamic magnetic field, the kinetic induction arises from the kinetic energy of cooper pairs and is a function of the magnetic penetration depth  $\lambda_L$  [66], as shown hereafter.

We present two models for calculating the kinetic inductance of a superconducting strip with width  $w$  and thickness  $d$ , where  $w \gg d$ . The first model assumes a homogeneous current density distribution  $J_z^{(\text{hom})}$  over the cross section of the strip and yields [67]

$$L_{k,l}^{(\text{hom})}(T) = \frac{\mu_0 \lambda_L^2(T)}{wd}, \quad (4.22)$$

which is a good approximation for a thin strip.

The second model assumes an exponentially decaying penetration of current density  $J_z^{(\text{inhom})}$  from each surface to the inside of the superconductor, originating from London's second equation [65]. In Appendix A.4.1, we derive from the definition of the kinetic inductance

$$L_{k,l}^{(\text{inhom})}(T) = \frac{\mu_0}{4w} \frac{d + \lambda_L(T) \sinh\left(\frac{d}{\lambda_L(T)}\right)}{\cosh\left(\frac{d}{\lambda_L(T)}\right) - 1}. \quad (4.23)$$

However, we conclude that using the homogeneous model is sufficient for our strip geometry ( $d/\lambda_L(0) \approx 1.7$ ), since the models deviate by less than 10% for  $d \leq 3.2\lambda_L(0)$ . Note that  $\lambda_L(T)$  increases with temperature, i.e., we expect a large deviation for  $T \approx T_c$ .

Based on the observation in Figure 4.17(a) that the temperature induced change  $L_{k,l}(T) - L_{k,l}(0)$  of inductance is small compared to  $L_{\text{geo},l} + L_{k,l}(0)$ , we derive the following expression for temperatures  $T \ll T_c$  (for details see Appendix A.4.2)

$$\frac{f_r(T) - f_r(0)}{f_r(0)} \approx \frac{\alpha}{2} \left( 1 - \frac{L_{k,l}(T)}{L_{k,l}(0)} \right), \quad (4.24)$$

where

$$\alpha = \frac{L_{k,l}(0)}{L_{\text{geo},l} + L_{k,l}(0)} \quad (4.25)$$

is the ratio of kinetic and total inductance at zero temperature.

Now, the phenomenological Gorter-Casimir model [65]

$$\lambda_L(T) = \frac{\lambda_L(0)}{\sqrt{1 - \left(\frac{T}{T_c}\right)^4}}, \quad (4.26)$$

in combination with Eq. (4.22) and Eq. (4.24) finally yields a model for the temperature dependence of the resonance frequency

$$\frac{f_r(T) - f_r(0)}{f_r(0)} \approx \frac{\alpha}{2} \left( 1 - \frac{1}{1 - \left( \frac{T}{T_c} \right)^4} \right). \quad (4.27)$$

Particularly, the linear scaling of the relative frequency shift with  $\alpha$  has been observed for microwave kinetic inductance detectors (MKID) [57, 68].

All resonator layouts share the same strip cross section geometry and are patterned on the same superconducting material, i.e., from Eq. (4.22), we expect an equal kinetic inductance per unit length  $L_{k,l}(T)$  for all resonators. We obtain an expression for the geometric inductance per unit length by rewriting Eq. (4.25) to

$$L_{\text{geo},l} = \left( \frac{1}{\alpha} - 1 \right) L_{k,l}(0). \quad (4.28)$$

Assuming  $f_r(1.5 \text{ K}) \approx f_r(0)$ , we fit Eq. (4.27) to the data in Figure 4.17 with the free parameters  $T_c$  and  $\alpha$ . For the two data clusters, we find  $T_c^{(\text{SR})} = 8.90 \text{ K}$  and  $T_c^{(\text{CR,MR})} = 9.04 \text{ K}$ . Deviations of these values from each other and from the literature value  $T_c = 9.2 \text{ K}$  [65] are attributed to a systematic calibration error of the temperature probe of the cryogenic setup as well as to limitations of the model for temperatures close to  $T_c$ .

Additionally, fitting  $f_r(T)$  yields  $\alpha^{(\text{SR})} = 0.0192$  and  $\alpha^{(\text{CR,MR})} = 0.0586$ . Using Eq. (4.28), we calculate the ratio between geometric and kinetic inductance

$$L_{\text{geo},l}^{(\text{SR})} = 51.1 L_{k,l}(0), \quad (4.29)$$

$$L_{\text{geo},l}^{(\text{CR,MR})} = 16.1 L_{k,l}(0). \quad (4.30)$$

We obtain absolute values for the inductance using  $L_{k,l}(0) = 13.6 \text{ nH/m}$  calculated from Eq. (4.22) for a strip width of  $5 \mu\text{m}$ , a thickness of  $150 \text{ nm}$  and a the London penetration depth for niobium of around  $90 \text{ nm}$  [63, 65]. Considering the total strip lengths of the resonators SR1, CR1 and MR1, we obtain the total inductances

$$L^{(\text{SR1})} = 7.7 \text{ nH}, \quad L^{(\text{CR1})} = 3.0 \text{ nH} \text{ and } L^{(\text{MR1})} = 5.3 \text{ nH}. \quad (4.31)$$

For each resonator design, these values are approximately a factor of 4 smaller compared to the geometrically estimated values in Section 4.1.1 to 4.1.3. Since the offset is systematic for all designs, we attribute this to an error in the calculated kinetic inductance  $L_k(0)$  at zero temperature. This can be caused, for example, by omitting the dependence of the kinetic inductance on the current density [69].

Next, we briefly discuss the temperature induced linewidth broadening  $\Delta\kappa(T)$  (cf. Section 4.2.3). Thermal quasiparticles are the origin of increased internal losses at high temperatures [53], as they increase the surface resistance  $R_s$  of a superconductor [68]. The temperature induced

linewidth broadening  $\Delta\kappa(T)$  is generally described by [68]

$$\Delta\kappa(T) = \frac{\alpha\omega_r}{2} \frac{R_s(T) - R_s(0)}{X_s(T)}, \quad (4.32)$$

where  $X_s$  denotes the surface impedance of the superconductor. In particular,  $\Delta\kappa(T)$  scales linearly with the ratio of kinetic and total inductance  $\alpha$ . From the temperature dependence of the resonance frequency we extracted  $\alpha^{(\text{CR,MR})}/\alpha^{(\text{SR})} = 3.05$ . This ratio approximately corresponds to the offset between the two clusters of resonator designs in the logarithmic plot of Figure 4.18(b), which is in good agreement with the relation  $\Delta\kappa(T) \propto \alpha$ . (cf. Eq. (4.32)).

#### 4.2.4 Static Magnetic Field

We characterize the resonator parameters  $f_r$  and  $\kappa/2\pi$  as a function of the applied static magnetic field  $B_0$ , as shown in Figure 4.19.

In analogy to the temperature dependent frequency shift, the relative resonance frequency data (see Figure 4.19(a)) clearly cluster into spiral and other resonators. Additionally, we observe two subclusters of the latter, separating CR from MR for high static fields  $B_0$ . For all resonators we observe a nonlinear behaviour of  $f_r$  when increasing the static magnetic field towards  $B_0 \approx 330, which is interpreted as the first critical field  $B_{c1}$  of the type-II superconductor niobium, whereas after this threshold, the resonance frequency decreases linearly with  $B_0$ .$

Using in the static magnetic field dependence of the London penetration depth  $\lambda_L$  [65], we find an expression for the relative frequency shift

$$\frac{f_r(B_0) - f_r(0)}{f_r(0)} = \frac{\alpha}{2} \left( 1 - \frac{L_{k,l}(T, B_0)}{L_{k,l}(T, 0)} \right) = \frac{\alpha}{2} \left( 1 - \frac{1}{1 - \left( \frac{B_0}{B_{c1}} \right)^2} \right). \quad (4.33)$$

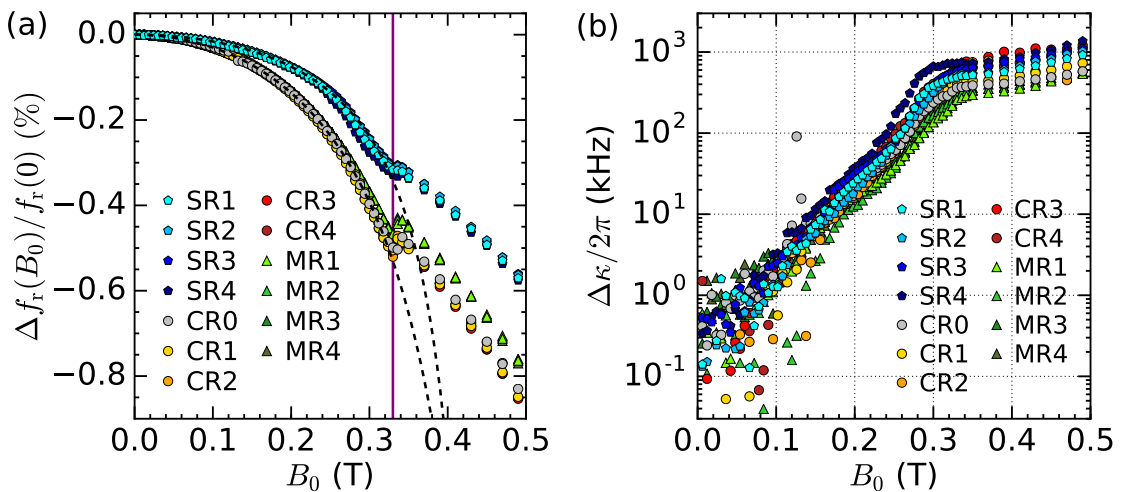


**Figure 4.19:** (a) Relative resonance frequency shift of multiple resonator designs as a function of the static magnetic field  $B_0$ . The two observed clusters of spiral and other resonators are fitted (black dashed lines) with Eq. (4.33). The purple vertical line separates the Meissner from the Shubnikov phase. (b) Dependence of the internal loss rate of resonators as a function of  $B_0$ . All measurements were performed at 1.5 K.

By fitting this model to the measurement data, we obtain the parameters  $B_{c1}^{(SR)} = 0.46$  T,  $B_{c1}^{(CR,MR)} = 0.52$  T,  $\alpha^{(SR)} = 0.0064$  and  $\alpha^{(CR,MR)} = 0.0156$ . Due to the large difference in the values of  $B_{c1}$ , the model is not considered consistent for this data set and does not yield conclusive results. Additionally, the values of  $\alpha$  differ from the ones found by analysing the temperature dependence of the resonance frequency. Further investigation is needed to explain this discrepancy. However, we observe that the spiral resonators are more robust towards magnetic field than the other designs. Figure 4.19(b) shows the resonator linewidth as a function of  $B_0$ . The loss rate increases exponentially with increasing static magnetic field and saturates beyond the critical field  $B_{c1}$ . We conclude, that in principle, the microwave LER can be operated in the Shubnikov phase of the superconductor, although they admit high internal loss rates there.

#### 4.2.5 Microwave Power

Microwave resonators exhibit a nonlinear behaviour for sample powers above a critical power  $P_c$ . The knowledge of  $P_c$  is essential for spectroscopy experiments due to its influence on the resonator's lineshape. We examine the power dependence of a capacitively shunted (CR3) and a spiral resonator (SR4) in Figure 4.20(a) and (b), respectively, where we plotted the power transmission as a function of frequency for a range of sample powers (see color code). The measurements are performed at 1.5 K and zero magnetic field.

For increasing sample power  $P_s$ , the resonance frequency of CR3 decreases, while the lineshape becomes asymmetric and finally exhibits a pronounced duffing behaviour with an infinite slope at a frequency lower than  $f_r$  [70].

Similarly, the resonance frequency of SR4 shifts towards lower values, upon increasing sample

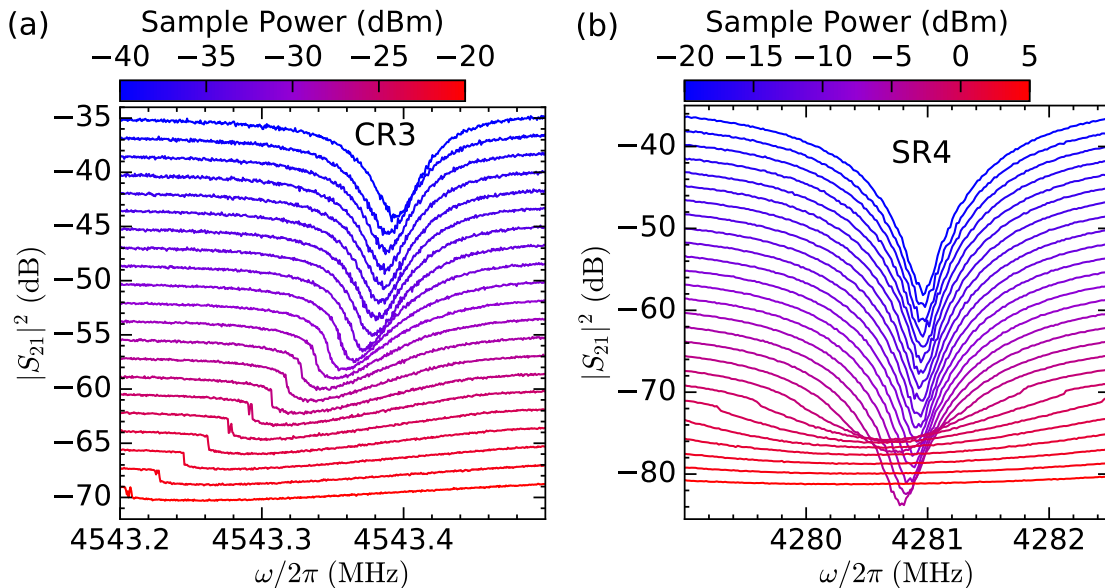


**Figure 4.20:** Duffing oscillator nonlinearity of resonators CR3 (a) and SR4 (b). The power transmission  $|S_{21}|^2$  is plotted as a function of frequency for an individual range of sample powers with steps of 1 dBm. Measurements were performed at 1.5 K and zero field. The plots were offset by 1.7 dB in the vertical direction for clarity.

power above  $-17$  dBm. However, the lineshape remains mostly unchanged for powers lower than  $-3$  dBm, where it shows a sudden and rapid broadening.

The described trends of the resonance frequency and the resonator quality are depicted in Figure 4.21, obtained by fitting the data in Figure 4.20 with the DCM model (cf. Section 4.2.1). Note that the DCM does not cover nonlinear effects.

Considering the resonance frequency shift, we find a critical power (vertical blue line) of  $P_c^{(f_r)} = -16$  dBm and  $P_c^{(f_r)} = -35$  dBm for CR3 and SR4, respectively (see caption of Figure 4.21 for the definition of  $P_c^{(f_r)}$ ). However, the resonator SR4 does not exhibit a change in  $Q_{\text{int}}$  for powers below  $-6$  dBm (vertical orange line). The region between  $-16$  dBm and  $-6$  dBm shows an onset of nonlinearity, nevertheless, we conclude that we can operate the resonator in this region without limitations.

Various effects of nonlinearity of superconducting Nb or NbN microwave resonators have been reported, ranging from resonance frequency shifts, linewidth broadening, asymmetric lineshapes, hysteresis and bifurcation to microwave intermodulation [62, 71–73]. Among the underlying mechanisms are duffing of the nonlinear harmonic oscillator, pair-breaking, local or global heating, effects due to material defects and many more [72]. In general, the resonance frequency depends on the kinetic inductance (cf. Section 4.2.3.2), whereas the internal quality factor is influenced by the sheet resistance  $R_s$  of the superconductor in the two fluid model [71].

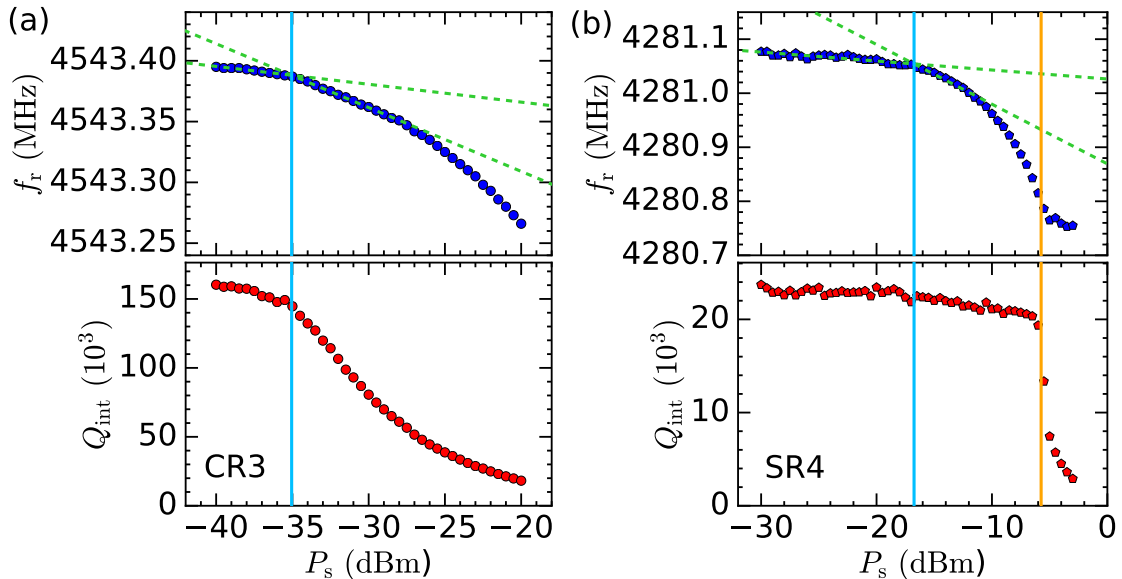


**Figure 4.21:** Critical microwave power extracted from the power dependence of the resonance frequency  $f_r$  and internal quality factor  $Q_{\text{int}}$  for resonators CR3 (a) and SR4 (b). Resonator parameters were extracted from transmission data shown in Figure 4.20. Vertical blue lines illustrate the critical power  $P_c^{(f_r)}$  found as intersection of the two dashed green lines, which are obtained by linear fits of  $f_r(P_s)$  in the linear regime of the resonator (lower power) and the region, where nonlinearities start to dominate (higher power). For SR4, the power dependence of  $Q_{\text{int}}$  indicates a higher critical power  $P_c^{(Q_{\text{int}})}$  (vertical orange line).

According to [69], the penetration depth  $\lambda_L$  also changes with the supercurrent density  $J$

$$\lambda_L(T, J) = \frac{\lambda_L(T, 0)}{\sqrt{1 - \left(\frac{J}{J_0(T)}\right)^2}}, \quad (4.34)$$

where  $J_0(T)$  is the effective pair-breaking current density. This relation in turn implies a power dependence of the kinetic inductance  $L_{k,l}$ , which explains the observed resonance frequency shift for high drive powers (cf. Eq. (4.24)) as well as the abrupt nonlinearity when the current density approaches  $J_0(T)$ .

### 4.3 Time Domain Pre-characterization

In this section, we present time domain pre-characterizations of microwave resonators and compare the results with a theoretical framework for describing non-equilibrium resonator dynamics. We briefly introduce the time domain setup and its basic measurement technique in Section 4.3.1. In Section 4.3.2, we verify the results of single pulse time domain measurements by comparing them with transmission data acquired in the CW setup. Further, we demonstrate that our model for an absorption microwave resonator coupled to a transmission line, presented in Section 2.1, is capable of reproducing the resonator response of single pulse experiments. We use the resonator parameters extracted from measurements with the CW setup to simulate the dynamic transmission of a signal line coupled to a resonator. In particular, the simulation results show an excellent agreement with data acquired with the time domain setup.

Generally, for pulsed electron spin resonance experiments, it is a decisive advantage to know the resonator dynamics, i.e. the time evolution of the resonator field  $a(t)$  (cf. Section 2.1.1), as the latter is proportional to the dynamic magnetic field  $B_1$  of the resonator (see Section ??). Ultimately, the framework presented in this section enables deeper understanding and prediction of the results of simple ESR experiments like Hahn echo or inversion recovery pulse sequences (see Section 6.2) as well as more demanding experiments involving adiabatic [45, 74, 75] or optimal control pulses [76].

#### 4.3.1 Time Domain Transmission Measurements

While continuous wave are mainly performed by a vector network analyzer, which has built-in functionality to simultaneously generate and detect microwave signals in a wide frequency range, here, we perform time domain transmission measurements using a pulsed excitation. The goal is to measure the time-resolved non-equilibrium transmission response to arbitrary waveforms.

We generate the in-phase ( $I$ ) and the quadrature component ( $Q$ ) of a waveform at an intermediate frequency  $f_{IF}$  in the MHz range (typically 42.5 MHz), which allows for full control over the signal magnitude and phase. Then, the microwave signal is converted to a frequency in the GHz range using an IQ mixer. After the signal is transmitted through the resonator chip, it is again downconverted to  $f_{IF}$ , this time using the low frequency side band of the IQ mixer. This yields

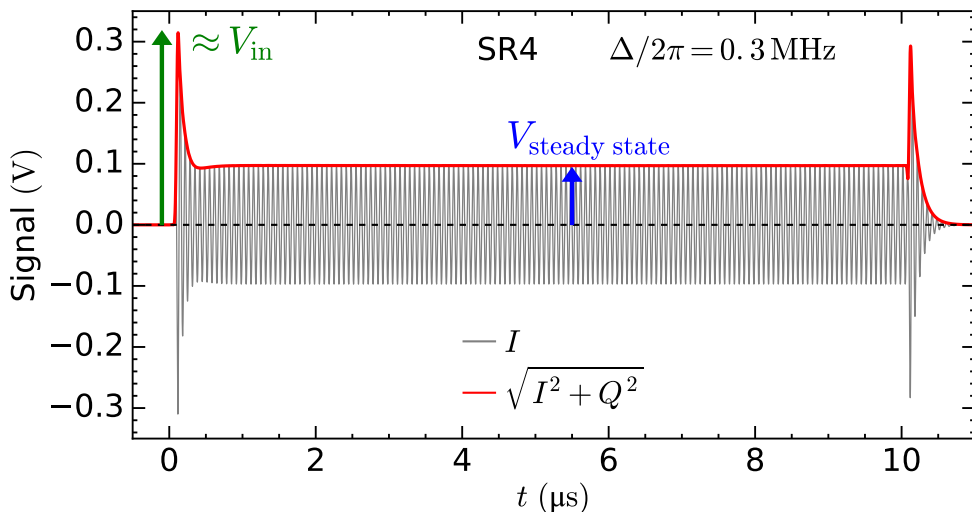


**Figure 4.22:** Time-resolved transmission of a single pulse experiment with rectangular pulse shape, pulse length  $t_p = 10\ \mu\text{s}$  and a power of  $-52\ \text{dBm}$ , performed at an effective drive frequency of  $\omega/2\pi = 4279.7\ \text{MHz}$ , which is  $0.3\ \text{MHz}$  detuned from the resonant frequency of SR4. The effective drive frequency  $\omega/2\pi$  results from a sum of the local oscillator frequency  $\omega_{\text{LO}}/2\pi = 4237.2\ \text{MHz}$  and the intermediate frequency  $\omega_{\text{IF}}/2\pi = 42.5\ \text{MHz}$ . We plot the in-phase component  $I$  of the intermediate frequency signal (here downconverted to  $15\ \text{MHz}$  for visualization) and its magnitude  $\sqrt{I^2 + Q^2}$  as a function of the time  $t$ . Blue and green arrows indicate the detected steady-state and input voltage<sup>10</sup>, respectively.

the quadratures  $I$  and  $Q$ , which are finally digitized with a high sampling rate and demodulated to a dc signal in software (cf. Section 3.4).

Figure 4.22 shows an exemplary response of the spiral resonator SR4 (cf. Section 4.2.2) to a rectangular excitation pulse with length  $t_p = 10\ \mu\text{s}$  and microwave sample power of  $-52\ \text{dBm}$ . The in-phase component  $I$  is plotted as a function of time  $t$ .

Due to the  $90^\circ$  phase shift between the quadratures  $I$  and  $Q$ , the magnitude of the intermediate frequency signal can be calculated to  $\sqrt{I^2 + Q^2}$  (cf. Section 3.4), which corresponds to the envelope (red curve) of  $I$  in Figure 4.22.

The transmission exhibits a ring up and ring down behaviour with characteristic sharp peaks in the transmitted signal at the beginning ( $t \approx 0\ \mu\text{s}$ ) and at the end ( $t \approx 10\ \mu\text{s}$ ) of the rectangular pulse, as expected from theory (for details see Section 2.1.3). These features stem from interference effects of the signal absorbed and emitted by the resonator and the transmitted microwaves of the signal line. Moreover, we observe a constant steady state signal magnitude  $V_{\text{steady state}}$  (blue arrow) between  $t \approx 1\ \mu\text{s}$  and the pulse end.

<sup>10</sup> As the signal is attenuated and amplified several times on its path through the MW circuitry, the magnitude of the detected signal does not correspond to the real signal magnitude at the sample, and therefore does not allow direct conclusions about the sample power.

### 4.3.2 Steady-state Transmission

We compare the steady-state transmission, which was on one hand extracted from time domain measurements, and on the other hand acquired with the continuous wave setup.

By considering  $V_{\text{steady state}}$  in relation to the input signal magnitude  $V_{\text{in}}$ , we can define the steady-state transmission obtained by time domain measurements as

$$S_{21}^{(\text{TD})} = \frac{V_{\text{steady state}}}{V_{\text{in}}} . \quad (4.35)$$

By sweeping the excitation frequency  $\omega/2\pi$  around the resonance frequency  $\omega_r/2\pi$  of a resonator, we obtain its transmission  $S_{21}^{(\text{TD})}(\omega)$  in the frequency domain.

Note that  $V_{\text{in}}$  roughly corresponds to the green arrow in Figure 4.22, however, a precise determination of the input voltage level is simply achieved with a single pulse measurement far detuned from  $\omega_r/2\pi$ .

Figure 4.23 shows the power transmission plotted against the detuning  $\Delta/2\pi$ , for the measurement sets acquired with the CW and TD setup, along with the corresponding lineshape fits (cf. Section 4.2.1).

The extracted quality factors are  $Q_{\text{ext}}^{(\text{CW})} = 1631 \pm 2$  ( $Q_{\text{ext}}^{(\text{TD})} = 1627 \pm 5$ ) and  $Q_{\text{int}}^{(\text{CW})} = 20500 \pm 700$  ( $Q_{\text{int}}^{(\text{TD})} = 19900 \pm 1400$ ) for the continuous wave (time domain) setup. The resonator parameters of both data sets are within their mutual fitting uncertainties, which is a general verification of the time domain setup.

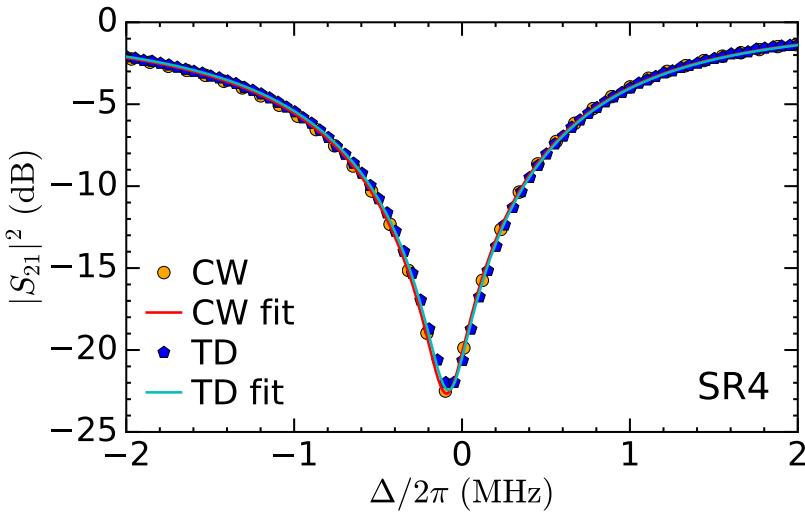


**Figure 4.23:** Comparison of microwave power transmission  $|S_{21}|^2$  as a function of detuning  $\Delta/2\pi = (\omega - \omega_r)/2\pi$  around the resonance frequency  $\omega_r/2\pi = 4779.42$  MHz of SR4, acquired with the continuous wave and the time domain setup at 1.6 K and a drive power around  $-50$  dBm. The time domain transmission data is extracted from  $10\mu\text{s}$  pulse experiments (as illustrated in Figure 4.22) following Eq. (4.35). We show fits based on the DCM model for both data sets (see text for extracted fitting parameters). Note that as a consequence of the asymmetric lineshape ( $\varphi_r = -4.0^\circ$ ), the frequency at minimal transmission does not coincide with the resonance frequency extracted by the DCM fit.

### 4.3.3 Resonator Dynamics

In the following, we briefly describe the framework for simulation of non-equilibrium resonator excitations.

First, we extract the resonator parameters  $\omega_r/2\pi$ ,  $\kappa$  and  $\kappa_{\text{ext}}$  from continuous wave measurements, where  $\kappa_{\text{ext}} = |\kappa_{\text{ext}}|e^{i\varphi_r}$  contains the asymmetry parameter  $\varphi_r$ . These quantities are sufficient to fully describe the excitation and relaxation behaviour of the specific resonator.

We simulate the resonator response to a given excitation pulse  $b_{\text{in}}(t)$ . Here,  $b_{\text{in}}(t)$  is the normalized dimensionless pulse shape, i.e., its magnitude  $|b_{\text{in}}(t)|$  assumes values between 0 and 1. The resonator dynamics are generally described by the dimensionless equation of motion

$$\dot{a}(t) = i\omega_r a(t) - \kappa a(t) + \sqrt{\kappa_{\text{ext}}} b_{\text{in}}(t), \quad (4.36)$$

which is discussed in Section 2.1.1 to 2.1.3. By considering Eq. (4.36) in the rotating frame, obtained by multiplication with the factor  $e^{-i\omega t}$ , where  $\omega$  is the drive frequency, we find a first order ordinary differential equation for the magnitudes  $|b_{\text{in}}(t)|$  and  $|a(t)|$ . With the boundary condition  $a(0) = 0$ , we solve the equation numerically, which yields the resonator field transient  $a(t)$  as a response to the input field  $b_{\text{in}}(t)$ . Next, we rescale the dimensionless quantities  $b_{\text{in}}(t)$  and  $\sqrt{\kappa_{\text{ext}}} a(t)$  with the detected input voltage  $V_{\text{in}}$ , to obtain comparability to the measured data. Then, Eq. (2.7) yields an expression for the transmitted signal magnitude

$$\sqrt{I^2 + Q^2} = V_{\text{in}} |b_{\text{in}}(t) - \sqrt{\kappa_{\text{ext}}} a(t)|. \quad (4.37)$$

We demonstrate this framework for rectangular and Gaussian shaped drive pulses, starting with the former.

Figure 4.24(a) shows the measured and simulated transmission of the resonator SR4 resonantly excited ( $\Delta/2\pi = 0$ ) by a rectangular pulse with a length of  $10\mu\text{s}$ . The time domain (simulation) data were calculated with the left-hand (right-hand) side of Eq. (4.37). We observe an excellent agreement between the measurement and the ab initio simulation.

For resonant excitations, the input and resonator field are in phase, when we neglect the influence of the lineshape asymmetry ( $\varphi_r \approx 0$ ). Thus we rewrite Eq. (4.37) for  $t < 10\mu\text{s}$  to (note that there we have  $|b_{\text{in}}(t)| > |\sqrt{\kappa_{\text{ext}}} a(t)|$ )

$$\sqrt{I^2 + Q^2} = V_{\text{in}} |b_{\text{in}}(t)| - V_{\text{in}} |\sqrt{\kappa_{\text{ext}}} a(t)|, \quad (4.38)$$

which has a simple consequence for the quantities plotted in Figure 4.24(a). Adding the transmission magnitude  $\sqrt{I^2 + Q^2}$  (red curve) to  $V_{\text{in}} |\sqrt{\kappa_{\text{ext}}} a(t)|$  (blue curve) results in the drive magnitude  $V_{\text{in}} |b_{\text{in}}(t)|$  (green curve).

Next, we consider an excitation pulse with Gaussian shape and a nominal length of  $t_p = 0.3\mu\text{s}$ , which corresponds to the full width at half maximum of the time domain pulse envelope. In analogy to the rectangular pulse, we plot the measured and simulated transmission as a function of the time, accompanied by the scaled input and resonator field in Figure 4.24(b). For this pulse

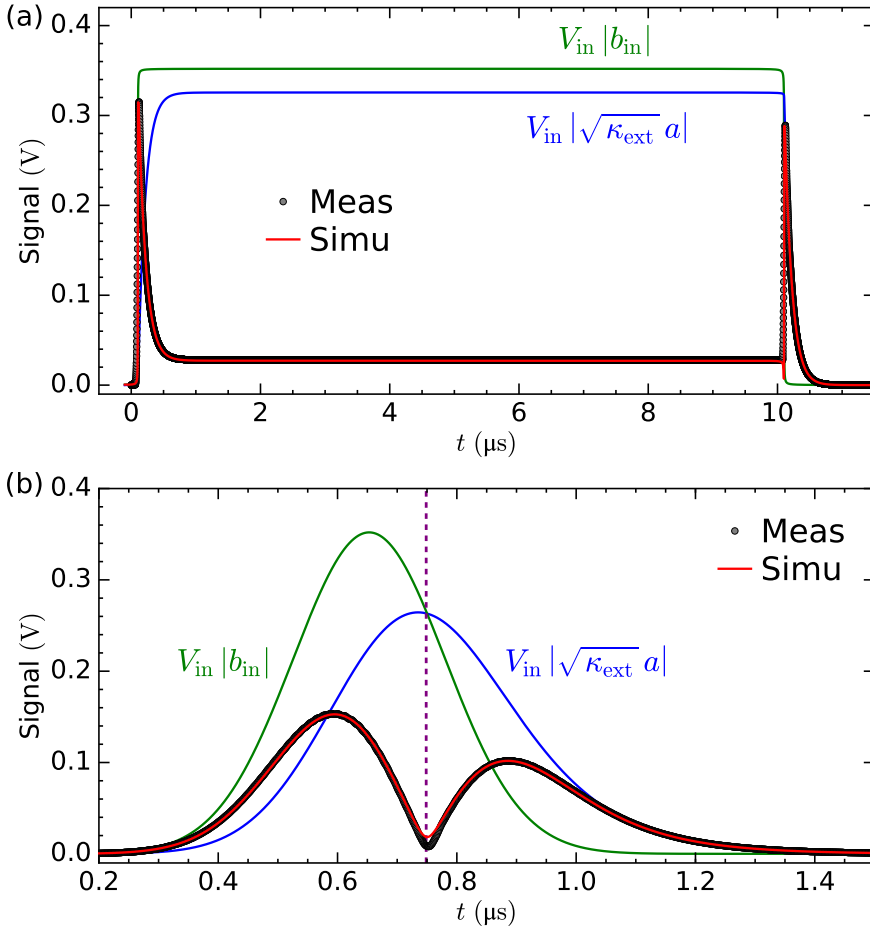


**Figure 4.24:** Measured and simulated resonator dynamics of a resonant excitation of resonator SR4 with a  $10\mu\text{s}$  rectangular pulse (a) and a  $0.3\mu\text{s}$  Gaussian pulse (b). The detected magnitude of the transmitted signal  $\sqrt{I^2 + Q^2}$  is plotted as a function of time  $t$ . The dimensionless quantities  $b_{\text{in}}(t)$  and  $-\sqrt{\kappa_{\text{ext}}}a(t)$  represent the input to the equation of motion (Eq. (4.36)) and its solution, respectively. They are scaled to the detected level of the input voltage  $V_{\text{in}} = 0.352\text{V}$ , which was extracted from offresonant measurements (not shown here). The simulated transmission signal (red curve) is obtained with the right-hand side of Eq. (4.37). The vertical dashed purple line in (b) marks the time  $t \approx 0.75\mu\text{s}$ , where  $|b_{\text{in}}(t)| = |\sqrt{\kappa_{\text{ext}}}a(t)|$ , which coincides with the local minimum of the transmission magnitude.

shape, we observe a good agreement between measurement and simulation.

Remarkably, the time-resolved transmission exhibits a local minimum at  $t \approx 0.75\mu\text{s}$ , which is due to a cancellation of the input signal (green) and the signal coupling back from the resonator to the transmission line (blue), as shown in Eq. (4.37).

In general, the transmitted signal<sup>11</sup>  $S_{21}(t) \cdot V_{\text{in}}$  is a sum of the two oscillating signals  $V_{\text{in}} \cdot b_{\text{in}}(t)$  and  $-V_{\text{in}} \cdot \sqrt{\kappa_{\text{ext}}}a(t)$ , which are perfectly opposite in phase and have a time-dependent magnitude. This means, that the transmission is in phase with  $b_{\text{in}}(t)$  for  $|b_{\text{in}}(t)| > |\sqrt{\kappa_{\text{ext}}}a(t)|$  (left side of the purple dashed line in Figure 4.24(a), i.e.  $t < 0.75\mu\text{s}$ ) and out of phase with  $b_{\text{in}}(t)$  otherwise. The situation becomes more complex when considering slightly offresonant excitations ( $\Delta/2\pi \neq$

<sup>11</sup> Note that we plotted  $\sqrt{I^2 + Q^2} = |S_{21}(t) \cdot V_{\text{in}}| \geq 0$  in Figure 4.24.

0), where we expect a non-zero phase shift between the drive and the resonator field ( $\varphi_a \neq 0$ , cf. Section 2.1.2) from theory, illustrated in Figure 2.2(b). In this case, the sum of the two signal contributions with time-dependent magnitudes results in a time-dependent phase relation  $\varphi_t(t)$ . The latter undergoes a rather continuous transition from  $\varphi_t = 0$  at the beginning of the excitation to  $\varphi_t = \pi$  after the end of the excitation, in contrast to the rather sudden transition in case of  $\Delta/2\pi = 0$ .

## 4.4 Summary

We developed three LER designs (CR, MR, SR) and estimated their resonance frequencies using simple models for the resonators' inductance and capacitance to a very good agreement with the values obtained from pre-characterization measurements. We established FEM simulations for modeling the LER properties by showing a very good matching of simulation and measurement results. Moreover, we demonstrated for each resonator design the tunability of the resonance frequency and the external coupling strength  $\kappa_{\text{ext}}$  by altering geometric parameters.

We fabricated a chip with a total of 14 resonators and performed a characterization with and without attached phosphorus doped silicon sample. In the course of this, we showed using FEM simulations, that the resonance frequency shift due to the presence of the sample reveals information about the sample mounting imperfection (gap width between sample and resonator surface) and allows to roughly approximate the filling factor. Additionally, we assigned the 14 resonance dips of the chip with mounted sample to either of the three resonator types by utilizing the observation, that different resonator designs show different temperature or magnetic field induced frequency shifts.

The novel SR design concept is based on the idea of a planar coil inductor and thus realizes parallel current directions in neighbouring strip sections, which leads to a positive contribution of the strip sections' mutual inductance to the total inductance. In comparison to resonators with meandering structures (CR, MR), this property results in a decreased ratio  $\alpha$  of kinetic to total inductance, which grants the SR a higher robustness of resonance frequency and reduced internal loss rates for increased temperatures, as we observed in CW measurements. Furthermore, the SR shows an enlarged mode volume and an improved homogeneity of its magnetic excitation field  $B_1$ , as a consequence of the constructive far field superpositions of  $B_1$  field contributions due to the parallel current flow in neighbouring strip sections. We discussed the expected sensitivity in various ESR experiments when using either resonator type. We particularly find that the SR is advantageous for pulsed ESR experiments with thin samples (tens of  $\mu\text{m}$ ).

Finally, we were able to reproduce the steady-state transmission acquired in CW measurements with the time domain setup by applying rectangular  $\mu\text{s}$ -pulses to the resonator. Additionally, we measured the transient transmission  $S_{21}(t)$  for pulsed excitations with rectangular and Gaussian shaped pulses, and simulated  $S_{21}(t)$  ab initio using the resonator parameters ( $f_r$ ,  $\kappa$ ,  $\kappa_{\text{ext}}$ ,  $\varphi_r$ ) in combination with the equation of motion. Both results show an excellent agreement. This verification of the theoretical framework enables the simulation of the resonator field  $a(t)$  and thus the dynamic magnetic field transient ( $|B_1(t)| \propto |a(t)|$ ) for arbitrary pulse shapes and sequences,

which ultimately allows a precise prediction of the outcome of pulsed ESR experiments.

## Chapter 5

# Continuous Wave Electron Spin Resonance

In this chapter we present the continuous wave (CW) electron spin resonance (ESR) characterization of phosphorus doped natural silicon. We extract the collective coupling strength of the spin ensemble from spectroscopy data and illustrate the influence of the resonator design on the filling factor of the ESR sample, which is a crucial parameter for achieving a strong collective coupling. Furthermore, we investigate the power dependent saturation of the spin system and provide a model for describing the observed behaviour. Finally, we focus on temperature effects contributing to the temperature dependence of the collective coupling rate.

### 5.1 Collective Coupling of a Spin Ensemble to a Lumped Element Resonator

In this section we characterize the spectroscopic features of phosphorus doped silicon using CW ESR measurements. The sample investigated is a silicon crystal with natural isotope composition and is doped with a concentration of  $[P] = 2 \cdot 10^{17} \text{ cm}^{-3}$ . This concentration is one order of magnitude below the metal to insulator transition of  $3.6 \cdot 10^{18} \text{ cm}^{-3}$  [77], where the ESR signal of hyperfine split isolated phosphorus donors is expected to vanish [78]. Due to the  $^{29}\text{Si}$  concentration of  $\approx 4.7\%$  in natural silicon, we expect a reduced spin-spin relaxation time  $T_2$ , as a consequence of nuclear-induced spectral diffusion [79].

#### 5.1.1 Field Calibration

To extract spectroscopic information from the ESR experiment, a field calibration is essential. This is in particular the case, because we use a superconducting solenoid magnet for the generation of the static magnetic field, typically exhibiting trapped flux and thus either an offset field and/or a slight modification to the current to field ratio [80]. This effect can be accounted for by performing an *in situ* calibration experiment. We choose DiPhenyl-Picryl-Hydrazyl (DPPH) as a spin marker with the known g-factor of 2.0036 [81]. The DPPH placed on the resonator CR0 and CR5 with

the frequencies 3.6905 GHz and 6.6007 GHz, respectively, allow to determine the static magnetic field offset and account for deviations in the current to field conversion ratio (e.g. due to a slight deviation in the spatial position of the sample). For this purpose, we tune the Larmor frequency  $\omega_{\text{Larmor}}$  of unpaired spins in DPPH into resonance with either microwave resonator. The larmor frequency is given by [65]

$$\omega_{\text{Larmor}} = \frac{g\mu_B}{\hbar}B_0 = \gamma B_0, \quad (5.1)$$

where  $g$  is the electron g-factor,  $\mu_B$  is the Bohr magneton and  $\gamma$  is the gyromagnetic ratio. We tune  $\omega_{\text{Larmor}}$  by varying the static magnetic field. Thus, we find the DPPH in resonance with resonator CR0 and CR5 at a set magnetic field of  $B_{0,\text{set}} = 141.75$  mT and  $B_{0,\text{set}} = 242.20$  mT, respectively. Comparing these results with the values expected form Eq. (5.1), we obtain two pairs of set and real values for the static magnetic field. A linear interpolation yields the calibration curve

$$B_0 = 1.033 \cdot B_{0,\text{set}} - 14.8 \text{ mT}, \quad (5.2)$$

which gives the real magnetic field  $B_0$  as a function of the set field  $B_{0,\text{set}}$ . We observe a large offset ( $-14.8$  mT) and a slight deviation in the current to field ratio (1.033).

The calibration is subject to slight deviations upon each field sweep measurement. Additionally, it has errors inherited from the measurement of the DPPH resonant magnetic field. Hence, we decide to generally plot spectroscopic data against the set magnetic field  $B_{0,\text{set}}$ .

However, the calibration (Eq. (5.2)) is essential for estimating the field range of interest, where the magnetic resonance of the spin system is expected.

### 5.1.2 Spectroscopic Characterization

Here, we present continuous wave ESR measurements on the spin ensemble in phosphorus doped silicon coupled to the capacitively shunted meander resonator CR3 with  $Q \approx 33000$ . We perform CW transmission measurements at  $T = 1.6$  K with a 200 kHz frequency span centered on 4539.78 MHz and a magnetic field between 168.21 mT and 173.7 mT centered on the expected resonance field. In order to prevent a saturation of the spin system (see Section 5.2), we chose a low power at sample of  $-100$  dBm = 0.1 pW, which corresponds to a resonator photon number of  $n = 4 \cdot 10^4$  calculated with Eq. (2.16). This in general leads to a decreased signal to noise ratio (SNR), which is compensated by using a low intermediate frequency bandwidth (IFBW) in addition to the averaging feature of the VNA, which results in an effective IFBW of 1 Hz. The in situ calibration experiment used for calculating the calibration curve in Eq. (5.2) was acquired right after the here presented measurement. We show the power transmission  $|S_{21}|^2$  as a function of the uncalibrated magnetic field  $B_{0,\text{set}}$  and the drive frequency in Figure 5.1(a). Here we consider the uncalibrated raw transmission data including line attenuation and amplification. When increasing the static magnetic field  $B_{0,\text{set}}$ , we observe a decreasing resonance frequency  $\omega_r/2\pi$  accompanied by two pronounced features at  $B_{0,\text{LF}} = 169.51$  mT and  $B_{0,\text{HF}} = 172.99$  mT. Increasing  $B_{0,\text{set}}$  is associated with an increasing kinetic inductance of the superconductor, which in turn leads to a decreasing resonance frequency, as discussed in Section 4.2.4.

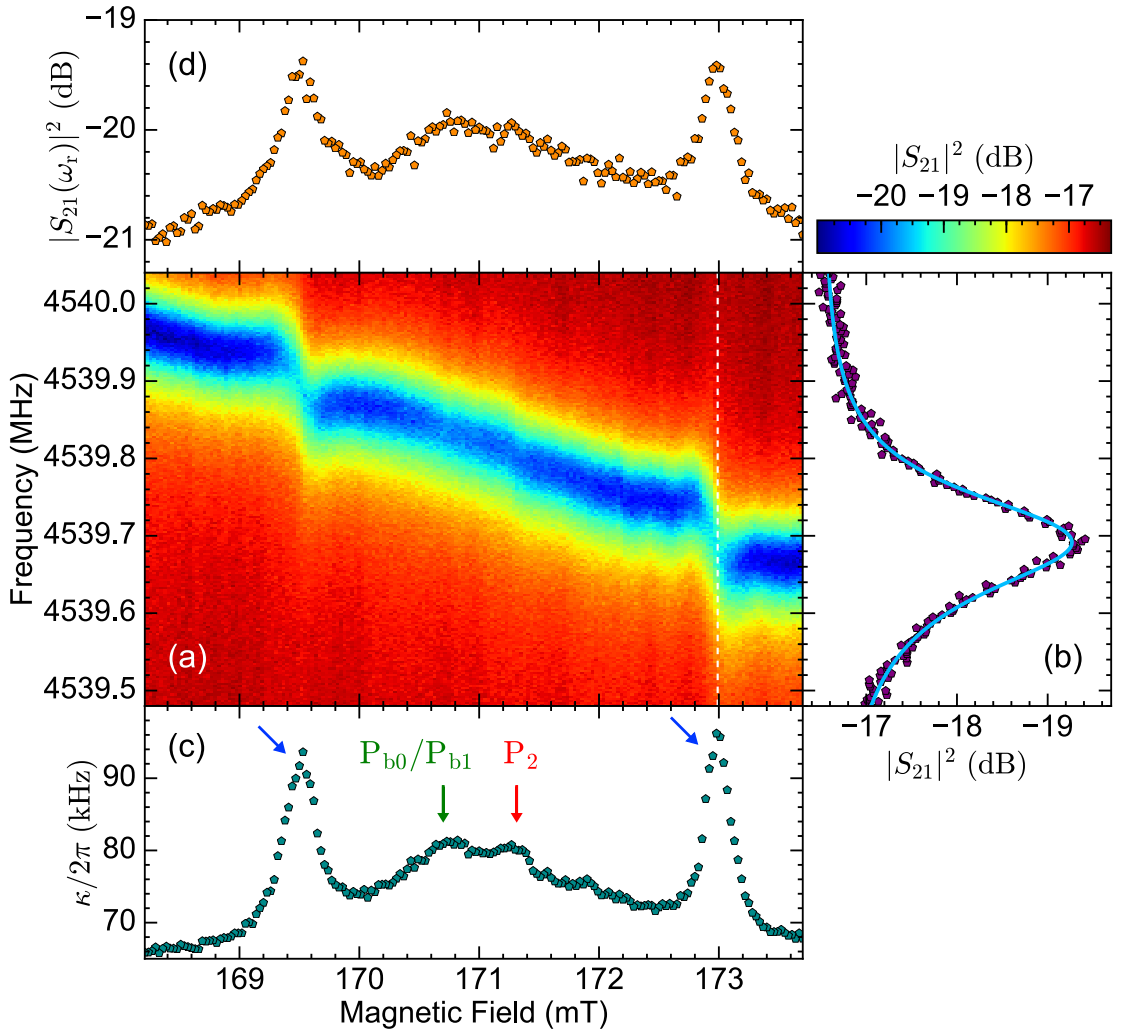


**Figure 5.1:** Continuous wave electron spin resonance of unpaired electrons in phosphorus doped silicon. The drive frequency was varied around the resonance frequency  $\omega_r/2\pi \approx 4539.8$  MHz of the resonator CR3 with  $Q \approx 33000$ . The measurement was performed at 1.6 K with a sample power of  $-100$  dBm =  $0.1$  pW and an effective IFBW of 1 Hz. (a) Color coded uncalibrated power transmission  $|S_{21}|^2$  as a function of the uncalibrated static magnetic field  $B_{0,\text{set}}$  and the drive frequency  $\omega/2\pi$ . (b) Uncalibrated power transmission plotted against frequency at the field  $B_{0,\text{set}} = 172.99$  mT (indicated by the dashed white line in (a)). Blue line illustrates a fit to the data using the DCM model. (c) Resonator loss rate  $\kappa/2\pi$  as a function of the magnetic field, extracted from a fit of a modified version<sup>12</sup> of the DCM model to the transmission data for each magnetic field. Blue, green and red arrows mark spectroscopic features (see text). (d) Uncalibrated power transmission  $|S_{21}(\omega_r)|^2$  at the field-dependent resonance frequency as a function of the magnetic field  $B_{0,\text{set}}$ .

<sup>12</sup> Due to the very low drive power required for CW measurements at 1.5 K in combination with temperature fluctuations, the transmission data and therefore the lineshape fits are subject to high noise, which makes extraction of the linewidth spectrum (Figure 5.1(c)) hardly possible. We circumvent this issue, by reducing the degrees of freedom in the DCM fit, which is accomplished by fixing the external loss rate  $\kappa_{\text{ext}}$  to the value obtained offresonant from magnetic resonance. This is justified, since in principle,  $\kappa_{\text{ext}}$  is not expected to be substantially dependent on the coupling to the spin system. This method produces consistent spectroscopic data, however, its limitations are discussed below.

In Figure 5.1(b), we plot the power transmission along the white dashed line in Figure 5.1(a) at  $B_{0,\text{HF}}$  as a function of the drive frequency, showing a minimal uncalibrated power transmission of  $|S_{21}(\omega_r/2\pi)|^2 = -19.4 \text{ dBm}$ . For each magnetic field, the transmission is analyzed with a modified version<sup>13</sup> of the DCM model (cf. Section 4.2.1) as exemplarily illustrated by the blue line in Figure 5.1(b). The extracted half width at half maximum  $\kappa/2\pi$  is plotted against the magnetic field in Figure 5.1(c). The background of the resonator linewidth exhibits a continuous broadening from 67 kHz to 78 kHz, when moving from either border of the presented  $B_{0,\text{set}}$  span to its center. This behaviour is superposed by two peaks at  $B_{0,\text{LF}}$  and  $B_{0,\text{HF}}$  (blue arrows) with a maximal linewidth enhancement of roughly 40 %.

We attribute the peaks to the characteristic hyperfine splitting of unpaired phosphorus electrons in silicon [8]. In theory, the magnetic resonance condition in ESR of a  $S = 1/2$  and  $I = 1/2$  spin system with solely a fermi contact hyperfine interaction is in good approximation described by

$$\omega_r = \omega_s = \gamma_{\text{eP}} B_0 \pm \frac{A}{2h}, \quad (5.3)$$

where  $\omega_s$  denotes the spin resonance frequency,  $\gamma_{\text{eP}}$  the gyromagnetic ratio of phosphorus in silicon and  $A/h = 117.53 \text{ MHz}$  denotes the hyperfine interaction constant [9]. At the resonance condition, the loss rate  $\kappa/2\pi$  of the resonator is increased since the coupling to the spin system represents an additional loss mechanisms for the excitation photons confined to the resonator. From Eq. (5.3), we expect the two magnetic resonances to be separated by  $A/(h\gamma_{\text{eP}}) = 4.20 \text{ mT}$ . However, we observe an uncalibrated hyperfine splitting of 3.48 mT, which changes to 3.58 mT after taking into account the calibration of the static magnetic field (cf. Eq. (5.2)). Furthermore, we calculate the electron g-factor of phosphorus in silicon using the central field  $B_{0,\text{center}} = (B_{0,\text{LF}}^{(\text{calib.})} + B_{0,\text{HF}}^{(\text{calib.})})/2 = 162.08 \text{ mT}$  obtained from the calibrated resonant fields  $B_{0,\text{LF/HF}}^{(\text{calib.})}$ , and find

$$g_{\text{eP}}^{(\text{meas.})} = \frac{\omega_r}{B_{0,\text{center}}} \frac{\hbar}{\mu_B} = 2.001, \quad (5.4)$$

which is in good agreement with the reported value 1.9985 [47], taking into account the error margins of the calibration curve (Eq. (5.2)). This result is a general verification of the  $B_0$  calibration given and confirms that the field calibration cannot cause the mismatch between the measured and expected hyperfine splitting. Additionally, a mismatch in the measured frequency can be excluded due to a precise calibration of the VNA. Moreover, we emphasize that the resonance frequency shift of the resonator between the two magnetic resonances, i.e.  $\Delta f_r = f_r(B_{0,\text{LF}}) - f_r(B_{0,\text{HF}}) = 0.2 \text{ MHz}$ , corresponds to a change of  $\approx 0.005 \%$  in the hyperfine splitting, yielding no explanation for the observed mismatch. The reduced hyperfine splitting might be a consequence of induced strain in the phosphorus doped silicon crystal [82] due to the pressure of the copper screw applied to the sample (cf. Section 3.2). However, further investigations are needed to understand or resolve the discrepancy between the measured and theoretically expected hyperfine splitting.

Moreover, we attribute the spectroscopic features denoted by the green arrow in Figure 5.1(c) to dangling bonds ( $P_{b0}/P_{b1}$ ), which represent defects at the Si/SiO<sub>2</sub> interface exhibiting an elec-

<sup>13</sup> See Footnote <sup>12</sup>.

tron g-factor around 2.005 [83, 84]. For doping concentrations exceeding  $6 \cdot 10^{16} \text{ cm}^{-3}$ , the wave functions of unpaired electrons of the phosphorus donors overlap significantly, forming antiferromagnetically exchange coupled  $P_2$  dimers with a resonance magnetic field (red arrow) in between the hyperfine split transitions [8, 85–87].

In Figure 5.1(d), we mimic the detection technique of a reflection cavity setup in conventional ESR [44], by considering the transmitted signal at the moving resonance frequency, which changes significantly with the magnetic field for microwave resonators, in contrast to conventional ESR cavities. The features in the resulting plot, are comparable to the observations of the linewidth spectrum in Figure 5.1(c). This is expected from theory, since the transmission at resonance frequency (cf. Eq. (2.12))

$$|S_{21}(\omega_r)| = \left|1 - \frac{\kappa_{\text{ext}}}{\kappa}\right| \quad (5.5)$$

increases upon linewidth broadening.

### 5.1.3 Characterization of the Spin Ensemble

The data processing for CW measurements at 1.5 K requires a modified version of the DCM fit, where the external coupling rate is fixed, reducing the degrees of freedom and thereby allowing to obtain consistent spectroscopy data. However, the temperature dependence of the collective coupling (cf. Section 5.3) indicates a systematic underestimation of  $g_{\text{eff}}$  for measurements evaluated with this modified fitting procedure. Motivated by this, we characterize the collective coupling of the spin system coupled to the resonator SR4 based on measurements at 4 K, which can be evaluated with the unmodified DCM model.

Figure 5.2 shows the resonator linewidth  $\kappa/2\pi$  as a function of the static magnetic field for a measurement at 4 K with a sample power of  $-95 \text{ dBm}$ . The field range is restricted to the high field magnetic resonance of the phosphorus donors hyperfine split lines.

For fitting the resonance peak we use a Lorentzian model on top of a linear background, which accounts for either the large background signal in Figure 5.1(c) or the dependence  $\kappa(B_0)$ , which dominates at higher temperatures (cf. Section 4.2.3.2). The data is well-described by the fit curve of this model (magenta line), which yields a peak of  $\Delta\kappa/2\pi = 45 \pm 5 \text{ kHz}$  and a magnetic linewidth (full width at half maximum) of  $\Delta B = 0.18 \pm 0.02 \text{ mT}$ . The latter is related to the spin loss rate  $\gamma_s$  via

$$\gamma_s = \gamma_{\text{ep}} \frac{\Delta B_0}{2}, \quad (5.6)$$

which covers homogeneous and inhomogeneous broadening effects [44, 88]. With this relation, we find a loss rate of  $\gamma_s/2\pi = 2.5 \text{ MHz}$ . This value agrees with the reported inhomogeneous broadening due to the residual concentration of typically 4.7% of the isotope  $^{29}\text{Si}$  in the natural silicon crystal hosting the phosphorus doping atoms [79]. Additionally, we can calculate the phase memory time  $T_2^*$  which governs the Free Induction Decay (FID), i.e. the dephasing of a uniformly oriented spin magnetization in the xy-plane of the Bloch sphere [44]. With the equation [89]

$$T_2^* = \frac{2\pi}{\gamma_s}, \quad (5.7)$$

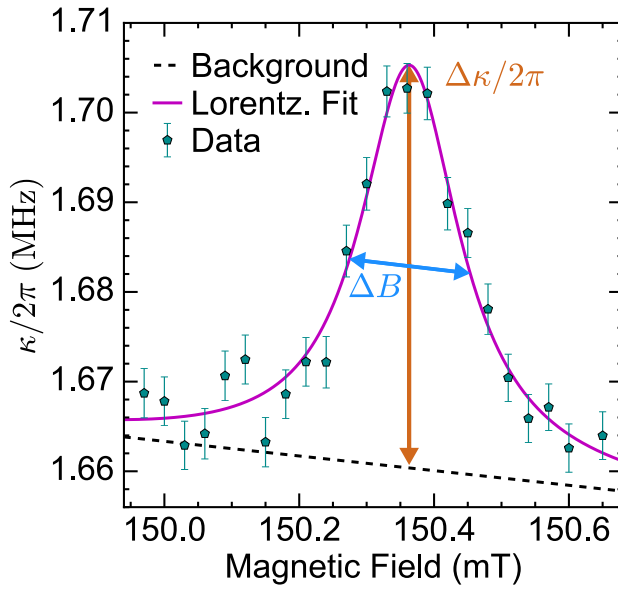


**Figure 5.2:** ESR Linewidth broadening of the spiral resonator SR4 coupled to the spin ensemble measured at  $T = 4\text{ K}$  with a sample power of  $-95\text{ dBm}$ . The resonator linewidth  $\kappa/2\pi$  is extracted from transmission measurements and plotted against the uncalibrated static magnetic field  $B_0$ . The fitting model for the linewidth broadening is composed of a Lorentzian function and a linear background, accounting for the large background signal accompanying the two hyperfine resonances in Figure 5.1(c). The fitted curve (magenta line) admits a peak of  $\Delta\kappa/2\pi = 45 \pm 5\text{ kHz}$  and full width at half maximum resonance broadening of  $\Delta B = 0.18 \pm 0.02\text{ mT}$ .

we find  $T_2^* = 400\text{ ns}$ .

Next, we focus on the collective coupling. According to Herskind *et al.* [90], we calculate the collective coupling between the spin system and the microwave resonator at magnetic resonance  $\omega_s = \omega_r$  (see Eq. (5.3)) to

$$g_{\text{eff}} = \sqrt{\gamma_s \Delta\kappa} = 2\pi \cdot (335\text{ kHz} \pm 74\text{ kHz}), \quad (5.8)$$

where the uncertainty is based on the fitting uncertainties of  $\Delta\kappa$  and  $\Delta B_0$ .

We compare this result to the collective coupling expected from theory, which is given by [91]

$$g_{\text{eff}} = \frac{g_{\text{eP}} \mu_B}{2\hbar} \sqrt{\frac{\mu_0 \rho \hbar \omega_r v_m}{2}}, \quad (5.9)$$

where  $\rho$  is the density of spins and  $v_m$  is the filling factor, which is defined for homogeneous field distributions as the ratio between the ESR sample volume  $V_s$  and the mode volume  $V_m$ . The sample mounting technique used for our experiments (cf. Section 3.2) allows a maximal filling factor of  $v_{m,\text{max}} = 0.5$ , which is the case when the sample completely covers the upper hemisphere. Moreover, the effective density of the spins contributing the magnetic resonance corresponds in a good approximation to half the doping density, i.e.  $\rho_{\text{eff}} = 1 \cdot 10^{17}\text{ cm}^{-3}$ , due to the equally populated ground states of the two hyperfine split transitions [54].

Taking the thermal polarization  $0 < P(T) < 1$  of the spin system into account modifies Eq. (5.9) to [31]

$$g_{\text{eff}} = \frac{g_{\text{eP}}\mu_{\text{B}}}{2\hbar} \sqrt{\frac{\mu_0\rho_{\text{eff}}\hbar\omega_{\text{r}}P(T)\nu_{\text{m}}}{2}}, \quad (5.10)$$

Generally, the thermal polarization is described by the Brillouin function, however, for temperatures beyond the millikelvin range, one uses the Langevin function as a good approximation [92]

$$P(T) = L(x) = \coth(x) - \frac{1}{x} \approx \frac{x}{3}, \quad (5.11)$$

with the ratio  $x = g_{\text{eP}}\mu_{\text{B}}JB_0/k_{\text{B}}T$  of Zeeman energy to thermal energy, where  $J = 1/2$  is the total angular momentum quantum number. For  $x \ll 1$ , which in our case translates to  $T \gg 0.10 \text{ K}$ , we can safely assume the approximation of the Langevin function in Eq. (5.11). This yields a thermal polarization of 0.84% at 4K.

Finally, we assume an ideal filling factor  $\nu_{\text{m}} = 0.5$ , corresponding to the upper hemisphere completely filled with phosphorus doped silicon. Eq. (5.10) then yields a maximal realizable collective coupling rate  $g_{\text{eff,max}}$  with the given spin density  $\rho_{\text{eff}}$  at 4K

$$g_{\text{eff,max}} = 2\pi \cdot 383 \text{ kHz}. \quad (5.12)$$

The small difference between the measured value of 335 kHz and theoretically predicted value of 383 kHz (Eq. (5.10)) is attributed the limitations of the spiral resonator due to an less-than-ideal  $B_1$ -field orientation. Hence, the experimental result is consistent with theory within the error margins of the measured  $g_{\text{eff}}$  (11% inherited<sup>14</sup> from errors of  $\Delta\kappa$  and  $\gamma_s$ ). Moreover, this indicates a close-to-perfect filling factor  $\nu_{\text{m}} \approx 0.5$ .

Finally, the hybrid system of the spin ensemble coupled to the microwave resonator SR4 is in the weak coupling regime due to  $g_{\text{eff}} < \gamma_s$  exhibiting a cooperativity of [26]

$$C = \frac{g_{\text{eff}}^2}{\kappa\gamma_s} = 0.027 \ll 1. \quad (5.13)$$

Assuming the same coupling strength  $g_{\text{eff}} = 2\pi \cdot 335 \text{ kHz}$  for a spin ensemble coupled to the highest quality resonator CR3 (cf. Figure 5.1) with  $\kappa/2\pi = 65 \text{ kHz}$  yields a remarkable cooperativity of  $C = 0.69$  for 1.6K. However, it has been shown for the case  $\kappa \ll \gamma_s$ , that a transmission with two minima at the magnetic resonance field, which corresponds to the onset of an anticrossing, is expected when  $g_{\text{eff}} > 0.64\gamma_s$  [93]. For our spin system, this corresponds to  $g_{\text{eff}}/2\pi > 1.6 \text{ MHz}$ . Hence, the study of an avoided crossing at liquid helium temperatures using a spin ensemble of phosphorus donors in natural silicon is beyond reach.

<sup>14</sup> The relative error of  $g_{\text{eff}} = \sqrt{\gamma_s\Delta\kappa}$  is inherited from the relative errors  $\delta\Delta\kappa$  and  $\delta\gamma_s$  via  $\delta g_{\text{eff}} = \frac{1}{2}(\delta\Delta\kappa + \delta\gamma_s)$ .

### 5.1.4 Modeling of the Filling Factor

We compare the collective coupling rate expected from the simulated  $B_1$ -distribution of the resonator to the maximal collective coupling rate  $g_{\text{eff,max}}$ , which is defined for convenience using the filling factor  $\nu_{m,\text{max}} = 0.5$ , as this is the largest filling factor realizable with our sample mounting technique.

A finite gap with width  $d_{\text{gap}}$  between the resonator surface and the ESR sample leads to a decreased filling factor  $\nu_m = \nu_m(d_{\text{gap}})$ . The dependence  $\nu_m(d_{\text{gap}})$  is essentially given by the three-dimensional  $B_1$ -field distribution and is therefore dependent on the resonator design. However, due to the high inhomogeneity of the dynamic magnetic field of a LER, it is not useful to define the filling factor as the ratio of sample to mode volume. Hence, we incorporate the  $B_1$ -distribution into the calculation of  $g_{\text{eff}}$  (see Eq. (5.9)) following [31, 54]

$$g_{\text{eff}} = \frac{g_{\text{eP}}\mu_B}{2\hbar} \sqrt{\sum_{\mathbf{r} \in V_s} |B_{1,yz}^{\text{norm}}(\mathbf{r})|^2}, \quad (5.14)$$

where the sum includes all spin locations in the sample volume and the normalized dynamic magnetic field fulfills (cf. Eq. (5.9) with filling factor  $\nu_m = 1$ )

$$\sum_{\mathbf{r} \in V_m} |B_1^{\text{norm}}(\mathbf{r})|^2 = \frac{\mu_0 \rho \hbar \omega_r}{2}. \quad (5.15)$$

In Eq. (5.14) we took into account, that for ESR applications only the  $yz$ -component of  $B_1$  contributes to the manipulation of spins. With this, we rewrite the collective coupling for arbitrary sample volumes  $V_s$  to

$$g_{\text{eff}} = \frac{g_{\text{eP}}\mu_B}{2\hbar} \sqrt{\frac{\mu_0 \rho \hbar \omega_r}{2} \frac{\sum_{\mathbf{r} \in V_s} |B_{1,yz}^{\text{norm}}(\mathbf{r})|^2}{\sum_{\mathbf{r} \in V_m} |B_1^{\text{norm}}(\mathbf{r})|^2}}. \quad (5.16)$$

This expression has the advantage, that we can use the unnormalized dynamic magnetic fields  $B_1$  and  $B_{1,yz}$ , since any normalization factor is cancelled out.

Figure 5.3 shows the collective coupling  $g_{\text{eff}}$  as function of  $d_{\text{gap}}$ , where  $g_{\text{eff}}$  is calculated from the  $B_1$  distributions presented in Section 4.1.5 and normalized to  $g_{\text{eff,max}}$ . Note that  $g_{\text{eff,max}}$  is calculated with a filling factor of  $\nu_{m,\text{max}} = 0.5$ .

At zero gap width, we observe the expected reduction of  $g_{\text{eff}}^{(\text{SR})}$  of the spiral resonator due to the orientation of the dynamic magnetic field in parts of the spiral resonator mode volume (cf. Section 4.1.5). The collective coupling to the CR and MR shows a nonlinear decrease, when increasing  $d_{\text{gap}}$ , with values  $< 4\%$  for gaps around  $40\mu\text{m}$ . As opposed to this, the spiral resonator shows a flat decrease of  $g_{\text{eff}}$  with increasing  $d_{\text{gap}}$ , with  $g_{\text{eff}}/g_{\text{eff,max}} \approx 30\%$  at  $50\mu\text{m}$ , which reflects the flat descent of  $B_1^{(\text{SR})}(z)$  in the far field.

In realistic mounting conditions, the gap width can be in the order of  $10\mu\text{m}$  due to surface imperfections or contamination [26]. As qualitatively described in Section 4.1.5, we conclude that using the spiral resonator enables higher collective coupling rates already for gaps larger than  $3\mu\text{m}$  and is clearly beneficial for gaps in the order of tens of  $\mu\text{m}$ .

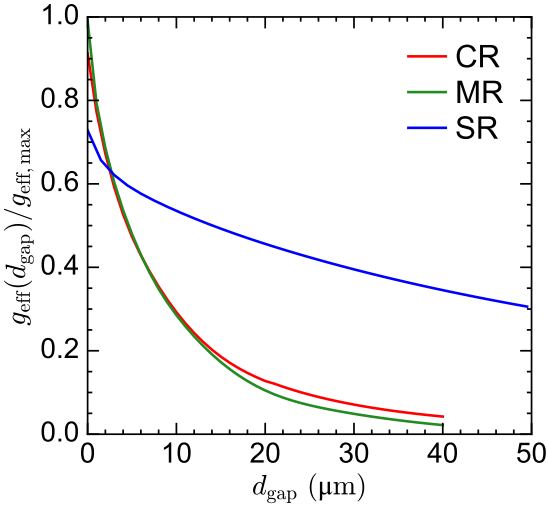


**Figure 5.3:** Collective coupling of a spin ensemble to a resonator depending on the gap width  $d_{\text{gap}}$  between the resonator surface and the sample hosting the spin system. The coupling rate  $g_{\text{eff}}$  is normalized to the theoretical upper limit  $g_{\text{eff}, \text{max}}$  and plotted as a function of  $d_{\text{gap}}$  for multiple resonator designs.  $g_{\text{eff}}$  is calculated based on three-dimensional  $B_1$ -field data extracted from FEM simulations (cf. Section 4.1.5).

## 5.2 Power Dependence of $g_{\text{eff}}$

In this section, we investigate the power dependence of the collective coupling between the microwave resonator and the spin system.

We perform CW measurements at 1.5 K with a number of resonators using drive powers in the wide range of  $-125$  dBm to  $-40$  dBm. The magnetic field is varied around the high field hyperfine transition. The collective coupling rate  $g_{\text{eff}}$  is extracted as demonstrated in Section 5.1.3. Instead of calculating the spin loss rate  $\gamma_s$  individually for each acquired linewidth spectrum, we assume a fixed value of  $\gamma_s = 2\pi \cdot 2.5$  MHz, which was obtained for the SR4 at 4 K (cf. Section 5.1.3).

In Figure 5.4, we depicted the resulting collective coupling strengths as a function of the sample power  $P_s$  in units of dBm for a total of seven resonators covering the three LER designs presented in Section 4.1.

In general, we observe small collective coupling rates for high sample powers  $P_s$  and vice versa. At low sample powers,  $g_{\text{eff}}$  is only weakly dependent on  $P_s$ . Between the two extreme cases of high to low powers, the collective coupling strength shows a continuous increase. We observe different values of saturation power for different resonators. This is attributed to an individual conversion of sample power into  $B_1$ -field magnitude for each resonator, which is, as shown further below, the crucial parameter for the mechanism of saturation.

In CW ESR, the magnetization of the spin system is continuously driven by the magnetic excitation field of the resonator. The coupling rate of microwave photons from resonator to spin ensemble and vice versa depends on the thermal polarization  $P(T)$  ( $g_{\text{eff}} \propto \sqrt{P(T)}$ ). However, increasing the microwave power, successively leads to an equal population of the two energy levels of the spin system ( $m_s = \pm 1/2$ ), which reduces the polarization  $P$  to zero [94]. This explains the decreasing collective coupling rate with increasing powers observed in Figure 5.4.

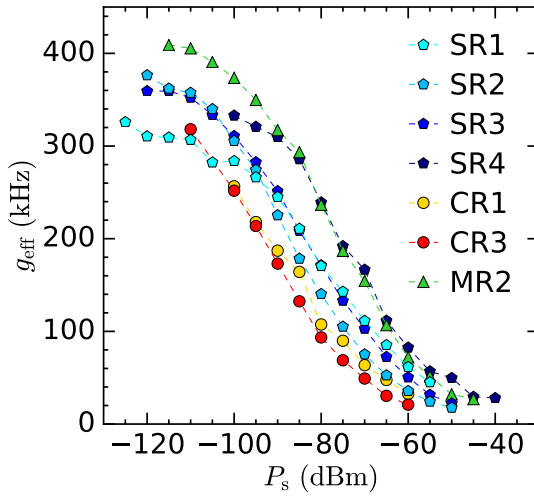


**Figure 5.4:** Collective coupling strength  $g_{\text{eff}}$  of the high field spin transition as a function of the sample power  $P_s$  for several lumped element resonators measured at 1.5 K. Dashed lines connecting data points of the same resonator are added as a guide to the eye.

We present a quantitative description of the spin ensemble saturation, which allows to model the power dependence of  $g_{\text{eff}}$  based on a resonator's dynamic magnetic field distribution.

We assume an individual saturation of spins or spin packets in a paramagnetic spin ensemble [88]. In conventional CW ESR, the saturation factor of an inhomogeneously broadened lineshape is defined as [95, 96]

$$S_{\text{Sat}} = \frac{1}{\sqrt{1 + s\gamma^2 B_1^2 T_1 T_2^*}}, \quad (5.17)$$

where  $s$  is a correction factor accounting for the lineshape of spin packets, which can be Lorentzian, Gaussian or a mixture of both [95, 97].  $S_{\text{Sat}}$  essentially depends on the product of  $B_1^2$  and the relaxation times  $T_1$  and  $T_2^*$ . The spin system is in the unsaturated regime  $S_{\text{Sat}} \approx 1$ , when  $\gamma B_1 \ll 1/\sqrt{sT_1 T_2^*}$ , i.e. the relaxation times are small compared to  $\gamma B_1$ . With this factor, the CW ESR signal can be written as [96]

$$S_{\text{CW}} = S_0 S_{\text{Sat}} B_1, \quad (5.18)$$

with some normalization constant  $S_0$ . If we incorporate this into the calculation of  $g_{\text{eff}}$  (Eq. (5.16)) by considering  $S_{\text{Sat}} B_{1,yz}$  instead of  $B_{1,yz}$ , we find

$$g_{\text{eff}} = \frac{g_{\text{ep}} \mu_B}{2\hbar} \sqrt{\frac{\mu_0 \rho \hbar \omega_r}{2} \frac{\sum_{\mathbf{r} \in V_s} |S_{\text{Sat}} B_{1,yz}(\mathbf{r})|^2}{\sum_{\mathbf{r} \in V_m} |B_1(\mathbf{r})|^2}}. \quad (5.19)$$

Thus, the collective coupling strength depends on the sample power  $P_s$  via the relation  $B_1 \propto \sqrt{P_s}$ . For three resonators, one of each design, we again plot the measured and simulated collective coupling strength as a function of the sample power in Figure 5.5.

The measured values of  $g_{\text{eff}}$  are normalization to the unsaturated  $g_{\text{eff}}$  of MR2 (green triangles), whereas the simulated  $g_{\text{eff}}$  were individually rescaled for each resonator to its measured unsat-

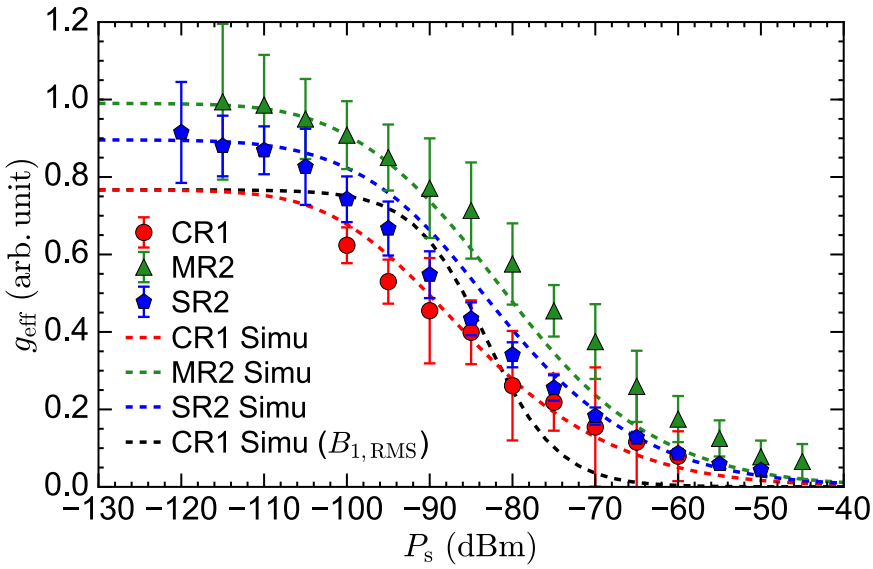


**Figure 5.5:** Normalized collective coupling rates  $g_{\text{eff}}$  as a function of sample power  $P_s$  measured and simulated for the resonators CR1, MR2 and SR2. The measurement data was taken from Figure 5.4 and normalized to the maximum of the MR2 resonator, which is  $g_{\text{eff}} = 2\pi \cdot 410 \text{ kHz}$ . Simulation data is obtained from Eq. (5.19), based on inhomogeneous  $B_1$  distributions, and rescaled to each resonator's maximum. The black line marks a simulation emulating a homogeneous dynamic magnetic field, where  $B_1$  is fixed to the root-mean-square of the  $B_1$  distribution of CR2.

urated (maximal) coupling strength. Using the results of CW ( $T_2^* = 400 \text{ ns}$ ) and pulsed ESR measurements ( $T_1 = 48 \text{ ms}$ ), we assume  $T_1 T_2^* = 19.2 \cdot 10^{-9} \text{ s}^2$ . Furthermore, the correction factor  $s$  was used as a mutual fitting parameter for the simulated  $g_{\text{eff}}$  (dashed lines in Figure 5.5), yielding  $s = 0.026$ .

The dashed blue, red and green curves were simulated using the inhomogeneous distribution of the SR, CR and MR, respectively. They show a good agreement with the measurement results taking into account the error margins of the measured collective coupling rates. Moreover, a simulation for CR1 was performed assuming a homogeneous dynamic magnetic field (black dashed line), which corresponds to the root-mean-square value of the  $B_1$  distribution. We observe that this simplified model is not suitable to describe the saturation behaviour. This reflects the fact the spins in the ensemble saturate independently of each other, only depending on the excitation field magnitude at their location in the mode volume.

### 5.3 Temperature Dependence of $g_{\text{eff}}$

Next, we investigate the temperature dependence of the collective coupling for the spiral resonator SR4. Figure 5.6 shows the collective coupling strength as a function of the sample power for temperatures between 1.55 K and 6.3 K.

We observe an increase of saturation power with increasing temperature. The unsaturated collective coupling rate shows higher values for lower temperatures. However, the value of  $g_{\text{eff}}$  measured for 1.55 K and 4 K are similar for low powers, despite the large temperature difference.

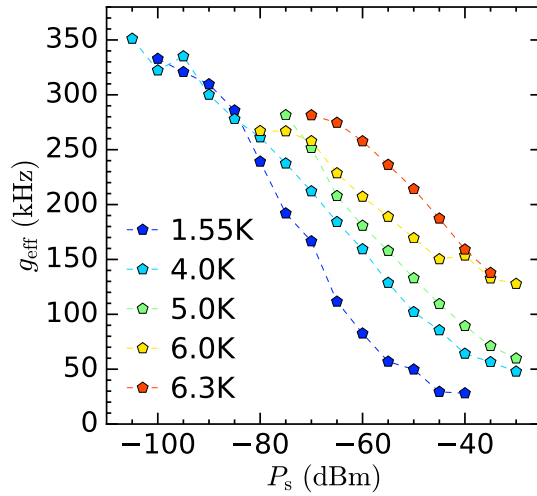


**Figure 5.6:** Temperature dependence of the collective coupling strength  $g_{\text{eff}}$  between the spiral resonator SR4 and the high field hyperfine split transition of phosphorus in silicon. The coupling rate  $g_{\text{eff}}$  is plotted as a function of the sample power  $P_s$  for different temperatures. Dashed lines connecting data points of the same temperature are added as a guide to the eye.

For low sample powers, where the spin system is completely unsaturated, the collective coupling strength mainly depends on the thermal polarization  $P(T)$  of the paramagnetic spin ensemble, more precisely  $g_{\text{eff}} \propto \sqrt{P(T)}$ , as shown by Eq. (5.10). For temperatures in the kelvin range, we can assume the relation  $P(T) \propto 1/T$  (cf. Eq. (5.11)), which yields an expected reduction of  $g_{\text{eff}}$  by a factor of roughly 2, when increasing the temperature from 1.55 K to 6.3 K. This is not observed in the measurement data set.

We attribute this deviation from theoretical prediction to the modified version of the DCM fit<sup>15</sup>, which is used only for fitting the data measured at 1.55 K. We assume, that the modified fitting model systematically underestimates the peak in the resonator linewidth (see Figure 5.2) and thus leads to a smaller  $g_{\text{eff}}$ . Additionally, the collective coupling rates in Figure 5.6 are calculated with a simple model, which assumes a homogeneous broadened lineshape (cf. Eq. (5.8)). This might lead to an underestimation of  $g_{\text{eff}}$  at low temperatures.

While not influenced by the thermal polarization, the saturation behaviour is strongly dependent on the phase memory time ( $T_2^*$ ) and the spin-lattice relaxation time ( $T_1$ ), as suggested by the saturation factor  $S_{\text{Sat}}$  (Eq. (5.17)). Essentially, the product  $T_1 T_2^*$  in the expression for  $S_{\text{Sat}}$  translates a decrease of  $T_1$  and  $T_2^*$  times into a higher saturation  $B_1$ -field magnitude and thus into a higher saturation sample power  $P_s$  ( $B_1 \propto \sqrt{P_s}$ ). Note that there is a variety of processes contributing to a linear or superlinear decrease of the characteristic relaxation times with increasing temperature [10, 44, 98]. This qualitatively agrees with the observations based on Figure 5.6.

Moreover, the exponential dependence of thermally induced losses of a superconducting microwave resonator (cf. Figure 4.18) contributes to the saturation behaviour. This is explained by the dependence of the resonator photon number  $n$  on the internal loss rate  $\kappa_{\text{int}}(T)$  (cf. Eq. (2.16))

<sup>15</sup> See footnote <sup>12</sup>

for  $\Delta = 0$ ) given by

$$n \propto \frac{1}{\kappa_{\text{ext}} + \kappa_{\text{int}}(T)}, \quad (5.20)$$

in combination with the relation  $B_1 \propto \sqrt{n}$ . This effect further reduces the saturation power with increasing temperature.

We conclude that continuous wave experiments on spin ensembles with high relaxation rates are more conveniently performed at higher temperatures, since several effects contribute to an increase of the saturation power, giving rise to higher SNR in microwave transmission measurements. However, the unsaturated collective coupling rate is expected to decrease with temperature as  $g_{\text{eff}} \propto 1/\sqrt{T}$ . Additionally, the quality factor of superconducting microwave resonators degrades drastically when approaching the critical temperature of the superconductor. Hence, there is an optimal operation temperature, which depends on multiple influencing factors, but most importantly, on the time dependence of the spin system's relaxation times.

## 5.4 Summary

We used CW measurements to characterize a spin ensemble consisting of phosphorus donors in natural silicon with a doping density of  $2 \cdot 10^{17} \text{ cm}^{-3}$  coupled to superconducting lumped element microwave resonators of different designs. We were able to identify spectroscopic features like the characteristic hyperfine splitting as well as dangling bonds on the Si/SiO<sub>2</sub> interface and exchange coupled phosphorus dimers. The magnetic linewidth of the high field hyperfine split transition translates into a spin loss rate of  $\gamma_s/2\pi = 2.5 \text{ MHz}$ , which is higher than the value reported for isotopically purified <sup>28</sup>Si crystals [79]. This is attributed to nuclear-induced spectral diffusion due to the presence of the nuclear spins of <sup>29</sup>Si atoms, which exhibit a concentration of 4.7 % in natural silicon. Moreover, we found a collective coupling rate of  $g_{\text{eff}}/2\pi = 335 \text{ kHz}$  of isolated phosphorus donors. For the spiral resonator with low quality factor, this result implies a cooperativity of  $C = 0.027$ , which classifies the hybrid system of spin ensemble and resonator into the weak coupling regime. However, the cooperativity approaches 1 for the resonator CR3 with the highest quality factor ( $\kappa/2\pi = 65 \text{ kHz}$ ). Theoretical estimations of the collective coupling rate taking into account the low thermal polarization of  $P(T) < 2\%$  at liquid helium temperatures and the high spin loss rate  $\gamma_s$  suggest a close-to-perfect filling factor  $\nu_m \approx 0.5$  of our bulk sample. The realization of high filling factors is attributed to the improved sample mounting technique, where a copper screw is used to tightly press the sample on the chip surface (cf. Section 3.2).

Simulations of the filling factor based on the dynamic magnetic field distribution show that the spiral resonator enables higher collective coupling rates in realistic sample mounting conditions compared to designs with meandering structures.

Finally we observe that with increasing temperature, the spin system accepts higher microwave powers before entering the saturation regime, which is explained by decreasing relaxation times  $T_1$  and  $T_2$  for increased temperature. We conclude that the spin ensemble is more conveniently characterized at higher temperatures (well below  $T_c$ ), where the improvement of SNR due to a higher drive power overweights the reduction of  $g_{\text{eff}}$  due to a smaller thermal polarization  $P(T)$ .



## Chapter 6

# Pulsed Electron Spin Resonance

Pulsed ESR is a powerful tool for characterizing paramagnetic spin ensembles. Applying a multiple pulse sequence like the Hahn echo or the inversion recovery sequence to a resonator, which is coupled to a spin system, results in a microwave echo. From the dependence of the echo intensity on specific parameters of the pulse sequence, we can extract information about the fundamental properties of the spin ensemble like the spin-spin or the spin-lattice relaxation times [44]. In the following, we perform various experiments investigating both the paramagnetic properties of phosphorus doped silicon as well as the application of microwave LERs in pulsed ESR experiments.

In Section 6.1.1, we introduce the standard Hahn echo pulse sequence consisting of Gaussian shaped pulses [44]. Next, we investigate the interplay of sample power, resonator parameters and pulse lengths, which is crucial for finding and maximizing the signal in pulsed experiments. In the second part of this chapter, we present various pulsed ESR experiments mainly conducted using the spiral resonator. Section 6.2.1 covers Hahn echo spectroscopy of phosphorus donors and dimers at multiple temperatures. Furthermore, we present echo-detected field and frequency sweeps, which respectively, give access to the spin system loss rate and demonstrate linewidth broadening when using short excitation pulses. In Section 6.2.4, we determine the spin-lattice relaxation time of the spin system using inversion recovery spectroscopy. Finally, we present the performance of spiral resonators for the application of driven Rabi oscillations.

### 6.1 Multiple Pulse Calibration

During a single microwave pulse applied to the resonator, many parameters influence the angular velocity of the magnetization rotation in the Bloch sphere, which makes the determination of the optimal pulse length difficult. Moreover, pulse schemes have to be adapted to the analyzed spin system, in particular taking the relaxation times  $T_1$ ,  $T_2$  and  $T_2^*$  into account.

In this section, we first present the Hahn echo pulse sequence. Then we investigate the effect of the pulse length, the sample power and the resonator parameters on the signal magnitude in a Hahn echo experiment.

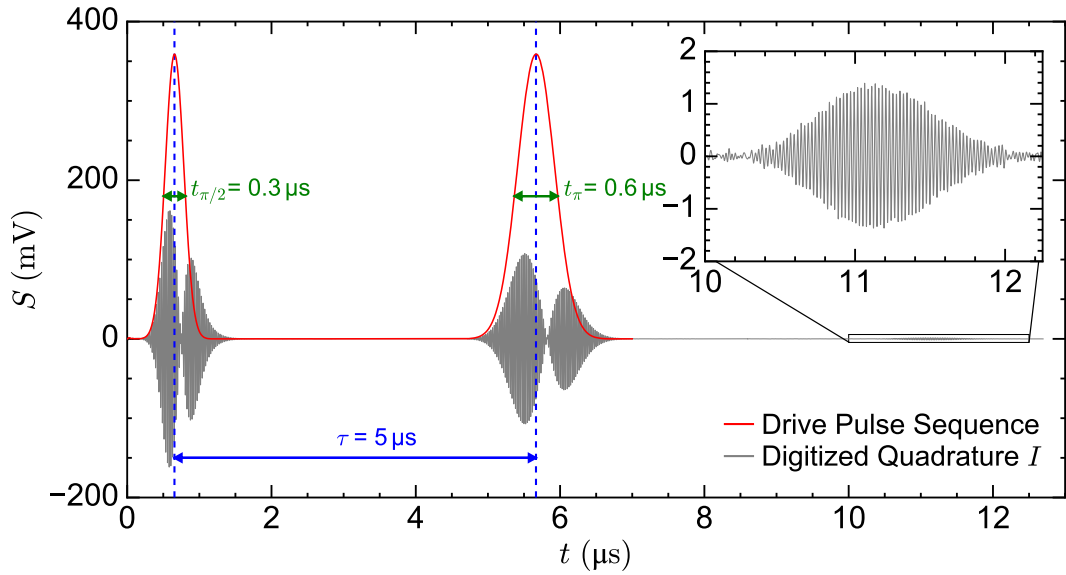


**Figure 6.1:** Hahn Echo pulse sequence with Gaussian excitation and refocusing pulse with length  $t_{\pi/2} = 0.3 \mu\text{s}$  and  $t_\pi = 0.6 \mu\text{s}$ , respectively. Both pulses are separated by  $\tau = 5 \mu\text{s}$ . The digitized signal of the quadrature  $I$  (grey curve) and the demodulated input pulse sequence (red curve) is plotted against the time  $t$ . The inset shows the resulting echo, which is located between  $t = 10.4 \mu\text{s}$  and  $t = 12 \mu\text{s}$ . Measurements were performed with the spiral resonator SR4 at 1.5 K using a drive power of  $-32 \text{ dBm}$  and a SRT of  $0.2 \text{ s}$  by averaging over 4000 shots.

### 6.1.1 Hahn Echo Pulse Sequence

In the following we present the standard Hahn echo pulse sequence [99]. Figure 6.1 shows a Hahn echo sequence performed on the resonator SR4 at 1.5 K with a Gaussian shaped excitation and refocusing pulse separated by a wait time of  $\tau = 5 \mu\text{s}$ . Generally,  $t_{\pi/2}$  ( $t_\pi$ ) denotes the length of the excitation (refocusing) pulse, which assumes the value 300 ns (600 ns) in Figure 6.1. The length of a Gaussian pulse is here defined as the full width at half maximum. The red curve depicts the demodulated signal of the input pulse sequence, which was measured 50 MHz offresonant from the resonance frequency  $\omega_r/2\pi = 4.281 \text{ GHz}$  of SR4. The measurements where acquired by averaging over 4000 shots with a shot-repetition-rate (SRT) of 0.2 s. The grey curve represents the in-phase component  $I$  of the digitized signal oscillating at an intermediate frequency of 42.5 MHz. We observe an echo signal, which is visualized by the inset of Figure 6.1. The echo occurs around  $5.6 \mu\text{s}$  after the center of the refocusing pulse and exhibits a maximal magnitude of  $\approx 1.4 \text{ mV}$ , which is 250 times smaller than the input signal magnitude. Finally, we observe a local minimum in the magnitude of the in-phase component  $I$  during either of the two Gaussian pulses. As discussed in Section 4.3.3, this is attributed to a destructive interference between the microwave input signal and the signal coupling back from the resonator into the transmission line.

### 6.1.2 Pulse Length Calibration

A typical commercial resonator used for conventional ESR has a well-defined specification of the excitation magnetic field as a function of the applied microwave power. This is typically not the case for LERs, as the resonator field magnitude  $|a|$  and in turn the dynamic magnetic field magnitude  $|B_1|$  strongly depends on the resonator parameters  $\kappa$  and  $\kappa_{\text{ext}}$  (cf. Section 2.1.3.2), in addition to the applied microwave power. If furthermore the relaxation times  $T_1$  and  $T_2$  of the investigated spin system are yet to be determined, there is a large space of available parameters for pulsed ESR experiments. For instance, in order to realize a Hahn echo,  $\tau$  may not exceed  $T_2$  by far to avoid dephasing of the spin system during the pulse sequence. Additionally, the shot-repetition-rate (SRT) should be  $> 6T_1$  to ensure that the ensemble is in its ground state prior to each shot. Motivated by this, we investigate the interplay between the optimal pulse lengths  $t_{\pi/2}$  and  $t_\pi$  of a Hahn echo sequence, the drive power and the resonator parameters in this section. The ESR response of a Hahn echo is quantified by the integrated echo area  $A_{\text{echo}}$ , which is obtained by integrating the demodulated echo signal (cf. Section 3.4). We performed a series of Hahn echo experiments, where we simultaneously varied the pulse lengths  $t_{\pi/2}$  and  $t_\pi$ , such that  $t_\pi = 2t_{\pi/2}$ , while all other parameters were fixed. In Figure 6.2(a), we plot the integrated echo area  $A_{\text{echo}}$  as function of  $t_{\pi/2}$  performed for different sample powers  $P_s$  with the spiral resonator SR4. The nominal sample power of a Gaussian pulse is defined as the peak power during the pulse.

For each sample power, we observe that increasing  $t_{\pi/2}$  from zero leads to an increased integrated echo area  $A_{\text{echo}}$  up to a maximal value. Further increasing  $t_{\pi/2}$  results in a decreased

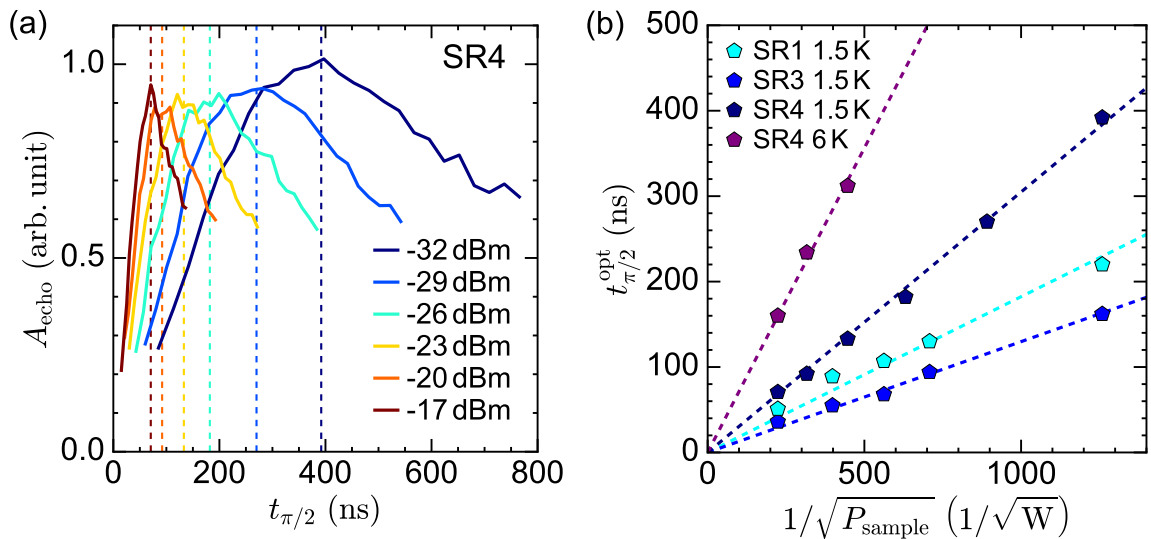


**Figure 6.2:** (a) Integrated echo area  $A_{\text{echo}}$  as a function of the excitation pulse length  $t_{\pi/2}$  for various sample powers (see legend) measured with the resonator SR4. The excitation pulse length is varied within individual ranges for each power, while the refocusing pulse length  $t_\pi = 2t_{\pi/2}$ . For each power, we extract an optimal excitation pulse length  $t_{\pi/2}^{\text{opt}}$ , defined as the pulse length at maximal echo area  $A_{\text{echo}}$ , as illustrated by the vertical dashed lines. (b) Optimal excitation pulse length  $t_{\pi/2}^{\text{opt}}$  as a function of the inverse square root of the sample power measured for different resonators at different temperatures (see legend). The dashed lines in (b) are straight lines through the origin fitted to each data set.

$A_{\text{echo}}$ . The value of the maximal echo area is comparable for all sample powers. However, the optimal pulse length  $t_{\pi/2}^{\text{opt}}$ , which is defined as  $t_{\pi/2}$  at the maximum of  $A_{\text{echo}}$  (vertical dashed lines in Figure 6.2(a)), exhibits a strong dependence on  $P_s$ , where  $t_{\pi/2}^{\text{opt}}$  is small for large values of  $P_s$  and vice versa.

In Figure 6.2(b), we plot the optimal pulse length  $t_{\pi/2}^{\text{opt}}$  of the Hahn echo excitation pulse against the inverse square root of the sample power for different data sets of spiral resonators and measurement temperatures. We fit a line through the origin individually to each set of data and find a very good agreement of each data set to the proportionality  $t_{\pi/2}^{\text{opt}} \propto 1/\sqrt{P_s}$ .

We can translate the optimal pulse length of the excitation pulse into the mean dynamic magnetic field  $B_1^{(\text{mean})}$  during the pulse via

$$\frac{\pi}{2} = \int \gamma B_1^{(\text{mean})} dt \approx \gamma B_1^{(\text{mean})} t_{\pi/2}, \quad (6.1)$$

Now, we can combine this relation with the proportionality factors between  $t_{\pi/2}^{\text{opt}}$  and  $1/\sqrt{P_s}$  and thus access the conversion factor of microwave power to dynamic magnetic field for each resonator. We find for the SR4

$$\frac{B_1^{(\text{mean})}}{\sqrt{P_s}} = 29 \frac{\text{mT}}{\sqrt{\text{W}}}. \quad (6.2)$$

Next, we investigate the relation between  $t_{\pi/2}^{\text{opt}}$  and the resonator photon number  $n$ , which is here defined as the equilibrium photon number corresponding to a continuous drive at the nominal sample power  $P_s$  of the pulse sequence. Using the resonator parameters  $\omega_r$ ,  $\kappa$  and  $\kappa_{\text{ext}}$  extracted from CW measurements in combination with  $P_s$ , we obtain the photon number  $n$  via Eq. (2.16). Finally, we plot  $t_{\pi/2}^{\text{opt}}$  as a function of  $1/\sqrt{n}$  for several resonators in Figure 6.3.

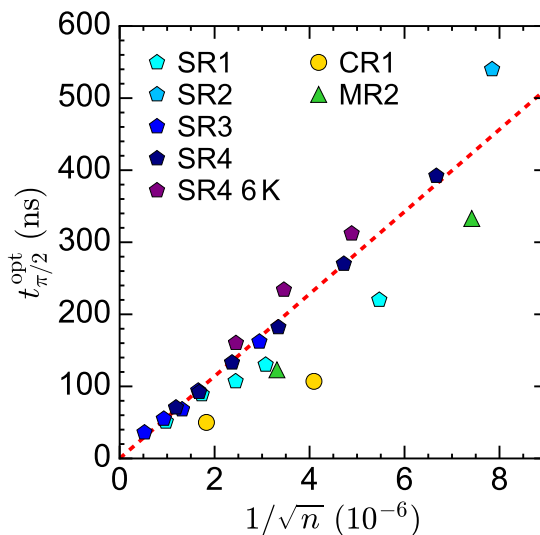


**Figure 6.3:** Optimal excitation pulse length  $t_{\pi/2}^{\text{opt}}$  as a function of the inverse square root of the resonator photon number, measured for various resonators. The photon number is calculated with Eq. (2.16) based in each resonator's individual parameter extracted from continuous wave measurements. The dashed line is a fit to all data points of spiral resonators.

Apart from small deviations, we observe a linear scaling of  $t_{\pi/2}^{\text{opt}}$  with  $1/\sqrt{n}$  for all data points of spiral resonators. This is illustrated by the dashed line, which is a line through the origin fitted to the data points of spiral resonators.

In order to describe the observations in Figure 6.2(b) and 6.3, we consider the rotation angle  $\theta_{\pi/2}$  of the spin system in the Bloch sphere due to the excitation pulse. Using Eq. (2.44),  $\theta_{\pi/2}$  follows the relation

$$\theta_{\pi/2} \propto \sqrt{P_s} \frac{\sqrt{\kappa_{\text{ext}}}}{\kappa} t_{\pi/2}. \quad (6.3)$$

Fixing  $\theta_{\pi/2} = 90^\circ$ , which corresponds to the optimal rotation of the magnetization into the xy-plane of the Bloch sphere, modifies Eq. (6.3) to

$$t_{\pi/2}^{\text{opt}} \propto \frac{1}{\sqrt{P_s}} \frac{\kappa}{\sqrt{\kappa_{\text{ext}}}}. \quad (6.4)$$

When considering a specific resonator, i.e. fixing  $\kappa$  and  $\kappa_{\text{ext}}$ , Eq. (6.4) yields the relation  $t_{\pi/2}^{\text{opt}} \propto 1/\sqrt{P_s}$  between optimal pulse time and sample power, which explains the observations in Figure 6.2(b). Moreover, Eq. (6.4) applies to all resonators of one design, which describes the relation  $t_{\pi/2}^{\text{opt}} \propto 1/\sqrt{n}$  observed in Figure 6.3, since the square root of the steady state photon number is exactly (see Eq. (2.16))

$$\sqrt{n} = \sqrt{P_s} \frac{\sqrt{\kappa_{\text{ext}}}}{\kappa}. \quad (6.5)$$

## 6.2 Pulsed ESR Experiments

### 6.2.1 Hahn Echo Spectroscopy

The spin-spin relaxation time  $T_2$  of a spin ensemble can be determined by performing a series of Hahn echo experiments with varying wait time  $\tau$  between the excitation and refocusing pulse and fitting the exponential decay of the resulting integrated echo areas with [44]

$$A_{\text{echo}} \propto \exp\left(-\frac{2\tau}{T_2}\right). \quad (6.6)$$

Figure 6.4(a) illustrates the demodulated signal  $S$  as a function of time, centered around the maximum of the echo signal ( $t_{\text{echo}}$ ), for values of  $\tau$  between 5  $\mu\text{s}$  and 200  $\mu\text{s}$ . The measurements were performed on the high field hyperfine split transition of isolated phosphorus ( $P_1$ ) in silicon, brought in resonance with the spiral resonator SR4 by tuning the magnetic field to 168.09 mT. The magnitude of the maximal echo signal  $S(t_{\text{echo}})$  decreases for increasing wait time  $\tau$ , while the width of the echo signal remains constant. We integrate the resulting echo areas and plot them on a logarithmic y-axis as a function of  $2\tau$  in Figure 6.4(b). We observe an exponential decay, which is fitted (green line) with Eq. (6.6) and yields a spin-spin relaxation time of  $T_2 = 120 \mu\text{s} \pm 2 \mu\text{s}$ . This result is comparable to  $T_2 \approx 200 \mu\text{s}$  reported for isotopically purified silicon with a concentration of  $10^{16} \text{ cm}^{-3}$  [36].

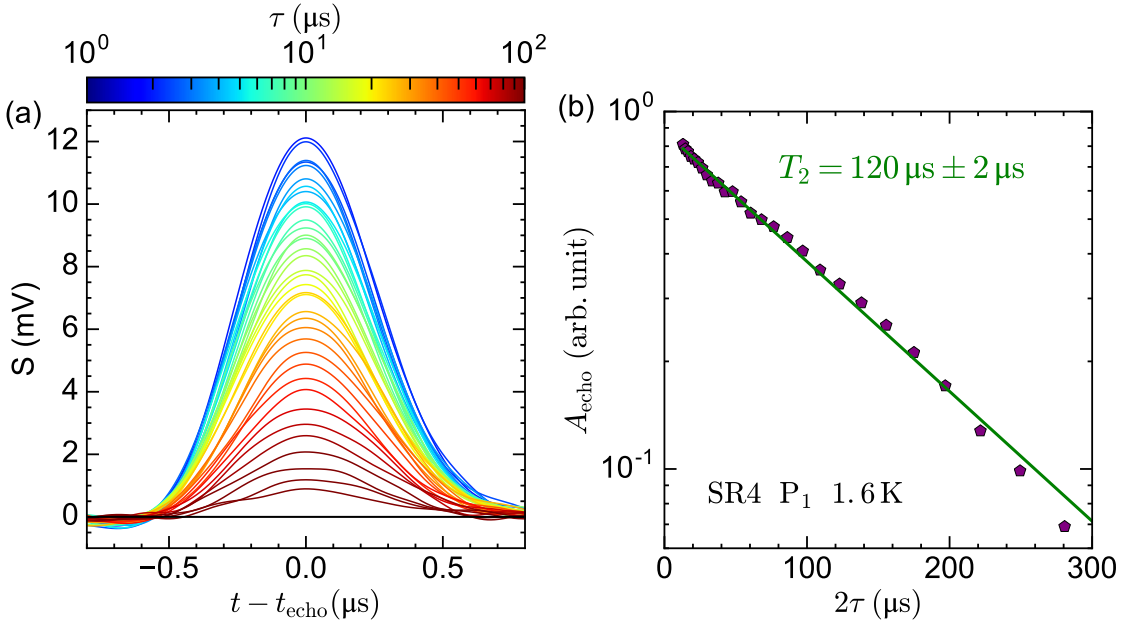


**Figure 6.4:** Determination of the spin-spin relaxation time  $T_2$  of the high field hyperfine split transition coupled to the resonator SR4 at 1.6 K and a sample power of  $-25$  dBm. The measurements were performed by successively increasing the wait time  $\tau$  of a Hahn echo with  $t_{\pi/2} = 170$  ns and  $t_\pi = 340$  ns. The signal is averaged 2500 times with a SRT of 0.5 s. **(a)** Demodulated echo signals for different values of  $\tau$  (see color code) as a function of time. **(b)** Integrated echo area  $A_{\text{echo}}$  (purple marker) on a logarithmic scale (y-axis) plotted against  $2\tau$ . The green line represents a fit with Eq. (6.6).

Next, the measurement series is repeated for higher temperatures. The integrated echo area as a function of  $2\tau$  for a measurement at 6 K is depicted in Figure 6.5(a).

The recorded demodulated signals  $S$  (not shown) and the integrated echo areas are subject to higher noise due to the increased measurement temperature. Fitting Eq. (6.6) to the data yields  $T_2 = 90 \mu\text{s} \pm 8 \mu\text{s}$ .

Additionally, we performed pulsed ESR experiments on phosphorus dimers  $P_2$  in silicon. Phosphorus dimers are only formed, when the distance between two donor pairs is sufficiently small, such that the exchange coupling strength  $J$  exceeds the hyperfine splitting constant  $A$  [100]. Hence, the collective coupling rate  $g_{\text{eff}} \propto \sqrt{\rho}$  (cf. Eq. (5.9)) of these clusters is expected to be reduced in comparison to the isolated phosphorus donors due to a decreased spin density. This gives rise to a smaller echo signal, reducing the signal to noise ratio of pulse experiments with phosphorus dimers. In Figure 6.5(b), we plot the integrated echo area  $A_{\text{echo}}$  against  $2\tau$  measured at 1.6 K and an uncalibrated magnetic field of 165.78 mT. We find a spin-spin relaxation time of  $T_2 = 124 \mu\text{s} \pm 14 \mu\text{s}$ . However, this result can not solely be attributed to the  $P_2$  dimers, as there might be contributions from the large background signal due to the spin resonance of dangling bonds. In general, systematic measurements are required to separate both spin species.

In Figure 6.6, we summarize the measured decoherence times  $T_2$  of phosphorus donors and dimers as a function of temperature  $T$ . The relaxation time of isolated phosphorus donors de-

<sup>16</sup>  $B_{0,\text{set}}$  is the set value of the static magnetic field and admits deviations from the real field. For a discussion on the field calibration, see Section 5.1.1.

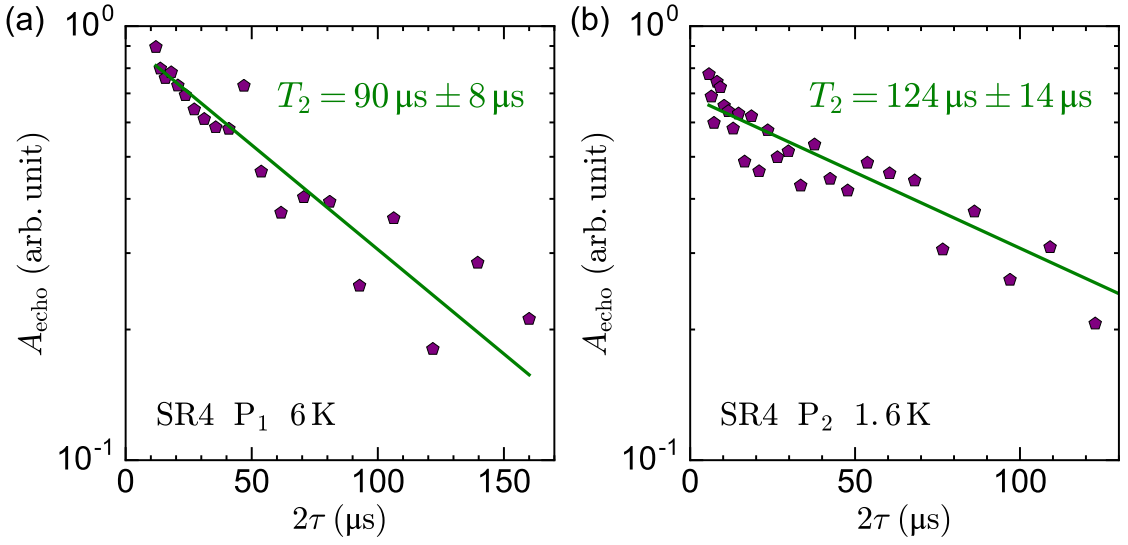


**Figure 6.5:** Determination of the spin-spin relaxation time  $T_2$  of (a) the high field hyperfine split transition of isolated phosphorus donors ( $P_1$ ) at 6 K and a field<sup>16</sup> of  $B_{0,\text{set}} = 167.38 \text{ mT}$ , and (b) the phosphorus donor clusters ( $P_2$ ) at 1.6 K and  $B_{0,\text{set}} = 165.78 \text{ mT}$ . Both measurements were performed on the resonator SR4 with a drive frequency of  $\omega_r/2\pi = 4.3906 \text{ GHz}$  ( $\omega_r/2\pi = 4.3745 \text{ GHz}$ ) at 1.6 K (6 K) and a sample power of  $-25 \text{ dBm}$ . The Hahn echo sequence was composed of pulse lengths around  $t_{\pi/2} = 170 \text{ ns}$  and  $t_\pi = 340 \text{ ns}$ . For both figures (a) and (b), the integrated echo area  $A_{\text{echo}}$  (purple marker) is plotted on a logarithmic scale (y-axis) as a function of  $2\tau$  with the green line representing a fit to the data with Eq. (6.6).

creases with increasing temperature. This behaviour is expected from theory as a consequence of multiple dephasing mechanisms like nuclear spin diffusion due to the presence of the  $^{29}\text{Si}$  isotope and instantaneous diffusion, i.e. a decoherence mechanism mediated by dipolar interaction of spins [36, 98].

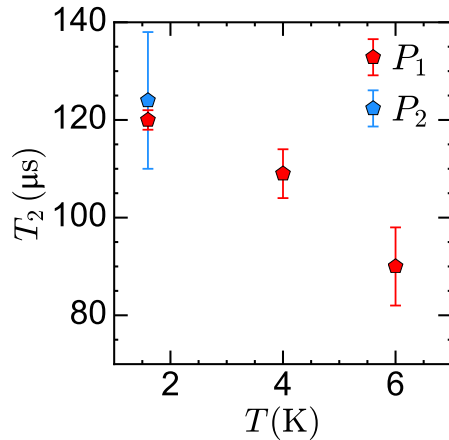


**Figure 6.6:** Spin-spin relaxation time of the high field hyperfine split transition of isolated phosphorus donors ( $P_1$ ) and phosphorus donor clusters ( $P_2$ ) as a function of temperature  $T$ . The provided errorbars are based on the uncertainties of fitting Eq. (6.6) to the integrated echo area  $A_{\text{echo}}(\tau)$ .

### 6.2.2 Echo-detected Frequency Sweep

We present measurement data of echo-detected frequency sweeps around the resonance frequency of resonator CR1, using a Hahn echo pulse sequence with short pulse lengths compared to the characteristic ring up time of the CR1. Figure 6.7 illustrates the integrated echo area  $A_{\text{echo}}$  as a function of detuning  $\Delta$  for several combinations of pulse length  $t_{\pi/2}$  and drive power  $P_s$  (see legend).

The pulse lengths of the blue, green and red data points are optimal for the respective sample power, i.e. they maximize the integrated echo area (cf. Section 6.1.2). In contrast, the yellow data points are acquired with strongly reduced pulse lengths  $t_{\pi/2} \ll t_{\pi/2}^{\text{opt}}$ . This explains the lower values of  $A_{\text{echo}}$  at resonant drive of the resonator ( $\Delta = 0$ ).

We observe a broadening of the echo signal linewidth with decreasing pulse lengths  $t_{\pi/2}$ . The yellow data points exhibit a similar linewidth as the green ones. We conclude, that the observed effect is not due to power broadening [44], since reducing the power from  $-25 \text{ dBm}$  (green) to  $-32 \text{ dBm}$  (yellow) for a fixed pulse length of  $t_{\pi/2} = 50 \text{ ns}$  shows little influence on the linewidth. We attribute these results to the finite linewidth broadening of Gaussian pulses in the frequency domain, which in general is pronounced for small pulse lengths (cf. Section 2.1.4).

When driving the spin ensemble with a Hahn echo sequence, which is detuned by  $\Delta/2\pi$  from the resonance frequency of the resonator, we expect an echo signal only if both, the excitation and the refocusing pulse have a linewidth broader than the detuning. The linewidth of a Gaussian pulse is inversely proportional to the pulse length (cf. Eq. (2.34)), leading to an even shorter excitation

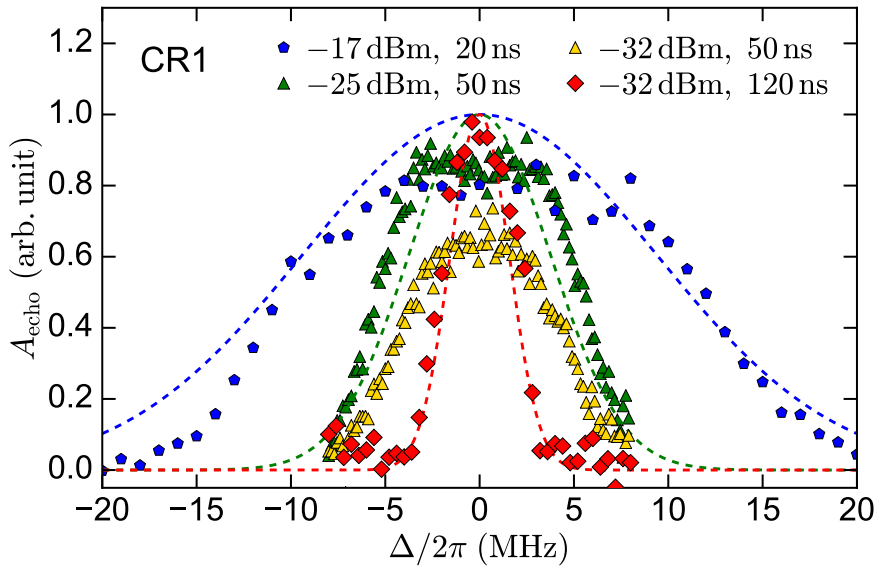


**Figure 6.7:** Echo-detected frequency sweep performed at the high field hyperfine split transition of  $P_1$  with the resonator CR1 using Hahn echo pulse sequences with various drive powers and excitation pulse lengths  $t_{\pi/2}$  (see legend). The integrated echo area is plotted as a function of the detuning  $\Delta = \omega - \omega_r$  from the resonance frequency  $\omega/2\pi = 3.9277 \text{ GHz}$  of CR1. For the Hahn echo sequences corresponding to the blue, green and red markers, we plotted (dashed lines with the same color) the normalized spectral distribution  $F_{\text{norm}}$  (see Eq. (6.7)) of the Gaussian refocusing pulse with length  $t_\pi$  of 40 ns, 100 ns and 240 ns, respectively, as a function of  $\Delta$ .

bandwidth for the refocusing pulse, which corresponds to half of the excitation bandwidth of the excitation pulse ( $t_{\pi/2} = 2t_\pi$ ). Thus, the refocusing pulse is the limiting factor for the offresonant excitation of the resonator. The corresponding normalized spectral distribution is given by (see Eq. (2.31))

$$F_{\text{Norm}}(\Delta) = \exp\left(-\frac{\Delta^2 t_\pi^2}{16 \cdot \ln 2}\right). \quad (6.7)$$

In Figure 6.7 we plotted  $F_{\text{Norm}}$  (dashed lines) as a function of  $\Delta$  in the same color as the corresponding Hahn echo sequence. We observe a good agreement between the expected and measured linewidth broadening, which verifies the hypothesis of linewidth broadening due to short pulse times. Deviations from the bare pulse sequence linewidth in the frequency domain are due to the finite resonator loss rate  $\kappa/2\pi$  and the spin system linewidth  $\gamma_s$ , which are not considered in the dashed lines in Figure 6.7.

Finally, we observe a flat echo area as a function of detuning  $\Delta/2\pi$  around the resonant excitation of the resonator ( $\Delta = 0$ ), which is best observable on the green data points in Figure 6.7. This is explained with the resonator dynamics of the CR1, which has a total loss rate around  $\kappa/2\pi \approx 550$  kHz. According to Eq. (2.17), the corresponding ring up time is  $\tau_r = 1/\kappa = 290$  ns, which is large compared to the pulse lengths  $t_{\pi/2}$  and  $t_\pi$ . Hence, for a detuning  $\Delta/2\pi = (\omega - \omega_r)/2\pi$ , the resonator oscillates a rather short time at the drive frequency  $\omega/2\pi$ , while the resonator ring down is governed by the large time scale  $\tau_r$  and essentially occurs at  $\omega_r/2\pi$  (see Section 2.1.3.3). This means, that the resonator ring down is the main contribution to the manipulation of the spin system for short pulse lengths  $t_{\pi/2}, t_\pi \ll \tau_r$ . In order to compare the transient excitation of a resonator as a function of the detuning, we have to consider the resonator field magnitude  $|a|$  at the end of the short pulse in addition to the pulse length and the ring down time. However, the dynamic of a resonator is little dependent on the detuning  $\Delta/2\pi$  for small drive times  $t \ll \tau_r$ , as illustrated by Figure 2.6. Hence, we can assume a roughly constant value for  $|a|$  at the end of the short excitation pulse.

We conclude that the Hahn echo is insensitive to detuning from the resonance frequency of a narrow linewidth resonator. This can be of advantage when operating with narrow linewidth resonators, since slight detuning from the resonance frequency does not reduce the ESR signal. It can also be of disadvantage, for instance, when one is interested in measuring the spin system linewidth as performed in the next section.

### 6.2.3 Echo-detected Field Sweep

We determine the spin system loss rate  $\gamma_s$  using an echo-detected field sweep. In this measurement, we consider the low field hyperfine split transition of isolated phosphorus donors driven at a fixed frequency of 4.3906 MHz, which corresponds to the resonance frequency of resonator SR4. Figure 6.8 shows the integrated echo area  $A_{\text{echo}}$  as a function of the uncalibrated magnetic field  $B_0$  measured at 1.6 K.

We observe a broad peak of integrated echo area  $A_{\text{echo}}$  with a maximum at 163.8 mT, which is fitted with a Lorentzian function (green curve). Taking the calibration of the magnetic field into

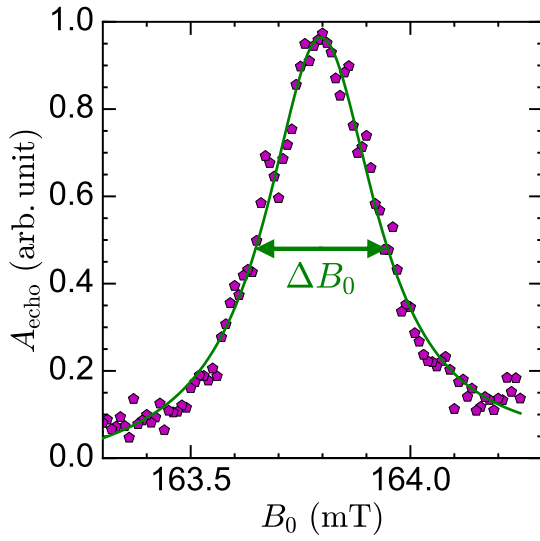


**Figure 6.8:** Echo-detected field sweep around the low field hyperfine split transition of isolated donors ( $P_1$ ) in silicon coupled to the resonator SR4. The integrated echo area is plotted as a function of the uncalibrated magnetic field. The Hahn echo measurements were performed at 1.6K with a sample power of  $-25$  dBm at a frequency of 4.3906 GHz. The green line represents a fit to the data using a Lorentzian model, where the full width at half maximum is denoted by  $\Delta B_0$ .

consideration, we find a magnetic full width at half maximum of  $\Delta B_0 = 314 \mu\text{T} \pm 10 \mu\text{T}$ . Using Eq. (5.6), this results translates into a spin loss rate of  $\gamma_s/2\pi = 4.4 \text{ MHz}$ , which is around 1.9 MHz higher than the value extracted from CW ESR measurements (see Section 5.1.3).

As shown above, the linewidth of a Hahn echo is broadened due to the finite length of microwave pulses. The data in Figure 6.8 was acquired using a Hahn echo sequence with a refocusing pulse length of  $t_\pi = 340 \text{ ns}$ . Hence, the spectral distribution of the pulse sequence has a half width at half maximum of  $\Delta\omega/2\pi = 2.773/2\pi t_\pi = 1.3 \text{ MHz}$  (cf. Eq. (2.34)), which can account for a large part of the difference in the spin loss rate. Additionally, the spin loss rate determine from pulsed ESR measurements can be attributed to power broadening [44, 101], since the pulsed measurements were conducted with a sample power of  $-25$  dBm, which is seven orders of magnitude higher compared to the sample power used for the continuous wave experiment.

#### 6.2.4 Inversion Recovery

The spin-lattice relaxation time  $T_1$  of a paramagnetic spin system can be determined using the inversion recovery pulse sequence [44]. This sequence consists of an initial inversion pulse with length  $t_{\text{inv}}$  followed by a variable wait time  $T$  and a standard Hahn echo pulse sequence. The expected integrated echo area as a function of the wait time  $T$  is given by [44]

$$A_{\text{echo}} \propto 1 - 2 \exp\left(-\frac{T}{T_1}\right). \quad (6.8)$$

Hence, by performing a series of inversion recovery pulse sequences with different values of  $T$  we gain information about the relaxation time  $T_1$ . For very long values of  $T$ , the magnetization is fully recovered during the wait time between the inversion pulse and the Hahn echo, such that the

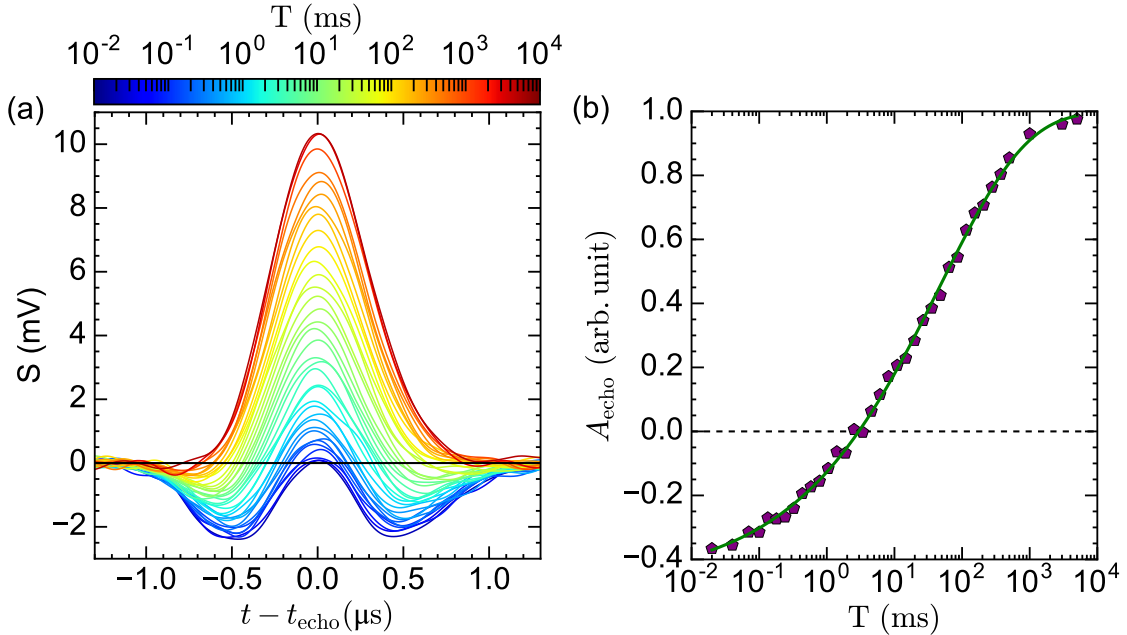


**Figure 6.9:** Determination of the spin-lattice relaxation time  $T_1$  of the high field hyperfine split transition of isolated phosphorus donors coupled to the resonator SR4 at 1.6 K. The inversion recovery measurements were performed by successively increasing the wait time  $T$  between the inversion pulse ( $t_{\text{inv}} = 400$  ns) and the excitation pulse of the Hahn echo. The excitation and refocusing pulse of the Hahn echo, respectively were designed with the pulse lengths of  $t_{\pi/2} = 200$  ns and  $t_\pi = 400$  ns, separated by a wait time of  $\tau = 3$  μs. (a) Demodulated echo signals for values of  $T$  between 40 μs and 5 s (see color code) as a function of time. (b) Echo area  $A_{\text{echo}}$  (purple marker) integrated between  $t = t_{\text{echo}} \pm 2$  μs plotted against  $T$  with a logarithmically scaled  $x$ -axis. The green line represents a fit to the data with Eq. (6.8) plus an additional offset on the  $y$ -axis.

echo signal resulting from the Hahn echo sequence is positive and maximal. The other limiting case is a very short wait time  $T$ , where the magnetization is ideally inverted, i.e. oriented in the negative z-direction on the Bloch sphere, immediately before the Hahn echo sequence, such that the resulting echo signal admits a negative demodulated echo area. Note that the demodulation is phase sensitive and thus yields negative demodulated signals, when the echo signal is opposite in phase with the drive tone.

Figure 6.9(a) shows the demodulated Signal  $S$  as a function of time for wait times  $T$  varying between 20 μs and 5 s. The measurement was performed on isolated phosphorus donors coupled to the resonator SR4 at 1.6 K. For long  $T$ , we observe a positive echo signal with a shape similar to the one observed in standard Hahn echo experiments (cf. Figure 6.4). Under these conditions, the inversion of the spin ensemble is fully relaxed to its thermal steady state and therefore the pure Hahn echo is expected.

In contrast, for  $T \lesssim 1$  ms, we observe a negative signal  $S$  with two minima on both sides of the echo center. For values of  $T$  between those two extreme cases, the echo shape evolves continuously between the two described shapes. As mentioned above, the negative signal  $S$  is due to a negative z-orientation of the magnetization prior to the Hahn echo sequence. However, we observe different echo signal shapes for short and long values of  $T$ . This is a consequence of the

$B_1$  inhomogeneity of the LER, since different  $B_1$  values result in different rotation angles on the Bloch sphere during the inversion pulse, contributing incoherently to the detected echo signal. Additionally, the observed lineshape might be attributed to the fact that the spin system loss rate  $\gamma_s$  exceeds the resonator linewidth  $\kappa$ .

Next, we plot the integrated echo area  $A_{\text{echo}}$  against the wait time  $T$  on a logarithmically scaled x-axis in Figure 6.9(b). With increasing  $T$  we observe an echo area  $A_{\text{echo}}$  increasing from  $-0.4$  to  $1.0$  in arbitrary units. Additionally,  $A_{\text{echo}}$  indicates a full relaxation for  $T \geq 1\text{ s}$ .

We observe that the model given by Eq. (6.8) does not describe the measurement data. Instead we use a stretched exponential ansatz given by [102, 103]

$$A_{\text{echo}} \propto (1 - 2 \exp\left(-\left(\frac{T}{T_1}\right)^b\right) + C). \quad (6.9)$$

We fit (green curve) this model to the measurement data with the free parameters  $T_1$ ,  $b$  and  $C$ , resulting in a spin-lattice relaxation time of  $T_1 = 48\text{ ms} \pm 3\text{ ms}$  and an exponent of  $b = 0.34$ .

Generally, doping concentrations of phosphorus in silicon exceeding  $1 \cdot 10^{16}\text{ cm}^{-3}$  lead to a rapidly reduced  $T_1$  time [12]. Due to the doping density of  $2 \cdot 10^{17}\text{ cm}^{-3}$  in our silicon crystal, the expected spin-lattice relaxation time is around  $T_1 = 5\text{ ms}$  [12], which is one order of magnitude smaller compared to our result.

### 6.2.5 Driven Rabi Oscillations

Driven Rabi oscillations can be measured with a three pulse sequence similar to the inversion recovery sequence, where the initial pulse has variable length  $t_p$  and the following wait time  $T$  is fixed. The initial pulse called preparation pulse rotates the magnetization in the Bloch sphere by an angle proportional to  $t_p$ , while the Hahn echo sequence effectively probes the z-component of the magnetization [44]. Therefore, we expect an oscillating echo signal as a function of the preparation pulse length  $t_p$ .

Figure 6.10 depicts the integrated echo area plotted against  $t_p$ . The data is acquired on the low field hyperfine split transition of isolated phosphorus donors in silicon with the resonator SR4 at  $1.6\text{ K}$ . The preparation pulse length was varied between  $50\text{ ns}$  and  $1500\text{ ns}$ . We used a sample power of  $-25\text{ dBm}$  which corresponds to an optimal refocusing pulse length of  $t_\pi = 400\text{ ns}$ .

When increasing the preparation pulse length  $t_p$  from zero, we observe a decrease of the echo area to a minimum of  $\approx -0.15$  (in arbitrary units) at  $t_p = 400\text{ ns}$ . Further increasing  $t_p$  leads to an increased  $A_{\text{echo}}$ , which remains almost constant for  $t_p \geq 700\text{ ns}$ .

The minimum of  $A_{\text{echo}}$  at  $t_p = 400\text{ ns}$  is expected, since this pulse length corresponds to  $t_\pi$ , which is the optimal pulse length for a  $180^\circ$  rotation of the magnetization. However, the rotation angle is proportional to the  $B_1$  magnitude experienced by a single spin in the mode volume of the resonator [44]. Hence, large fractions of the spin ensemble exhibit a rotation angle smaller or larger than  $180^\circ$ , due to the inhomogeneity of the  $B_1$ -field. Therefore only small parts of the spin ensemble contributes to the echo signal at  $t_p = 400\text{ ns}$ . Around the preparation pulse length of  $700\text{ ns}$ , the Bloch sphere is considered to be equi-populated. Further increasing  $t_p$  does not substantially change this state, which explains the unchanged echo shape (not shown) and the

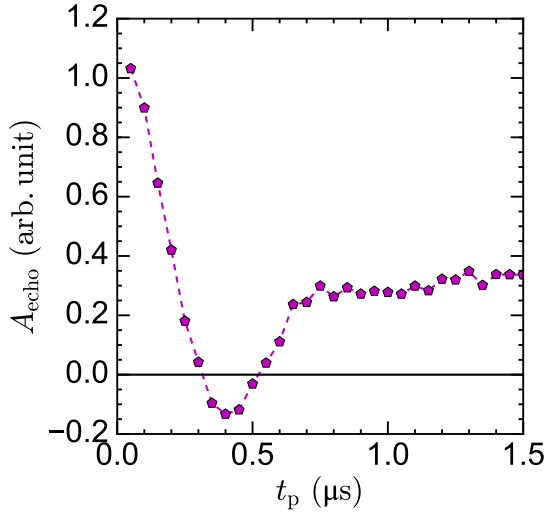


**Figure 6.10:** Driven Rabi oscillations of the low field hyperfine split transition of isolated phosphorus donors in silicon coupled to the resonator SR4. The integrated echo area is plotted as a function of the preparation pulse length  $t_p$ . We used a sample power of  $-25$  dBm, Hahn echo pulse lengths of  $t_{\pi/2} = 200$  ns and  $t_\pi = 400$  ns and a wait time of  $T = 1$  ms after the preparation pulse.

constant integrated echo area (Figure 6.10) for  $t_p > 700$  ns. This results highlights the limitations of a homogeneous magnetization control in large scale samples using LERs.

However, due to the higher  $B_1$  homogeneity, the SR represents an improvement compared to the CR, since negative echo areas as shown in Figure 6.9 and 6.10 could previously not be obtained with the CR design [54]. Coherent spin manipulation can in general be improved by reducing the dimensions of the sample, which contains the spin system. Particularly, in combination with the SR, which offer a large volume that shows little variation of the  $B_1$  magnitude (cf. Section 4.1.5), a sample with small dimensions is expected to yield a strongly enhanced coherence of the spin manipulation.

### 6.3 Summary

We investigated the dependence of the optimal pulse length  $t_{\pi/2}^{\text{opt}}$  in a Hahn echo sequence on the sample power and the resonator parameters. We find that  $t_{\pi/2}^{\text{opt}}$  is inversely proportional to the square root of the resonator photon number  $n$  throughout all resonators of one resonator design. Using the spiral design, we demonstrated various standard ESR experiments including Hahn echo and inversion recovery spectroscopy as well as driven Rabi oscillations. We measured the  $T_2$  times of phosphorus donors up to 6 K and dimers at 1.6 K finding values in the order of 100  $\mu\text{s}$ .

An echo-detected field sweep was used for calculating a spin loss rate of  $\gamma_s/2\pi = 4.4$  MHz, which is enhanced compared to the value resulting from CW measurements. This observation is attributed to power broadening. Moreover, we demonstrated the ESR linewidth broadening for echo-detected frequency sweeps with short pulse lengths and explained the observations with the finite broadening of the short Gaussian pulses in the frequency domain.

Additionally, we measured the spin-lattice relaxation time  $T_1$  at 1.6 K to be 34 ms for our spin

system. Here, we were able to demonstrate negative echo areas in an inversion recovery pulse sequence, which is an improvement with regards to the homogeneity of the dynamic excitation field of the spiral resonator, compared to resonator designs based on meandering structures. For a rapidly improved magnetization control, we propose small sample dimensions in combination with the improved  $B_1$  homogeneity of the spiral resonator.

## Chapter 7

# Summary & Outlook

The application of superconducting lumped element microwave resonators is beneficial for a variety of electron spin resonance (ESR) applications, ranging from the realization of strong coupling between a spin ensemble and a resonator to an increased sensitivity in pulsed ESR experiments. This raises the necessity to tailor the resonator's properties to the needs of a specific experiment and improve the performance towards numerous criteria like the resonator linewidth or the distribution of the magnetic excitation field.

We developed a fabrication process for high quality niobium superconducting microwave resonators. Here, the niobium is aluminum-coated aiming for an oxidation protection and hereby enabling a preservation of the resonator quality factor. The main aspect of the thesis is the development of three lumped element resonator designs, which include two different topological approaches, a meander and a spiral microstructure. Using FEM simulations, we demonstrated the tailoring of the resonance frequency  $f_r$  by the geometric design. Additionally, we showed how the external coupling rate  $\kappa_{\text{ext}}$  can be adjusted over several orders of magnitude. We found a good agreement of simulation results with pre-characterization measurements for all three designs. Furthermore, we estimated the resonance frequencies of the resonators using simple models for the electromagnetic properties of the microstructures.

With continuous wave measurements, we determined operation limits for the resonators with respect to temperature, static magnetic field and microwave power. We find that the microwave resonators remain in the linear regime for microwave powers of up to 0.25 mW ( $= -6 \text{ dBm}$ ) or  $2 \cdot 10^{13}$  photons. Moreover, the resonator designs are distinguished by an individual dependence of the resonance frequency on temperature and applied static magnetic field. We note that spiral resonators exhibit a significantly better performance when operated at higher temperatures with reduced internal losses by a factor of three compared to other designs. This behaviour is understood when comparing the kinetic and geometric inductance of the respective resonator type. In particular, the kinetic inductance rapidly increases close to the critical temperature of the superconductor, and hereby affects the resonance frequency and increases the internal losses of the resonator, decreasing its performance. The spiral resonator has a particularly favorable design as it exhibits a positive contribution of mutual inductance between neighbouring strip sections to the total inductance.

We successfully tested all three resonator designs in continuous wave and pulsed ESR measure-

ments. Using continuous wave measurements, we performed a spectroscopic analysis of phosphorus doped silicon coupled to a lumped element resonator (spiral design) and observe spectroscopic features associated with dangling bonds,  $P_2$ -clusters and the hyperfine split lines of isolated phosphorus donors. At  $T = 4\text{ K}$ , the ensemble of isolated donors exhibits a collective coupling rate of  $g_{\text{eff}}/2\pi = 335\text{ kHz}$  to the microwave resonator. From the magnetic ESR linewidth, we extract a spin loss rate of  $\gamma_s/2\pi = 2.5\text{ MHz}$ , which corresponds to a phase memory time of  $T_2^* = 400\text{ ns}$ . This result implies a weak coupling of the spin ensemble with a cooperativity of  $C = 0.027$  and  $C = 0.41$  to a broad and a narrow linewidth resonator, respectively. A comparison of the measured coupling strength  $g_{\text{eff}}$  to the theoretically expected value suggests a close-to-perfect filling factor of 0.5. The realization of high filling factors is enabled by an improved sample mounting technique, where a copper screw is used to tightly press the sample on the chip surface.

Due to the relatively high spin relaxation time  $T_1$  of  $48\text{ ms}$  and spin decoherence time  $T_2$  of  $120\mu\text{s}$ , phosphorus donors in silicon host crystals are prone to saturation behaviour. We observe an onset of saturation of the spin system at microwave sample powers around  $0.1\text{ pW}$  at  $1.5\text{ K}$ . Furthermore, the power threshold for saturation is increased for elevated temperatures, due to temperature-induced effects decreasing the relaxation times  $T_1$  and  $T_2$ . We model the saturation behaviour with a simple model taking into account the distribution of the dynamic excitation field, and find a very good agreement with the measurements data.

We next turn to the time domain experiments. We start with the initial characterization of the microwave transmission of a resonator in pulsed experiments. Using a time domain excitation and detection setup we show that the resonator dynamics can be understood and reproduced using simulations based on an equation of motion, taking the dynamics of the resonator and its coupling to the excitation signal line into account. With this verification of the theoretical framework, we can simulate and predict the transient of the dynamic magnetic field for microwave excitations with arbitrary pulse sequences. Based on the benchmark system of phosphorus doped silicon, we determine an expression of the optimal pulse length in pulsed ESR experiments as a function of the resonator parameters and the microwave power. We observe that this expression is universal for all resonators of one design. This allows to a priori optimize the ESR signal in pulsed experiments, by estimating the conversion factor of the microwave power to the dynamic magnetic field magnitude with the knowledge of the resonator parameters ( $\kappa, \kappa_{\text{ext}}$ ) of a lumped element resonator.

Using Hahn echo and inversion recovery spectroscopy, we determine the spin life-time and coherence time of the spin system to be  $T_1 = 48\text{ ms}$  and  $T_2 = 120\mu\text{s}$  at a temperature of  $1.6\text{ K}$ . Furthermore, we observe a broadening of the ESR linewidth for echo-detected drive frequency sweeps with short pulse lengths. We were able to quantitatively explain this observation with the finite bandwidth of pulse sequences in the frequency domain. Finally, the improved homogeneity of the dynamic excitation field of the spiral resonator compared to meandering resonators, allows for negative echo areas in inversion recovery and driven Rabi oscillation experiments.

The results and learnings of this thesis allow to improve the sensitivity of pulsed ESR experiments with lumped element resonators, by combining the homogeneous excitation field of the

spiral resonator with a sample volume tailored to small dimensions. In this way, one can realize a more uniform manipulation of all spins of the sample volume, which leads to an enhanced ESR signal. Furthermore, this allows to add experiments like for example driven Rabi oscillations to the toolbox of pulsed ESR with lumped element resonators.

In addition, based on the know how obtained in this thesis, the spiral resonator design can be further optimized towards an even more improved homogeneity of the dynamic magnetic field  $B_1$  by systematically studying the influence of geometric parameters on the  $B_1$  distribution. One approach is to reduce the spacing between neighbouring strip sections and at the same time enlarge the area of the resonator interior. This is expected to yield an enhanced mutual inductance, which further increases the robustness for measurement temperatures near the critical temperature.

The fabrication process developed during the course of this thesis allows to build lumped element microwave resonators with high internal quality factors. In combination with the demonstrated controllability of the external quality factor, we can now fabricate critically coupled narrowband resonators, which are ideal for maximizing the collective coupling rate of a spin ensemble to the resonator. Further advancing into the strong coupling regime makes it easier to study coherent excitation transfer between resonator and spin system, which is one key requirement for embedding spin ensembles into future quantum computers. Combining on one hand the resonators presented in this thesis, and on the other hand isotopically purified silicon doped with phosphorus at a concentration of  $2 \cdot 10^{17} \text{ cm}^{-3}$ , we shall be able to realize a cooperativity exceeding 400 at millikelvin temperatures.

Moreover, alternative superconducting materials and sample mounting techniques can be employed for ESR applications. The superconductor NbN exhibits a critical temperature of around  $T_c^{\text{NbN}} = 16 \text{ K}$  [65]. Thus, using the temperature-resilient spiral resonator design allows to utilize high quality resonators in ESR experiments for even higher temperatures as shown in this thesis. Finally, it is possible to fabricate a superconducting microwave resonator on a substrate, which hosts a spin system, like phosphorus doped silicon. This approach guarantees an ideal filling factors and represents a convenient technique for the production of ESR samples.



# Appendix A

## Appendix

### A.1 Power Dependence of the Dynamic Resonator Field

We show that the resonator field transient  $|a(t)|$  scales linearly with the input field magnitude  $|b_{\text{in}}(t)|$ .

We assume an arbitrary pulse sequence at frequency  $\omega/2\pi$  with maximal microwave power  $P_{\text{MW}}$  denoted by the input field

$$b_{\text{in}}(t, \omega, P_{\text{MW}}) = \sqrt{\frac{P_{\text{MW}}}{\hbar\omega}} \hat{b}_{\text{in}}(t), \quad t_0 < t < t_1 \quad (\text{A.1})$$

with the normalized pulse sequence  $0 < \hat{b}_{\text{in}}(t) < 1$ . The factor  $\sqrt{\frac{P_{\text{MW}}}{\hbar\omega}}$  stems from the relation between the photon number and the input field (cf. Eq. (2.16)). We are interested in the power dependence of the resonator field transient  $a = a(t, \omega, P_{\text{MW}})$ .

The resonator field equation of motion (see Eq. (2.3)) is solved using the method of variation of constants. First, we define the antiderivative

$$A(t) := \int_{t_0}^t (i\omega_r - \kappa) d\tilde{t} = (i\omega_r - \kappa)(t - t_0). \quad (\text{A.2})$$

With this, we can state the set of solutions

$$a_{\text{hom}}(t) = ce^{A(t)}, \quad c \in \mathbb{C} \quad (\text{A.3})$$

for the homogeneous problem  $\dot{a}(t) = (i\omega_r - \kappa)a(t)$ , which corresponds the scenario of a relaxation in the absence of a drive tone. Next, we assume the constant to be a time-dependent function  $c = c(t)$  and choose the ansatz  $a(t) = c(t)e^{A(t)}$ . Derivation of  $a(t)$  yields:

$$\dot{a}(t) = c(t)\dot{A}(t)e^{A(t)} + \dot{c}(t)e^{A(t)} = (i\omega_r - \kappa)a(t) + \dot{c}(t)e^{A(t)}. \quad (\text{A.4})$$

Comparing this with the inhomogeneous equation of motion (Eq. (2.3)) we find

$$\dot{c}(t) = \sqrt{\kappa_{\text{ext}}} b_{\text{in}}(t, \omega, P_{\text{MW}}) e^{-A(t)}, \quad (\text{A.5})$$

and hence

$$c(t) = \int_{t_0}^t \sqrt{\kappa_{\text{ext}}} b_{\text{in}}(\tilde{t}, \omega, P_{\text{MW}}) e^{-A(\tilde{t})} d\tilde{t} = \sqrt{\frac{P_{\text{MW}}}{\hbar\omega}} \cdot \int_{t_0}^t \sqrt{\kappa_{\text{ext}}} \hat{b}_{\text{in}}(\tilde{t}) e^{-A(\tilde{t})} d\tilde{t}. \quad (\text{A.6})$$

This finally proves the linear scaling of the resonator field magnitude with the magnitude of the input field

$$|a(t)| = |c(t)e^{A(t)}| \propto \sqrt{\frac{P_{\text{MW}}}{\hbar\omega}}. \quad (\text{A.7})$$

In particular,  $|a|$  is proportional to the square root of the pulse sequence microwave power.

## A.2 Estimation of Microstrip Inductance and Capacitance

The self inductance per unit length of a microstrip can be estimated by [104]

$$L_l = \left[ \ln\left(\frac{2l}{w+d}\right) + \frac{1}{2} + \frac{w+d}{3l} \right] 0.2 \frac{\text{nH}}{\text{mm}}, \quad (\text{A.8})$$

where  $l$ ,  $w$  and  $d$  denotes the strip length, width and thickness, respectively. For long strips  $l \gg w$ , the inductance depends only weakly on  $w$ . Additionally, the thickness of thin strips  $d \ll w$  can be neglected.

We estimate the microstrip capacitance  $C$  between two very thin strips with spacing  $s_{\text{cap}}$ , thickness  $d$  and length  $l$ . Here,  $C$  is approximated by the capacitance of two thin wires with radius  $r = d/2$  and distance  $D = w$ , which is given by the expression [105]

$$C = \frac{\pi\epsilon_0\epsilon_{\text{eff}}l}{\ln\left(\frac{D}{r}\right)}, \quad (\text{A.9})$$

where  $\epsilon_{\text{eff}}$  is the effective relative permittivity of the microstrips' dielectric environment.

This is a good approximation due to the high ratio  $s_{\text{cap}}/d = 100$  between the microstrip distance and the strip thickness, which reduces the influence of the strip cross section on the resulting capacitance. Moreover, the fabricated structures are not expected to have perfectly rectangular strip cross sections.

## A.3 Finite Element Method Simulations with CST Microwave Studios

For the three-dimensional finite element simulations (FEM) of lumped element resonators (LER), we use the software CST Microwave Studios, which basically is a high frequency solver for the set of Maxwell's equations.

We implement the  $6 \times 10 \text{ mm}^2$  chip, including the end-to-end coplanar waveguide (CPW) coupling to a single LER. The CPW is driven by two microwave ports at both chip ends. The superconducting material is modeled as a perfect electrical conductor (PEC) with a thickness of 150 nm. As substrate material, we use lossy silicon with a conductivity of  $2 \cdot 10^{-5} \frac{\text{S}}{\text{m}}$ , which implies dielectric

losses in the substrate and is exclusively responsible for the simulated internal losses of the LER. The simulations are performed with the broadband frequency domain solver following the recommendations of [106]. We apply a well increased mesh resolution to the LER structure (initial mesh dimensions around  $4\mu\text{m}$ ) compared to the large ground plane. Ultimately, we extract the microwave transmission between both ports as well as two- and three-dimensional dynamic electric and magnetic field data.

## A.4 Kinetic Inductance

In superconductors, the kinetic energy of charge carriers is non-negligible due to long mean free paths. When interpreting the total kinetic energy due to a current flow as magnetic energy generated by that current, one obtains the kinetic inductance  $L_K$  of a conductor. Its definition is [66]

$$\frac{1}{2}L_{k,l}(T)I^2 = \frac{\mu_0\lambda_L^2(T)}{2} \int_A J_z^2 dS, \quad (\text{A.10})$$

where  $L_{k,l}$  is the kinetic inductance per unit length,  $I$  is the supercurrent,  $\lambda_L(T)$  is the London magnetic penetration depth and  $J_z$  is the current density in the superconductor. The integral on the right-hand side is a surface integral over the cross section  $A$  of the superconducting strip.

Assuming a homogeneous current density  $J_z^{(hom)}$  over the area  $A$  with width  $w$  and thickness  $d$ , we find the following expression [67]

$$L_{k,l}^{(hom)}(T) = \frac{\mu_0\lambda_L^2(T)}{wd}. \quad (\text{A.11})$$

However, this is only a good description of reality if  $d < \lambda_L$ .

### A.4.1 Kinetic Inductance for Inhomogeneous Current Density

In analogy to the derivation of the internal magnetic field of a superconductor [65], we calculate a more realistic expression for the kinetic inductance of a superconducting strip. We assume a current density  $J_z^{(inhom)}$  based on an exponential decay with increasing distance from the superconductor surface, as motivated by [107], and adapt it to our strip cross section geometry ( $d \ll w$ ), which gives

$$J_z^{(inhom)}(y, z) = J_0 \cosh\left(\frac{z}{\lambda_L(T)}\right). \quad (\text{A.12})$$

This ansatz is illustrated in Figure A.1. In the following, we abbreviate  $\lambda_L(T)$  with  $\lambda$ .

First, we calculate the total current  $I$  flowing through the strip cross section

$$\begin{aligned} I &= \int_S J_z^{(inhom)}(y, z) dy dz = \int_{-w/2}^{w/2} dy \int_{-d/2}^{d/2} J_0 \cosh\left(\frac{z}{\lambda}\right) dz = J_0 w \left[ \lambda \sinh\left(\frac{z}{\lambda}\right) \right]_{-d/2}^{d/2} = \\ &= 2J_0 w \lambda \sinh\left(\frac{d}{2\lambda}\right). \end{aligned} \quad (\text{A.13})$$

Substituting this into the left-hand side of the definition of kinetic inductance (see Eq. (A.10))

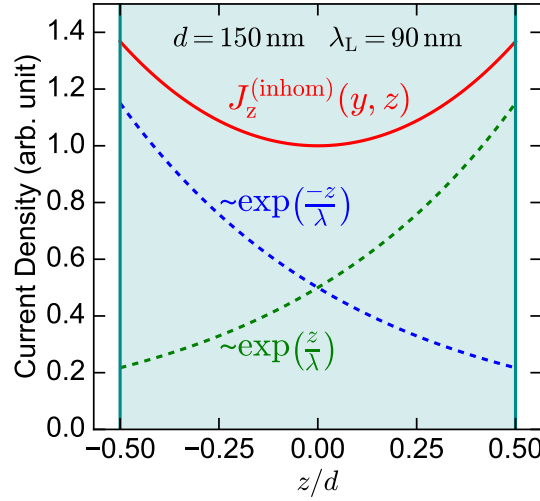


**Figure A.1:** Illustration of the inhomogeneous current density (red curve) along the  $z$ -dimension of a thin superconducting strip (cyan area). The red curve is the sum of the dashed ones.

yields

$$LHS = \frac{1}{2} L_{k,l} I^2 = 2 L_{k,l} J_0^2 w^2 \lambda^2 \sinh^2\left(\frac{d}{2\lambda}\right) = L_{k,l} J_0^2 w^2 \lambda^2 \left[ \cosh\left(\frac{d}{\lambda}\right) - 1 \right]. \quad (\text{A.14})$$

Next, we find for the right-hand side

$$\begin{aligned} RHS &= \frac{\mu_0 \lambda^2}{2} \int_A (J_z^{(\text{inhom})}(y, z))^2 \, dS = \frac{\mu_0 \lambda^2}{2} \int_{-w/2}^{w/2} dy \int_{-d/2}^{d/2} J_0^2 \cosh^2\left(\frac{z}{\lambda}\right) dz = \\ &= \frac{\mu_0 \lambda^2 J_0^2 w}{2} \int_{-d/2}^{d/2} \left[ \frac{1}{2} + \frac{1}{2} \cosh\left(\frac{2z}{\lambda}\right) \right] dz = \frac{\mu_0 \lambda^2 J_0^2 w}{2} \left( \frac{d}{2} + \frac{\lambda}{4} \left[ \sinh\left(\frac{2z}{\lambda}\right) \right]_{-d/2}^{d/2} \right) = \\ &= \frac{\mu_0 \lambda^2 J_0^2 w}{4} \left( d + \lambda \sinh\left(\frac{d}{\lambda}\right) \right). \end{aligned} \quad (\text{A.15})$$

Finally, we solve for the kinetic inductance after combining the left-hand and right-hand side

$$L_{k,l} J_0^2 w^2 \lambda^2 \left[ \cosh\left(\frac{d}{\lambda}\right) - 1 \right] = LHS = RHS = \frac{\mu_0 \lambda^2 J_0^2 w}{4} \left( d + \lambda \sinh\left(\frac{d}{\lambda}\right) \right), \quad (\text{A.16})$$

and therefore

$$L_{k,l}^{(\text{inhom})}(T) = \frac{\mu_0}{4w} \frac{d + \lambda \sinh\left(\frac{d}{\lambda}\right)}{\cosh\left(\frac{d}{\lambda}\right) - 1}. \quad (\text{A.17})$$

For  $d \ll \lambda$

### A.4.2 Influence on Resonance Frequency

We find that the total inductance is large compared to the temperature induced change of the kinetic inductance for  $T \ll T_c$  (cf. Figure 4.17)

$$L_{k,l}(T) - L_{k,l}(0) \ll L_{geo,l} + L_{k,l}(0). \quad (\text{A.18})$$

Hence, we can expand the relative frequency shift using

$$\begin{aligned} \frac{f_r(T) - f_r(0)}{f_r(0)} &= \sqrt{\frac{L_{geo,l} + L_{k,l}(0)}{L_{geo,l} + L_{k,l}(T)}} - 1 = \sqrt{\frac{1}{1 + \frac{L_{k,l}(T) - L_{k,l}(0)}{L_{geo,l} + L_{k,l}(0)}}} - 1 \approx -\frac{1}{2} \frac{L_{k,l}(T) - L_{k,l}(0)}{L_{geo,l} + L_{k,l}(0)} \\ &= \frac{1}{2} \frac{L_{k,l}(0)}{L_{geo,l} + L_{k,l}(0)} \left( 1 - \frac{L_{k,l}(T)}{L_{k,l}(0)} \right), \end{aligned} \quad (\text{A.19})$$

where we used the expansion for a variable  $x \ll 1$

$$\sqrt{\frac{1}{1+x}} = 1 - \frac{x}{2} + \mathcal{O}(x^2). \quad (\text{A.20})$$



# Bibliography

- [1] E. Zavoisky. Spin-Magnetic Resonance in Paramagnetics. *J. Phys. USSR* **245** (1945).
- [2] E. Zavoisky. Paramagnetic Relaxation of Liquid Solutions for Perpendicular Fields. *J. Phys. USSR* **211–216** (1945).
- [3] Takeshita, K. & Ozawa, T. Recent progress in in vivo esr spectroscopy. *Journal of Radiation Research* **45**, 373–384 (2004).
- [4] Han, J. Y., Hong, J. T. & Oh, K.-W. In vivo electron spin resonance: An effective new tool for reactive oxygen species/reactive nitrogen species measurement. *Archives of pharmacal research* **33**, 1293–1299 (2010).
- [5] Oda, M. N., Forte, T. M., Ryan, R. O. & Voss, J. C. The c-terminal domain of apolipoprotein A-I contains a lipid-sensitive conformational trigger. *Nature Structural Biology* **10**, 455–460 (2003).
- [6] Garbuio, L. *et al.* Orthogonal spin labeling and Gd(III)-nitroxide distance measurements on bacteriophage T4-lysozyme. *The Journal of Physical Chemistry. B* **117**, 3145–3153 (2013).
- [7] Portis, A. M. Electronic structure of F centers: Saturation of the electron spin resonance. *Physical Review* **91**, 1071–1078 (1953).
- [8] Feher, G., Fletcher, R. C. & Gere, E. A. Exchange effects in spin resonance of impurity atoms in silicon. *Physical Review* **100**, 1784–1786 (1955).
- [9] Feher, G. Electron spin resonance experiments on donors in silicon. I. electronic structure of donors by the electron nuclear double resonance technique. *Physical Review* **114**, 1219–1244 (1959).
- [10] Feher, G. & Gere, E. A. Electron spin resonance experiments on donors in silicon. ii. electron spin relaxation effects. *Physical Review* **114**, 1245–1256 (1959).
- [11] Wilson, D. K. & Feher, G. Electron spin resonance experiments on donors in silicon. iii. investigation of excited states by the application of uniaxial stress and their importance in relaxation processes. *Physical Review* **124**, 1068–1083 (1961).
- [12] Feher, G., Wilson, D. K. & Gere, E. A. Electron spin resonance experiments on shallow donors in germanium. *Phys. Rev. Lett.* **3**, 25–28 (1959).

- [13] Fanciulli, M. & Moustakas, T. D. Study of defects in wide band gap semiconductors by electron paramagnetic resonance. *Physica B: Condensed Matter* **185**, 228–233 (1993).
- [14] D. C. Maier. *Bruker Rep.* **13** (1997).
- [15] Schmidt, J. & Solomon, I. Modulation de la photoconductivite dans le silicium a basse temperature par resonance magnetique electronique des impuretes peu profondes. *Comptes Rendus Hebdomadaires des Seances de l'Academie des Sciences Serie b* **263**, 169 (1966).
- [16] Maxwell, R. & Honig, A. Neutral-impurity scattering experiments in silicon with highly spin-polarized electrons. *Phys. Rev. Lett.* **17**, 188–190 (1966).
- [17] Kawachi, G., Graeff, C. F. O., Brandt, M. S. & Stutzmann, M. Saturation measurements of electrically detected magnetic resonance in hydrogenated amorphous silicon based thin-film transistors. *Japanese Journal of Applied Physics* **36**, 121–125 (1997).
- [18] McCamey, D. R. *et al.* Electrically detected magnetic resonance in ion-implanted si: P nanostructures. *Applied Physics Letters* **89**, 182115 (2006).
- [19] Morello, A. *et al.* Single-shot readout of an electron spin in silicon. *Nature* **467**, 687–691 (2010).
- [20] Wrachtrup, J., von Borczyskowski, C., Bernard, J., Orrit, M. & Brown, R. Optical detection of magnetic resonance in a single molecule. *Nature* **363**, 244–245 (1993).
- [21] Gruber, A. Scanning confocal optical microscopy and magnetic resonance on single defect centers. *Science (New York, N.Y.)* **276**, 2012–2014 (1997).
- [22] Bienfait, A. *et al.* Reaching the quantum limit of sensitivity in electron spin resonance. *Nature Nanotechnology* **11**, 253–257 (2016).
- [23] Lindström, T., Healey, J. E., Colclough, M. S., Muirhead, C. M. & Tzalenchuk, A. Y. Properties of superconducting planar resonators at millikelvin temperatures. *Physical Review B* **80**, 144 (2009).
- [24] Wallace, W. J. & Silsbee, R. H. Microstrip resonators for electron–spin resonance. *Review of Scientific Instruments* **62**, 1754–1766 (1991).
- [25] Narkowicz, R., Suter, D. & Stonies, R. Planar microresonators for epr experiments. *Journal of Magnetic Resonance* **175**, 275–284 (2005).
- [26] Zollitsch, C. W. *et al.* High cooperativity coupling between a phosphorus donor spin ensemble and a superconducting microwave resonator. *Applied Physics Letters* **107**, 142105 (2015).
- [27] Eichler, C., Sigillito, A. J., Lyon, S. A. & Petta, J. R. Electron spin resonance at the level of  $10^4$  spins using low impedance superconducting resonators. *Physical Review Letters* **118**, 037701 (2017).

- [28] Probst, S. *et al.* Inductive-detection electron-spin resonance spectroscopy with 65 spins/ hz sensitivity. *Appl. Phys. Lett.* **111**, 202604 (2017).
- [29] Kubo, Y. *et al.* Strong coupling of a spin ensemble to a superconducting resonator. *Physical review letters* **105**, 140502 (2010).
- [30] Amsüss, R. *et al.* Cavity QED with magnetically coupled collective spin states. *Physical review letters* **107**, 060502 (2011).
- [31] Sandner, K. *et al.* Strong magnetic coupling of an inhomogeneous nitrogen-vacancy ensemble to a cavity. *Physical Review A* **85**, 1 (2012).
- [32] Probst, S. *et al.* Anisotropic rare-earth spin ensemble strongly coupled to a superconducting resonator. *Physical Review Letters* **110**, 157001 (2013).
- [33] Grezes, C. *et al.* Towards a spin-ensemble quantum memory for superconducting qubits. *Comptes Rendus Physique* **17**, 693–704 (2016).
- [34] Wu, H. *et al.* Storage of multiple coherent microwave excitations in an electron spin ensemble. *Physical Review Letters* **105**, 140503 (2010).
- [35] Kubo, Y. *et al.* Storage and retrieval of a microwave field in a spin ensemble. *Physical Review A* **85** (2012).
- [36] Tyryshkin, A. M. *et al.* Electron spin coherence exceeding seconds in high-purity silicon. *Nature Materials* **11**, 143–147 (2011).
- [37] Wallraff, A. *et al.* Strong coupling of a single photon to a superconducting qubit using circuit quantum electrodynamics. *Nature* **431**, 162–167 (2004).
- [38] Schoelkopf, R. J. & Girvin, S. M. Wiring up quantum systems. *Nature* **451**, 664–669 (2008).
- [39] Putz, S. *et al.* Protecting a spin ensemble against decoherence in the strong-coupling regime of cavity qed. *Nature Physics* **478**, 221 (2014).
- [40] Walls, D. F. & Milburn, G. J. *Quantum Optics*. Springer Study Edition (Springer, Berlin and Heidelberg, 1994).
- [41] Greifenstein, M. Elektronenspinresonanz mit supraleitenden mikrowellenresonatoren bei millikelvin-temperaturen. *Diploma Thesis* (2012).
- [42] Zhou, X. *et al.* Slowing, advancing and switching of microwave signals using circuit nanoelectromechanics. *Nature Physics* **9**, 179–184 (2013).
- [43] Rebić, S., Parkins, A. S. & Tan, S. M. Photon statistics of a single-atom intracavity system involving electromagnetically induced transparency. *Physical Review A* **65**, 36 (2002).

- [44] Schweiger, A. & Jeschke, G. *Principles of Pulse Electron Paramagnetic Resonance* (Oxford Univ. Press, Oxford, 2005), reprinted. edn.
- [45] Sigillito, A. J. *et al.* Fast, low-power manipulation of spin ensembles in superconducting microresonators. *Applied Physics Letters* **104**, 222407 (2014).
- [46] Khalil, M. S., Stoutimore, M. J. A., Wellstood, F. C. & Osborn, K. D. An analysis method for asymmetric resonator transmission applied to superconducting devices. *Journal of Applied Physics* **111**, 054510 (2012).
- [47] Dreher, L. *et al.* Electroelastic hyperfine tuning of phosphorus donors in silicon. *Physical Review Letters* **106**, 037601 (2011).
- [48] Stone, N. J. Table of nuclear magnetic dipole and electric quadrupole moments. *Atomic Data and Nuclear Data Tables* **90**, 75–176 (2005).
- [49] Höcherl, G. & Wolf, H. C. Zur konzentrationsabhängigkeit der elektronenspin-relaxationszeiten von diphenyl-picryl-hydrazyl in fester phase. *Z. Physik (Zeitschrift für Physik)* **183**, 341–351 (1965).
- [50] Nyquist, H. Thermal agitation of electric charge in conductors. *Physical Review* **32**, 110–113 (1928).
- [51] Pozar, D. M. *Microwave Engineering* (Wiley, Hoboken, 2012).
- [52] Göppel, M. *et al.* Coplanar waveguide resonators for circuit quantum electrodynamics. *Journal of Applied Physics* **104**, 113904 (2008).
- [53] Goetz, J. *The Interplay of Superconducting Quantum Circuits and Propagating Microwave States*. PhD Thesis, Technische Universität München (2017).
- [54] Zollitsch, C. W. *Single Excitation Transfer in the Quantum Regime*. PhD Thesis, Technische Universität München (2016).
- [55] Massel, F. *et al.* Microwave amplification with nanomechanical resonators. *Nature* **480**, 351–354 (2011).
- [56] Simons, R. *Coplanar waveguide circuits, components, and systems*. Wiley Series in Microwave and Optical Engineering (Wiley-Interscience, New York and Chichester and Weinheim, 2001).
- [57] Doyle, S., Mauskopf, P., Naylor, J., Porch, A. & Duncombe, C. Lumped element kinetic inductance detectors. *Journal of Low Temperature Physics* **151**, 530–536 (2008).
- [58] Yue, C. P. & Wong, S. S. Physical modeling of spiral inductors on silicon. *IEEE Transactions on Electron Devices* **47**, 560–568 (2000).

- [59] Khalil, M. S., Wellstood, F. C. & Osborn, K. D. Loss dependence on geometry and applied power in superconducting coplanar resonators. *IEEE Transactions on Applied Superconductivity* **21**, 879–882 (2011).
- [60] Assenheim, H. M. *Introduction to Electron Spin Resonance*. Monographs on Electron Spin Resonance (Springer US, Boston, MA and s.l., 1966).
- [61] Gao, J. *The Physics of Superconducting Microwave Resonators*. PhD Thesis, California Institute of Technology, Pasadena, California (2008).
- [62] C. C. Chin, D. E. Oates, G. Dresselhaus & and M. S. Dresselhaus. Nonlinear electrodynamics of superconducting NbN and nb thin films at microwave frequencies. *Physical Review B* 4788–4798 (1992).
- [63] Gubin, A. I., Il'in, K. S., Vitusevich, S. A., Siegel, M. & Klein, N. Dependence of magnetic penetration depth on the thickness of superconducting nb thin films. *Physical Review B* **72**, 224 (2005).
- [64] Levi, A. F. J. *Essential classical mechanics for device physics*. IOP concise physics (Morgan & Claypool Publishers and IOP Publishing, San Rafael and Bristol, 2016).
- [65] Gross, R. & Marx, A. *Festkörperphysik*. Mathematik, Physik 10-2012 (Oldenbourg Verlag, München, 2012).
- [66] Watanabe, K., Yoshida, K., Aoki, T. & Kohjiro, S. Kinetic inductance of superconducting coplanar waveguides. *Japanese Journal of Applied Physics* **33**, 5708–5712 (1994).
- [67] Annunziata, A. J. *et al.* Tunable superconducting nanoinductors. *Nanotechnology* **21**, 445202 (2010).
- [68] Gao, J. *et al.* Equivalence of the effects on the complex conductivity of superconductor due to temperature change and external pair breaking. *Journal of Low Temperature Physics* **151**, 557–563 (2008).
- [69] Booth, J. C., Beall, J. A., Rudman, D. A., Vale, L. R. & Ono, R. H. Geometry dependence of nonlinear effects in high temperature superconducting transmission lines at microwave frequencies. *Journal of Applied Physics* **86**, 1020–1027 (1999).
- [70] Zmuidzinas, J. Superconducting microresonators: Physics and applications. *Annual Review of Condensed Matter Physics* **3**, 169–214 (2012).
- [71] M. A. Golosovsky, H. J. Snortland & and M. R. Beasley. Nonlinear microwave properties of superconducting nb microstrip resonators. *Physical Review B* 6462–6469 (1995).
- [72] Abdo, B., Segev, E., Shtempluck, O. & Buks, E. Nonlinear dynamics in the resonance lineshape of NbN superconducting resonators. *Physical Review B* **73**, 1644 (2006).

- [73] Dahm, T. & Scalapino, D. J. Theory of intermodulation in a superconducting microstrip resonator. *Journal of Applied Physics* **81**, 2002–2009 (1997).
- [74] Garwood, M. & Ke, Y. Symmetric pulses to induce arbitrary flip angles with compensation for rf inhomogeneity and resonance offsets. *Journal of Magnetic Resonance (1969)* **94**, 511–525 (1991).
- [75] de Graaf, R. A. & Nicolay, K. Adiabatic rf pulses: Applications to in vivo NMR. *Concepts in Magnetic Resonance* **9**, 247–268 (1997).
- [76] Spindler, P. E. *et al.* Shaped optimal control pulses for increased excitation bandwidth in epr. *Journal of Magnetic Resonance* **218**, 49–58 (2012).
- [77] Castner, T. G., Lee, N. K., Cieloszyk, G. S. & Salinger, G. L. Dielectric anomaly and the metal-insulator transition in n -type silicon. *Phys. Rev. Lett.* **34**, 1627–1630 (1975).
- [78] Kodera, H. Effect of doping on the electron spin resonance in phosphorus doped silicon. iv. experimental study at liquid helium temperature. *Journal of the Physical Society of Japan* **27**, 1197–1203 (1969).
- [79] Abe, E. *et al.* Electron spin coherence of phosphorus donors in silicon: Effect of environmental nuclei. *Physical Review B* **82** (2010).
- [80] Gabrielse, G. & Tan, J. Self-shielding superconducting solenoid systems. *Journal of Applied Physics* **63**, 5143–5148 (1988).
- [81] Mani, R. G. *et al.* Demonstration of a 1/4-cycle phase shift in the radiation-induced oscillatory magnetoresistance in gaas/algaas devices. *Physical Review Letters* **92**, 146801 (2004).
- [82] Huebl, H. *et al.* Phosphorus donors in highly strained silicon. *Physical review letters* **97**, 166402 (2006).
- [83] Poindexter, E. H., Caplan, P. J., Deal, B. E. & Razouk, R. R. Interface states and electron spin resonance centers in thermally oxidized (111) and (100) silicon wafers. *Journal of Applied Physics* **52**, 879–884 (1981).
- [84] Stesmans, A. & Afanas'ev, V. V. Electron spin resonance features of interface defects in thermal (100)si/sio<sub>2</sub>. *Journal of Applied Physics* **83**, 2449–2457 (1998).
- [85] Jérôme, D. & Winter, J. M. Electron spin resonance on interacting donors in silicon. *Physical Review* **134**, A1001–A1007 (1964).
- [86] Maekawa, S. & Kinoshita, N. Electron spin resonance in phosphorus doped silicon at low temperatures. *Journal of the Physical Society of Japan* **20**, 1447–1457 (1965).
- [87] Morigaki, K. & Maekawa, S. Electron spin resonance studies of interacting donor clusters in phosphorus-doped silicon. *Journal of the Physical Society of Japan* **32**, 462–471 (1972).

- [88] Portis, A. M., Kip, A. F., Kittel, C. & Brattain, W. H. Electron spin resonance in a silicon semiconductor. *Physical Review* **90**, 988–989 (1953).
- [89] Rose, B. C. *et al.* Coherent rabi dynamics of a superradiant spin ensemble in a microwave cavity. *Physical Review X* **7** (2017).
- [90] Herskind, P. F., Dantan, A., Marler, J. P., Albert, M. & Drewsen, M. Realization of collective strong coupling with ion coulomb crystals in an optical cavity. *Nature Physics* **5**, 494–498 (2009).
- [91] Huebl, H. *et al.* High cooperativity in coupled microwave resonator ferrimagnetic insulator hybrids. *Physical Review Letters* **111**, 127003 (2013).
- [92] Kittel, C. *Introduction to solid state physics* (Wiley, Hoboken, NJ, 2005), 8. ed. edn.
- [93] Abe, E., Wu, H., Ardavan, A. & Morton, J. J. L. Electron spin ensemble strongly coupled to a three-dimensional microwave cavity. *Applied Physics Letters* **98**, 251108 (2011).
- [94] Blundell, S. *Magnetism in condensed matter*, vol. 4 of *Oxford master series in condensed matter physics* (Oxford Univ. Press, Oxford, 2014), reprint edn.
- [95] Cullis, P. R. Electron paramagnetic resonance in inhomogeneously broadened systems: A spin temperature approach. *Journal of Magnetic Resonance* (1969) **21**, 397–418 (1976).
- [96] Fajer, P., Watts, A. & Marsh, D. Saturation transfer, continuous wave saturation, and saturation recovery electron spin resonance studies of chain-spin labeled phosphatidylcholines in the low temperature phases of dipalmitoyl phosphatidylcholine bilayers. effects of rotational dynamics and spin-spin interactions. *Biophysical Journal* **61**, 879–891 (1992).
- [97] Castner, T. G. Saturation of the paramagnetic resonance of a V center. *Physical Review* **115**, 1506–1515 (1959).
- [98] Tyryshkin, A. M., Lyon, S. A., Astashkin, A. V. & Raitsimring, A. M. Electron spin relaxation times of phosphorus donors in silicon. *Physical Review B* **68**, 193207 (2003).
- [99] Hahn, E. L. Spin echoes. *Physical Review* **80**, 580–594 (1950).
- [100] Shankar, S., Tyryshkin, A. M. & Lyon, S. A. Esr measurements of phosphorus dimers in isotopically enriched si<sub>28</sub> silicon. *Physical Review B* **91**, 663 (2015).
- [101] Dréau, A. *et al.* Avoiding power broadening in optically detected magnetic resonance of single NV defects for enhanced DC magnetic field sensitivity. *Physical Review B* **84** (2011).
- [102] Zatryb, G., Podhorodecki, A., Misiewicz, J., Cardin, J. & Gourbilleau, F. On the nature of the stretched exponential photoluminescence decay for silicon nanocrystals. *Nanoscale research letters* **6**, 106 (2011).
- [103] Brown, S. L. *et al.* Origin of stretched-exponential photoluminescence relaxation in size-separated silicon nanocrystals. *AIP Advances* **7**, 055314 (2017).

- [104] Steinberg, K., Scheffler, M. & Dressel, M. Microwave inductance of thin metal strips. *Journal of Applied Physics* **108**, 096102 (2010).
- [105] Kothari, D. P. & Nagrath, I. J. *Power System Engineering* (Tata McGraw-Hill, New Delhi [u.a.], 2009), 2. ed., [nachdr.] edn.
- [106] Weiland, T., Timm, M. & Munteanu, I. A practical guide to 3-d simulation. *IEEE Microwave Magazine* **9**, 62–75 (2008).
- [107] Shadowitz, A. Rectangular type-ii superconducting wires carrying axial current. *Physical Review B* 2841–2843 (1981).

# Acknowledgments

I want to thank everyone who contributed to the thesis and accompanied my way during the last year. Particularly, I thank:

Prof. Dr. Rudolf Gross, for giving me the opportunity of doing this work at the Walther-Meißner-Institut (WMI).

Dr. Hans Huebl, for introducing me to the interesting field of microwave resonators and the physics of ESR, which has been truly a pleasure to work on, for the huge amount of knowledge I was able to acquire during my thesis, for numerous lengthy discussions, which always provided me with fruitful ideas, for introducing me to scientific working (sometimes the hard way) and finally for constantly supporting me throughout this thesis.

Stefan Weichselbaumer, for being a very pleasant and respectful adviser, for sharing with me your immense technical knowledge about microwave engineering, programming and ESR, for always helping me when I was in need of help and for your great willingness to support me during the writing process. I enjoyed working with you.

Philip Schmidt, for essentially introducing me to the art of experiments at cryogenic temperatures and giving me the starting point for all the experimental results, for providing me with a lot of fresh ideas and for always being a patient and valuable conversational partner.

Clemens Mühlenhoff, for being the best imaginable mate, for spending uncountable many lunches, coffee-less coffee breaks, stays in the clean room, evenings and nights with me at the WMI, for talking with me about everything that comes to your mind, which is a lot, for sharing the same work life imbalance and just for being a really good friend.

Michaela Schleuder, for enlightening the atmosphere at the WMI, for spreading cheer and positivity (coupled with traces of sarcasm) and for being a great and reliable conversationalist.

The master students Sarah Gelder, Christian Besson, Lukas Liensberger, Behdad Ghaffari, Saki Matsuura, Lisa Rosenzweig, Christoph Utschick, Daniel Arweiler, Birte Cöster, Luis Flacke and Tobias Wimmer, for generating a very pleasant and enjoyable atmosphere at the WMI, for always being trustful and helpful mates and for sharing uncountable many amusing moments with me.

Hannes Maier-Flaig, for many interesting conversations which sometimes happened to thematise physics.

Daniel Schwienbacher, Micheal Fischer and Edwar Xi, for fabrication, technical and programming support, whenever needed.

Mathias Weiler, Stephan Geprägs and Matthias Opel, for sharing their knowledge and providing great support.

Mathias Althammer, for spending endless time with me on the elderly care of the cryostat.  
Mathias Pernpeintner, for giving me a great training on the fabrication facilities at the WMI.  
Thomas Brenninger and Sebastian Kammerer for maintaining the experimental and fabrication facilities at the WMI.  
Prof. Dr. Martin Brandt for sharing his wafers on stock with us.  
Kevni Büyüktas and Uwe Wahl, for putting trust in me and making this thesis yet possible.  
My parents and Maria Farhat, for taking care of the little ones whenever needed and for providing us with delicious food.  
Nora, for your great support during the last year, for the rare beautiful moments and for taking care of our wonderful children.  
Elias and Noah, for a beautiful motivation in life.